Department of Physics and Astronomy

University of Heidelberg

Master thesis

in Physics

submitted by

Patrick Fahner

born in Mannheim

September 2015

Measurement of the branching ratio for the decay $\Lambda_b^0 \to D^0 p \mu^- \overline{\nu}_\mu X$ with the LHCb experiment

This Master thesis has been carried out by

Patrick Fahner

at the

Physikalisches Institut

under the supervision of

Prof. Dr. Ulrich Uwer

and

Dr. Mika Vesterinen

Zusammenfassung:

In der vorliegenden Arbeit wird zum ersten Mal das Verzweigungsverhältnis des Zerfalls $\Lambda_b^0 \to D^0 p\mu^- \overline{\nu}_\mu X$ relativ zum Referenzkanal $\Lambda_b^0 \to \Lambda_c^+ \mu^- \overline{\nu}_\mu$ gemessen. Die ausgewerteten Daten wurden in den Jahren 2011 und 2012 in Proton-Proton Kollisionen bei einer Schwerpunktsenergie von 7 TeV beziehungsweise 8 TeV am LHCb Experiment gesammelt. Dies entspricht einer integrierten Luminosität von $3\,\text{fb}^{-1}$. Mit Hilfe eines zweidimensionalen Fits an die invariante $D^0 p$ Masse und an $\log \chi^2_{\text{IP}}$, einem Maß für die Qualität des $D^0 p\mu^-$ Vertex, werden etwa 23000 $\Lambda_b^0 \to D^0 p\mu^- \overline{\nu}_\mu$ Signalereignisse rekonstruiert und extrahiert. Ein Fit an die korrigierte Λ_b^0 Masse ergibt für den Referenzkanal $\Lambda_b^0 \to \Lambda_c^+ \mu^- \overline{\nu}_\mu$ etwa 1,5 Millionen Ereignisse. Unter Berücksichtigung der Rekonstruktions- und Selektionseffizienzen erhält man damit ein relatives Verzweigungsverhältnis $\mathcal{R}$ von

$$\mathcal{R} := \frac{\mathcal{B}(\Lambda_b^0 \to D^0 p\mu^- \overline{\nu}_\mu X)}{\mathcal{B}(\Lambda_b^0 \to \Lambda_c^+ \mu^- \overline{\nu}_\mu)} = 0.0180 \pm 0.0013\,(\text{stat}) \pm 0.0014\,(\text{syst}).$$

Die Mehrheit der $\Lambda_b^0 \to D^0 p\mu^- \overline{\nu}_\mu X$ Zerfälle verläuft dabei nichtresonant, es werden aber auch Zerfälle über die Resonanzen $\Lambda_c(2880)^+$ und $\Lambda_c(2940)^+$ gemessen. Bei Betrachtung der invarianten $D^0 p$ Masse wird weiterhin eine unerwartete Häufung von Ereignissen um etwa 2840 MeV beobachtet. Es werden einige mögliche Ursachen hierfür untersucht, dennoch kann keine endgültige Erklärung für diese Häufung präsentiert werden. Derzeit gibt es keine experimentellen oder theoretischen Vergleichswerte für $\mathcal{R}$, die hier genannt werden können.

Abstract:

This thesis presents the first branching ratio measurement of the semileptonic decay $\Lambda_b^0 \to D^0 p\mu^- \overline{\nu}_\mu X$ with respect to the reference channel $\Lambda_b^0 \to \Lambda_c^+ \mu^- \overline{\nu}_\mu$. The analysed data was collected in proton-proton collisions at a centre-of-mass energy of 7 TeV respectively 8 TeV by the LHCb experiment in 2011 and 2012 and corresponds to an integrated luminosity of $3\,\text{fb}^{-1}$. About 23000 $\Lambda_b^0 \to D^0 p\mu^- \overline{\nu}_\mu$ signal events are reconstructed and extracted from a two-dimensional fit to the invariant $D^0 p$ mass and $\log \chi^2_{\text{IP}}$, a measure for the quality of the $D^0 p\mu^-$ vertex, distribution. With a fit to the corrected Λ_b^0 mass, about 1.5 million $\Lambda_b^0 \to \Lambda_c^+ \mu^- \overline{\nu}_\mu$ events are found. After consideration of reconstruction and selection efficiencies, the relative branching ratio $\mathcal{R}$ is determined as

$$\mathcal{R} := \frac{\mathcal{B}(\Lambda_b^0 \to D^0 p\mu^- \overline{\nu}_\mu X)}{\mathcal{B}(\Lambda_b^0 \to \Lambda_c^+ \mu^- \overline{\nu}_\mu)} = 0.0180 \pm 0.0013\,(\text{stat}) \pm 0.0014\,(\text{syst}).$$

The majority of the $\Lambda_b^0 \to D^0 p\mu^- \overline{\nu}_\mu X$ decay width is non-resonant, but there are also contributions from intermediate $\Lambda_c(2880)^+$ and $\Lambda_c(2940)^+$ resonances measured. Furthermore, there is an anomalous enhancement seen in the invariant $D^0 p$ mass spectrum. Its origin is not completely figured out in this thesis, but several cross-checks are presented. No theoretical predictions or experimental results on $\mathcal{R}$ exist so far for a comparison of the obtained result.

Contents

Chapter 1

Introduction

Developed about 40 years ago, the Standard Model of Particle Physics very successfully describes the properties of the known elementary particles and their interactions among each other [1–3]. It includes the electromagnetic, the strong and the weak interaction. Until today it has been probed with tremendous precision. With the exception of the neutrino masses, no results contradicting its predictions have been found so far. With the discovery of the Higgs boson in 2012 [4, 5], confirming the theory of electroweak symmetry breaking, the success of the Standard Model reached its climax.

Nonetheless, there are still open questions, which the Standard Model does not answer: Where does the asymmetry between matter and antimatter come from[1]? What is the origin of dark matter and of dark energy, making up about 95% of our universe in total [6]? How can gravitation be formulated as a quantum field theory and be combined with the Standard Model interaction to a more general theory of forces?

The Large Hadron Collider (LHC) of the European Organization for Nuclear Research (CERN) at Geneva, Switzerland is “the world’s largest and most powerful particle accelerator" [7] dedicated to tackle those questions. One of the four big experiments located at the LHC is the LHCb-experiment. It is built to probe the Standard Model to a high precision and to find indirect evidence for physics beyond the Standard Model, often referred to as “New Physics (NP)", by the study of hadron decays containing a b- or c-quark. These hadrons provide an excellent laboratory for the measurement of observables sensitive to New Physics like $\mathcal{CP}$-violation and many more. It allows furthermore to do spectroscopical analyses with bound heavy quark states leading to a better understanding of Quantum Chromodynamics (QCD), the theory of the strong interaction responsible for the bindings of quarks to hadrons. Unfortunately, QCD cannot be treated perturbatively in the energy regime of hadrons. Thus, theoretical predictions of such b-/c-hadron decays are always forced to make use of approximations, for instance of the Heavy Quark Effective Theory (HQET) [8]. The quark model of such theories predicts plenty of b-/c-hadron resonances [9]. Consequently, the more resonances and particles includ-

[1] Admittedly, with the $\mathcal{CP}$-violation the Standard Model provides a framework for matter-antimatter asymmetry, though it is not sufficient to explain the observed asymmetry in the universe.

ing their properties are measured, the better these effective theories can be adjusted and the better gets the knowledge of the strong interaction. While the B factories and hadron colliders made a great progress in studying b mesons, the knowledge of b baryons is rather poor.

This thesis aims to measure the branching fraction of the semileptonic decay $\Lambda_b^0 \to D^0 p\mu^- \overline{\nu}_\mu X$ in the form of a relative branching fraction ratio

$$\mathcal{R} := \frac{\mathcal{B}(\Lambda_b^0 \to D^0 p\mu^- \overline{\nu}_\mu X)}{\mathcal{B}(\Lambda_b^0 \to \Lambda_c^+ \mu^- \overline{\nu}_\mu)}$$

for the first time. The $D^0 p$ subsystem allows a spectroscopical analysis of Λ_c^+ resonances, here briefly denoted as Λ_c^{*+} via the intermediate reaction $\Lambda_b^0 \to \Lambda_c^{*+} \mu^- \overline{\nu}_\mu$, $\Lambda_c^{*+} \to D^0 p$. Furthermore, this decay is a hardly understood background in semileptonic searches for New Physics like the $\mathcal{CP}$-violating asymmetry a_{sl}^d [10] or the measurement of the CKM matrix element $|V_{ub}|$ in the decay $\Lambda_b^0 \to p\mu^- \overline{\nu}_\mu$ [11]. Hence, with the measurement of $\mathcal{B}\left(\Lambda_b^0 \to D^0 p\mu^- \overline{\nu}_\mu X\right)$ it is possible to reduce the uncertainties of those measurements.

This thesis is structured as follows. Chapter 2 introduces the Standard Model of Particle Physics as well as some searches for physics beyond the Standard Model. The last part of this chapter explains experimental techniques and methods used in this analysis. In Chapter 3, the LHCb-experiment, where the decays have been recorded, is described. Afterwards a short overview of the analysis strategy follows in Chapter 4. With Chapter 5, the actual analysis starts with the description of the event reconstruction and selection. It is followed by the determination of the signal yields through fits for the $\Lambda_b^0 \to D^0 p\mu^- \overline{\nu}_\mu X$ channel[2] in Chapter 6 and for the $\Lambda_b^0 \to \Lambda_c^+ \mu^- \overline{\nu}_\mu$ channel in Chapter 7. The required reconstruction and selection efficiencies are determined in Chapter 8. Subsequently, Chapter 9 contains a discussion of different backgrounds focusing on the $\Lambda_b^0 \to D^0 p\mu^- \overline{\nu}_\mu X$ signal channel. The systematic uncertainties are studied in Chapter 10. Since an anomalous enhancement appears in the $D^0 p$ mass spectrum in the signal fit, several cross-checks on the origin of this enhancement are presented in Chapter 11. In Chapter 12, all intermediate results are summarised and the relative branching ratio $\mathcal{R}$ is calculated. Eventually, this thesis ends in Chapter 13 with the conclusion.

[2] In this thesis, the channel $\Lambda_b^0 \to D^0 p\mu^- \overline{\nu}_\mu X$ will be also called signal channel and the $\Lambda_b^0 \to \Lambda_c^+ \mu^- \overline{\nu}_\mu$ channel normalisation or reference channel. The corresponding fits are sometimes labeled as signal fit respectively normalisation fit.

Chapter 2

Theory and motivation

2.1 The Standard Model of Particle Physics

The Standard Model of particle physics (SM) is a relativistic and renormalisable quantum field theory, that combines the electroweak theory developed by Glashow, Salam and Weinberg [1–3] with quantum chromodynamics (QCD), the theory of the strong interaction. It combines the current knowledge of fundamental particles and their interactions at microscopic level with the exception of gravitation.

The electroweak theory itself is a combination of the electromagnetic and the weak interaction. Every fundamental particle can interact via the weak force. For instance, the weak force is responsible for the β-decay of neutrons. Atoms or molecules are bound by the electromagnetic interaction taking place between electrically charged particles. If particles also carry a so-called colour charge, they can interact via the strong interaction, which binds e.g. protons and neutrons in a nucleus.

In the Standard Model, matter arises as half-integer spin particles from quantum fields. These particles are called FERMIONS and can be furthermore split up in QUARKS and LEPTONS. There exist 6 so-called "flavours" of quarks: up (u), down (c), charm (c), strange (s), top (t) and bottom[1] (b). According to their mass and other physical properties, they can be grouped into three generations:

$$\begin{pmatrix} u \\ d \end{pmatrix}, \begin{pmatrix} c \\ s \end{pmatrix}, \begin{pmatrix} t \\ b \end{pmatrix}.$$

Quarks in the top row are referred to as UP-TYPE quark. They carry an electrical charge of $+\frac{2}{3}e$, whereas DOWN-TYPE quarks carry a charge of $-\frac{1}{3}e$. Thus, they can participate in the electromagnetic interaction. In addtion, quarks carry colour charge allowing them to interact via the strong interaction.

Leptons do not carry colour charge as opposed to quarks. There exist three flavours of leptons, namely the electron (e^-), the muon (μ^-) and the tauon (τ^-) with an electric charge of $-e$ and their neutral counterparts, the neutrinos ν_e, ν_μ, ν_τ. Similarly to quarks, the leptons can be grouped into three generations

$$\begin{pmatrix} e^- \\ \nu_e \end{pmatrix}, \begin{pmatrix} \mu^- \\ \nu_\mu \end{pmatrix}, \begin{pmatrix} \tau^- \\ \nu_\tau \end{pmatrix}.$$

[1] The bottom quark is sometimes also called beauty.

As the neutrinos do neither carry electrical nor colour charge, they only interact weakly. Due to that fact it is not possible to detect neutrinos at hadron colliders like the LHC. For each fermion, there exists a corresponding antifermion with the same mass, but opposite quantum numbers.

In the Standard Model, the interactions among the particles are described by the mediation of spin-1 gauge bosons. For the electromagnetic interaction, this is the electric neutral photon γ. It couples to electrically charged particles. Since the photon is massless, the range of the electromagnetic interaction is infinite. The weak interaction is mediated by three massive gauge bosons: the electrically charged W^+ and W^- as well as the neutral Z boson. The $W^\pm$ bosons only couple to left-handed fermions (or right-handed antifermions), whereas the Z couples to both, left- and right-handed fermions, but with different strength. Due to their large mass of $m_{W^\pm} \approx 80\,\text{GeV}$ and $m_Z \approx 91\,\text{GeV}$ the weak interaction is only short-ranged. The strong interaction is carried by 8 massless gluons. They couple to particles carrying a colour charge and carry colour itself. Thus, gluon-gluon couplings are also possible, leading to a QCD coupling strength α_s, which strongly depends on the momentum transfer in an interaction. For low energies, α_s increases dramatically which means that coloured particles cannot be isolated. This phenomenon is called Confinement. At high energies, α_s is very small resulting in the Asymptotic Freedom, i.e. the quarks are thus quasi-free at short distances. Due to the confinement, strongly interacting composite particles alias Hadrons, must always be colour-neutral. They exist either as quark-antiquark systems and are called Mesons or as composite of three quarks named Baryons. Recent LHCb measurements report the observation of candidates for bound states consisting of even 4 quarks (2 quark, 2 antiquarks) [12] and also 5 quarks (4 quarks, 1 antiquark) [13], called Tetraquarks or Pentaquarks respectively.

Contradicting to the properties of the particles mentioned above, the invariance of local gauge transformation requires that the particles of the Standard Model are massless. This problem is solved by the Higgs mechanism, which introduces a doublet of complex scalar (spin 0) fields. The potential of these fields spontaneously breaks the electroweak symmetry and leads to massive bosons and fermions due to interaction with the Higgs field. The Higgs mechanism furthermore predicts a massive spin-0 particle, the Higgs Boson. As lastly unobserved particle, its discovery in July 2012 by ATLAS [4] and CMS [5] was a big success for the experimental community as well as for the theory of the Standard Model itself. Figure 2.1 summarises the fermions and bosons of the Standard Model and lists their main properties [14–16].

2.2 The interest in $\Lambda_b^0 \to D^0 p \mu^- \overline{\nu}_\mu X$

There are several reasons why the study of the decay $\Lambda_b^0 \to D^0 p \mu^- \overline{\nu}_\mu X$, which is analysed in this thesis, is interesting. On the one hand, the $D^0 p$ subsytem allows spectroscopical studies to learn more about QCD. On the other hand, the decay is

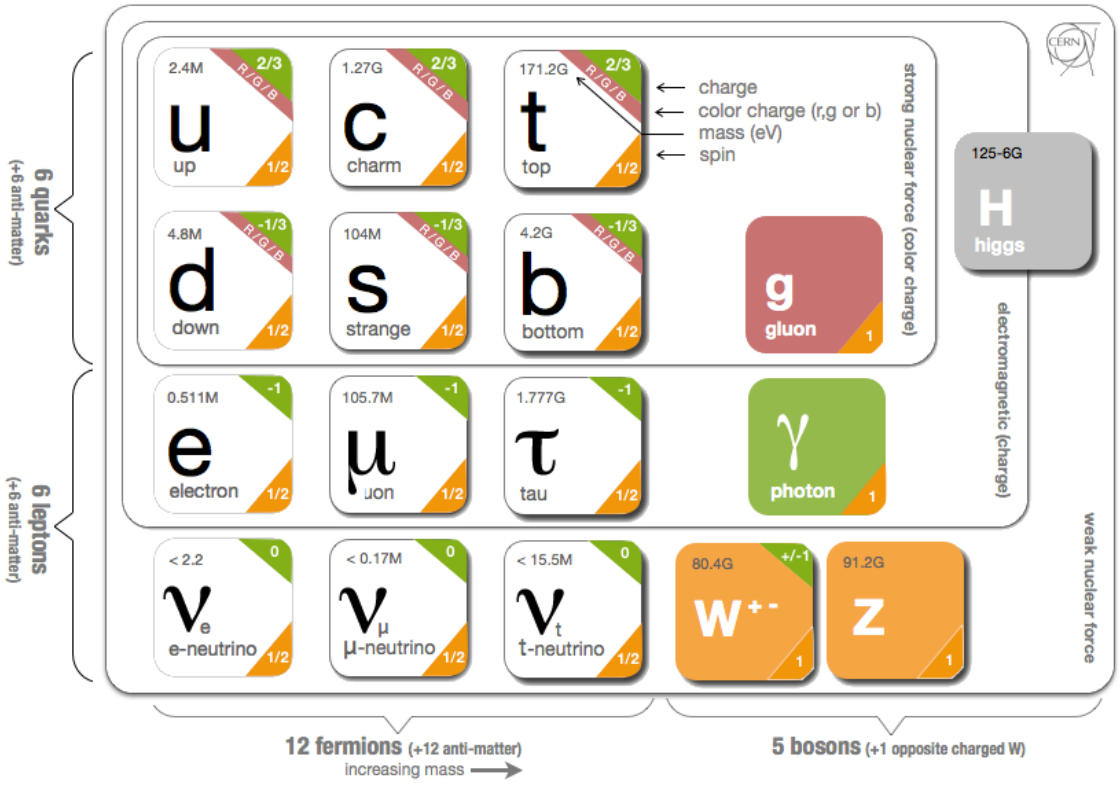

Figure 2.1: Summary of all fundamental fermions and bosons of the Standard Model of particle physics with their most important properties. Figure slightly modified and taken from [17].

a source of background in studies sensitive to physics beyond the Standard Model and thus limits their precision. The following sections ought to briefly introduce the areas and studies, where a better understanding of $\Lambda_b^0 \to D^0 p \mu^- \overline{\nu}_\mu X$ is needed.

The Λ_b^0 is a baryon with the quark content udb and a mass of $(5619.5 \pm 0.4)\,\text{MeV}$ [18]. Among all b baryons it is the lightest one. Hence, it can only decay weakly as the strong and the electromagnetic interactions forbid quark transitions into other flavours. This results in a characteristic, relatively long lifetime of $(1.451 \pm 0.013)\,\text{ps}$ [18], which is helpful for the detection and reconstruction as will be explained later. The b quark decays into a c by the emission of a W^- boson. Subsequently, the W^- boson decays into a muon μ^- and a neutrino $\overline{\nu}_\mu$. With a $u\overline{u}$ pair from the vacuum or an emitted gluon, it is then possible to form a proton p (quark content: uud) and a D^0 meson ($c\overline{u}$) in the final state. Figure 2.2 shows a possible Feynman graph for the decay $\Lambda_b^0 \to D^0 p \mu^- \overline{\nu}_\mu$. The mass of the D^0 meson is $(1864.84 \pm 0.07)\,\text{MeV}$ and of the proton[2] 938.27 MeV [18]. Thus, a particle decaying into a $D^0 p$ must have a mass above the $D^0 p$ mass threshold of about 2803 MeV.

[2]The uncertainty on the proton is negligible compared to the other particles in this analysis.

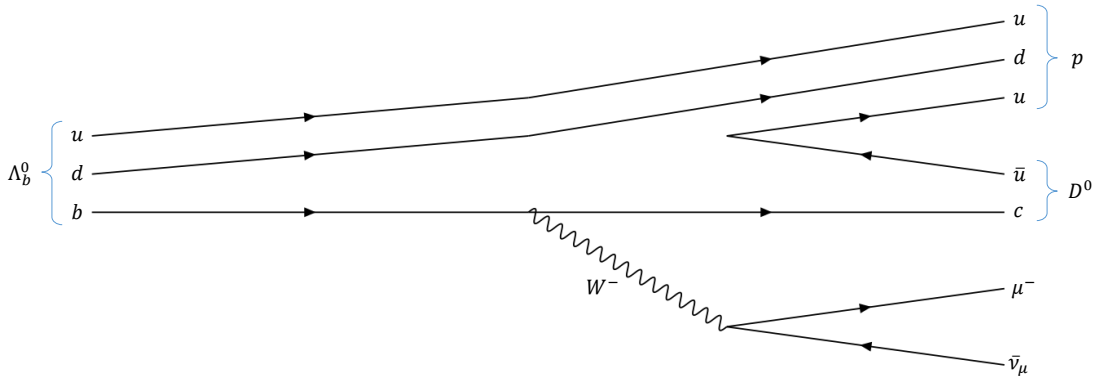

Figure 2.2: Feynman diagram for the decay $\Lambda_b^0 \to D^0 p \mu^- \overline{\nu}_\mu$.

2.2.1 Baryonic spectroscopy

There are plenty of combinatoric possibilities to combine three quarks to a baryon. The constituent quark model predicts seven ground-state baryons with a total angular momentum J and parity P of $J^P = \frac{1}{2}^+$, containing a heavy b quark and two light (u, d or s) quarks: The Λ_b^0 singlet, the Σ_b triplet, the Ξ_b doublet and the Ω_b^- [19]. Except for the Σ_b^0, all these states have been observed. However, the current knowledge of their fundamental properties like masses, widths and quantum numbers is poor as well as only few decay channels have been measured. Thus, there is a big interest in the study of b baryons.

With the transition from a b to a c quark by the emission of a W^- boson, the Λ_b^0 can decay into a Λ_c^+ baryon. The quark content of the Λ_c^+ is udc and thus a representative of a rich spectrum of CHARMED BARYONS. Figure 2.3 shows all known charmed baryons with their quantum number J^P and their observed decays. Again, this spectrum is not complete. A lot of expected charmed baryons are not established and also quantum numbers etc. of established charmed baryons have not been measured so far. In 2006, BaBar reported the observation of the charmed baryon decays $\Lambda_c(2880)^+ \to D^0 p$ and $\Lambda_c(2940)^+ \to D^0 p$ [20]. Thus, the decay $\Lambda_b^0 \to D^0 p \mu^- \overline{\nu}_\mu X$, studied in this thesis offers the possibility to study Λ_c^+ resonances above the $D^0 p$ mass threshold of 2803 MeV by investigating the $D^0 p$ subsystem.

The charmed baryon spectrum in Figure 2.3 resembles the emission spectrum of a hydrogen atom. While the electromagnetic force is responsible for the splitting of the hydrogen's energy levels, the spectroscopy of baryons allows a better understanding of QCD, the theory of the strong interaction. Thus, QCD should be able to describe the dynamics of the baryons and predict their masses. However, due to the rising coupling strength α_s at short distances, QCD cannot be treated perturbatively in the context of baryons. There is no universal approach that solves QCD, but there exist several QCD solutions under specific conditions. Examples for such approaches are Lattice QCD [21] or effective theories like the Heavy Quark Effective Theory (HQET) [8]. The latter one has proven to be useful by the description of b

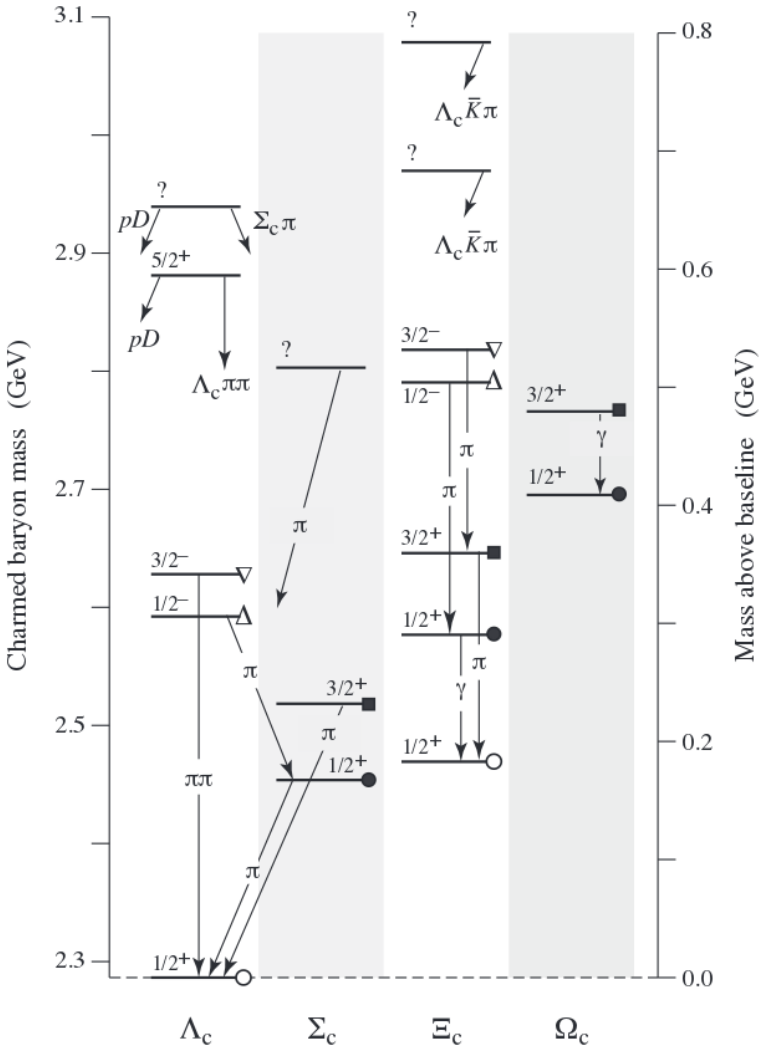

Figure 2.3: Summary of all known and established charmed baryons with quantum numbers J^P and their observed decays. Figure taken from [18].

hadrons. The main principle is that one considers the heavy b quark as static source of the gluon field surrounded by the light quarks. This theoretical simplification in describing the dynamics is analogous to consider a hydrogen atom instead of a positronium [8].

2.2.2 The hunt for New Physics at LHCb

It has already been stated in the introduction, that the Standard Model does not cover and explain all observed phenomena. For instance, gravitation is not included in the Standard model, it does not provide a candidate for dark matter as well as dark energy and the asymmetry between matter and antimatter in the Standard Model is not large enough to fully explain why matter and antimatter have not fully

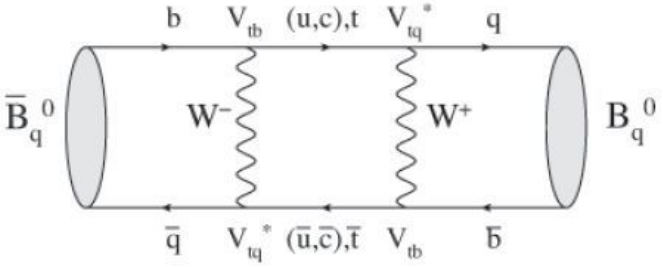

Figure 2.4: One possible Feynman diagram for $B/\overline{B}$ mixing. The q denotes either a d or an s quark. Figure taken from [22].

annihilated after the big bang. All physics that go beyond the Standard Model and try to answer those questions are generally referred to as New Physics (NP).

In principle, there are two ways to discover New Physics: The first one is to directly search for new particles, which is done by ATLAS and CMS. However, one can only discover particles with a mass less than the available centre-of-mass energy $\sqrt{s}$.

The LHCb way of searching for New Physics is an indirect one by the investigation of loop processes such as the $B/\overline{B}$ mixing[3] shown in Figure 2.4. The virtual particles in the loops do not need to satisfy Einstein's energy-momentum relation and thus can have heavier masses than the initial and final state particles. Regarding the B mixing, it is dominated by the top quark with a mass of $m_t = 173.3\,\text{GeV}$ in the loop although the B mass is only $m_B = 5.3\,\text{GeV}$. Thus, it is sensitive to a particle with a mass more than 30 times higher than the B mass and hence the necessary centre-of-mass energy needed for its production. If there exist new heavy particles they might also contribute to such loop processes. By a precise measurement of those, LHCb might find deviations from Standard Model predictions for some variables. Two of them, a_{sl}^d and V_{ub} will be introduced in the following.

2.2.3 Flavour physics and the measurement of $|V_{ub}|$

The flavour eigenstates of the weak interaction $|d'\rangle$, $|s'\rangle$, $|b'\rangle$ are not equal to the mass eigenstates $|d\rangle$, $|s\rangle$, $|b\rangle$. The transformation between those eigenstates is described by the unitary Cabibbo-Kobayashi-Maskawa (CKM) matrix V_{CKM} [23]:

$$\begin{pmatrix} |d'\rangle \\ |s'\rangle \\ |b'\rangle \end{pmatrix} = \begin{pmatrix} V_{ud} & V_{us} & V_{ub} \\ V_{cd} & V_{cs} & V_{cb} \\ V_{td} & V_{ts} & V_{tb} \end{pmatrix} \cdot \begin{pmatrix} |d\rangle \\ |s\rangle \\ |b\rangle \end{pmatrix} . \tag{2.1}$$

The probability that a quark with a mass eigenstate $|j\rangle$ decays into a quark with mass eigenstate $|i\rangle$ is given by $|V_{ij}|^2$. As the CKM matrix is complex, there are in principle 18 free parameters. Due to unitarity constraints and unobservable quark

[3] A brief introduction of meson mixing will follow in the next sections.

phases this number reduces to 4 parameters, which can be measured. A convenient way is to write the CKM matrix in WOLFENSTEIN PARAMETRISATION [24]:

$$V_{\text{CKM}} = \begin{pmatrix} V_{ud} & V_{us} & V_{ub} \\ V_{cd} & V_{cs} & V_{cb} \\ V_{td} & V_{ts} & V_{tb} \end{pmatrix} = \begin{pmatrix} 1 - \frac{\lambda^2}{2} & \lambda & A\lambda^3(\rho - \mathrm{i}\eta) \\ -\lambda & 1 - \frac{\lambda^2}{2} & A\lambda^2 \\ A\lambda^3(1 - \rho - \mathrm{i}\eta) & -A\lambda^2 & 1 \end{pmatrix} + \mathcal{O}(\lambda^4). \tag{2.2}$$

With a value of $\lambda \approx 0.23$ [18], the Wolfenstein parametrisation clearly shows the almost diagonal structure of the CKM matrix, i.e. that quark transitions happen mostly within a generation. The values of the CKM matrix elements are fundamental parameters of the Standard Model, thus their precise measurement and knowledge is important for the search for New Physics. The unitarity of the CKM matrix imposes

$$\sum_j = V_{ij} V_{kj}^* = \delta_{ik} \qquad \text{and} \qquad \sum_i = V_{ij} V_{ik}^* = \delta_{jk}. \tag{2.3}$$

The vanishing combinations can be represented as triangles in a complex plane. Most commonly one uses

$$V_{ud} {V_{ub}}^* + V_{cd} {V_{cb}}^* + V_{td} {V_{tb}}^* = 0. \tag{2.4}$$

After division of Equation (2.4) by $V_{cd} {V_{cd}}^*$, the vertices of the triangle are $(0,0)$, $(0,1)$ and $(\bar{\rho}, \bar{\eta})$ with $\bar{\rho} = \rho(1 - \frac{\lambda^2}{2} + \ldots)$ and $\bar{\eta} = \eta(1 - \frac{\lambda^2}{2} + \ldots)$ as shown on the top part of Figure 2.5.

The aim of flavour physics is to overconstrain the CKM matrix elements. Many loop processes provide the ability to measure the absolute values of V_{ij} or related quantities like the angles α, β, γ of the triangle and are furthermore sensitive to New Physics as explained above. A lot of these results can be displayed and compared in the $(\bar{\rho}, \bar{\eta})$ plane as can be seen on the bottom part of Figure 2.5. A clear sign for New Physics would be for instance, that the triangle is not closed at the vertex of angle α. This is equivalent to the violation of unitarity of the CKM matrix [18, 25].

Currently, there is a large interest in the measurement of $|V_{ub}|$ since it is the least known among the CKM matrix element and there is a deviation of about 3σ between measurements of $|V_{ub}|$ using either exclusive, $B \to \pi \ell \nu_\ell$, or inclusive, $B \to X_u \ell \nu_\ell$, semileptonic decays. Theorists try to explain this discrepancy e.g. with the presence of a right-handed coupling of the W boson as extension to the Standard Model [26]. A recent LHCb study has measured $|V_{ub}|$ for the first time in a baryonic decay, namely $\Lambda_b^0 \to p\mu^- \overline{\nu}_\mu$ and confirmed this incompatibility [11]. The decay $\Lambda_b^0 \to D^0 p\mu^- \overline{\nu}_\mu X$, which is studied in this thesis, is a source of background in the latter $|V_{ub}|$ measurement. The pollution of $\Lambda_b^0 \to p\mu^- \overline{\nu}_\mu$ with $\Lambda_b^0 \to D^0 p\mu^- \overline{\nu}_\mu X$ could only be estimated with simulation. Thus, a better understanding of $\Lambda_b^0 \to D^0 p\mu^- \overline{\nu}_\mu X$ could help to improve the determination of $|V_{ub}|$.

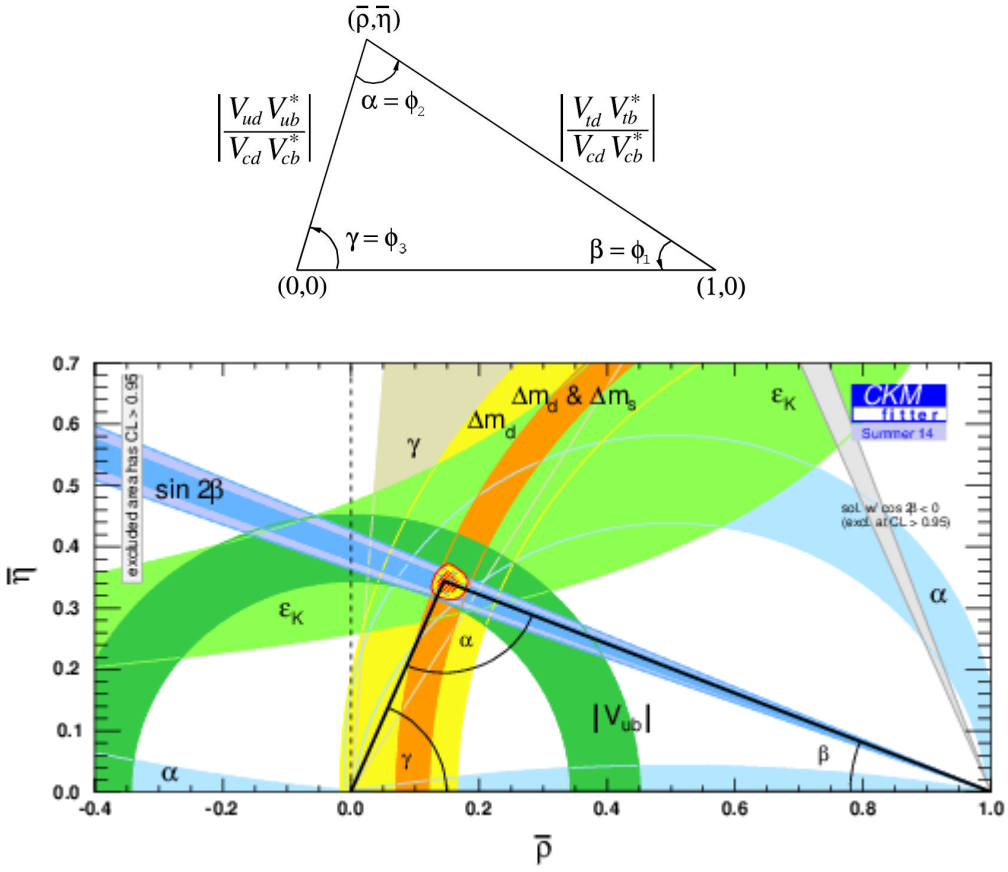

Figure 2.5: Top: Triangle in the complex $(\bar{\rho}, \bar{\eta})$ plane obtained by the unitarity constraint on the CKM matrix in equation (2.4). Bottom: Current status of the CKM matrix with all measured variables included. Figures taken from [18] and [27] respectively.

2.2.4 The measurement of $\mathcal{CP}$ violation in mixing with a_{sl}^d

The symmetry transformation $\mathcal{CP}$ describes a combination of two symmetries: The charge conjugation $\mathcal{C}$ transforms a particle into its antiparticle and the parity operation $\mathcal{P}$ inverts spatial coordinates. If $\mathcal{CP}$ was an exact symmetry, the physical laws would be the same for matter and antimatter. Thus, the creation of our universe requires a violation of the $\mathcal{CP}$ symmetry, otherwise all matter would have been annihilated with antimatter[4]. In the Standard Model, only the weak interaction breaks $\mathcal{CP}$ symmetry. Described by only one parameter, it appears as a single, complex phase in the CKM matrix[5] [23]. However, the $\mathcal{CP}$ violation predicted by the Standard Model is too small to explain the observed matter in the universe. Thus, the measurement of $\mathcal{CP}$ violating observables may reveal New Physics contributions by deviations from the Standard Model predictions.

[4] This requirement is also known as one of the three Sakharov conditions for baryogenesis [28].
[5] Without $\mathcal{CP}$ violation the unitarity triangle would have a vanishing area.

In principle one distinguishes three different kinds of $\mathcal{CP}$ violation [18, 25]:

1. **$\mathcal{CP}$ violation in decay**
   Let M denote a charged or neutral hadron and $\overline{M}$ its $\mathcal{CP}$ conjugate. Their decay amplitudes into a multi-particle final state f or into the $\mathcal{CP}$ conjugated state $\overline{f}$ respectively are defined as

   $$\begin{aligned} A_f &:= \langle f|\mathcal{H}|M\rangle, \qquad & \overline{A}_f &:= \langle f|\mathcal{H}|\overline{M}\rangle, \\ A_{\overline{f}} &:= \langle \overline{f}|\mathcal{H}|M\rangle, \qquad & \overline{A}_{\overline{f}} &:= \langle \overline{f}|\mathcal{H}|\overline{M}\rangle, \end{aligned} \tag{2.5}$$

   where $\mathcal{H}$ denotes the Hamiltonian governing weak interactions. Then, $\mathcal{CP}$ violation in decay is defined by

   $$\left|\frac{\overline{A}_{\overline{f}}}{A_f}\right| \neq 1, \tag{2.6}$$

   i.e. the probability that $\overline{M}$ decays into $\overline{f}$ is different from the probability, that M decays into f.

2. **$\mathcal{CP}$ violation in mixing**
   A neutral meson, e.g. the B^0 meson can oscillate into its antiparticle $\overline{B}^0$ and this $\overline{B}^0$ again back into a B^0. This phenomenon is also called Neutral Meson Mixing and a possible Feynman diagram of the $B^0/\overline{B}^0$ is given in Figure 2.4. The time evolution of the flavour eigenstates $|B^0\rangle$ and $|\overline{B}^0\rangle$ can be phenomenologically described by an effective Schroedinger equation

   $$\mathrm{i}\frac{\mathrm{d}}{\mathrm{d}t}\begin{pmatrix}|B^0\rangle \\ |\overline{B}^0\rangle\end{pmatrix} = \left(M - \frac{\mathrm{i}}{2}\Gamma\right)\begin{pmatrix}|B^0\rangle \\ |\overline{B}^0\rangle\end{pmatrix}, \tag{2.7}$$

   where M is the mass matrix and Γ the decay matrix. Both, M and Γ are Hermitian but not $\mathcal{H} = M - \frac{\mathrm{i}}{2}\Gamma$ due to the possible decay of the mesons. Due to the mixing, it is obvious that $\mathcal{H}$ is not diagonal. After diagonalisation, the mass eigenstates $|B_H\rangle$ and $|B_L\rangle$ can be written in terms of the flavour eigenstates as

   $$|B_{\mathrm{H}}\rangle = p|B^0\rangle - q|\overline{B}^0\rangle \tag{2.8}$$

   $$|B_{\mathrm{L}}\rangle = p|B^0\rangle + q|\overline{B}^0\rangle, \qquad \text{with} \quad |p|^2 + |q|^2 = 1, \tag{2.9}$$

   where the index H (heavy) denotes the mass state with the larger mass compared to the lighter one, indexed with L (light). The coefficients p and q can be related to the mass and decay matrix elements M_{ij} respectively Γ_{ij}, but a thorough discussion of the phenomenology of mixing is beyond the scope of this thesis. $\mathcal{CP}$ violation in mixing means that the probability that a B^0 oscillates into a $\overline{B}^0$ is different from the probability that a $\overline{B}^0$ oscillates into a B^0 or formally

   $$\left|\frac{q}{p}\right| \neq 1. \tag{2.10}$$

3. **$\mathcal{CP}$ violation in interference**
   If there exist final states f, that can be reached from a hadron M as well as from its $\mathcal{CP}$ conjugate $\overline{M}$, $\mathcal{CP}$ violation can occur in the interference between a decay without mixing, $M \to f$, and a decay with mixing, $M \to \overline{M} \to f$. This kind of $\mathcal{CP}$ violation is formally expressed by

   $$\mathcal{I}m(\lambda_f) \neq 0, \tag{2.11}$$

   where λ_f is defined as

   $$\lambda_f := \frac{q}{p}\frac{\overline{A}_f}{A_f}. \tag{2.12}$$

   An example for $\mathcal{CP}$ violation in mixing is the decay $B^0/\overline{B}^0 \to J/\psi\, K^0_{\mathrm{S}}$.

For the measurement of $\mathcal{CP}$ violation it is crucial to know the meson's flavour at decay, for instance if it was a B^0 or a $\overline{B}^0$ meson. A common way to distinguish a B^0 or respectively a $\overline{B}^0$ decay is to use semileptonic decays, since the charge of the lepton contains the information about the meson's flavour: The b quark in the B^0 meson can only decay via the emission of a W^- boson resulting in a negatively charged lepton (and a neutrino), whereas the $\overline{b}$ quark of the $\overline{B}^0$ emits a W^+ when decaying. To measure $\mathcal{CP}$ violation in $B^0/\overline{B}^0$ mixing one defines the SEMILEPTONIC ASYMMETRY a^d_{sl} as

$$a^d_{sl} = \frac{P(\overline{B}^0 \to B^0) - P(B^0 \to \overline{B}^0)}{P(\overline{B}^0 \to B^0) + P(B^0 \to \overline{B}^0)}, \tag{2.13}$$

where P denotes the probability for the transition given in brackets. The Standard Model prediction of $a^d_{sl} = -(4.1 \pm 0.6)10^{-4}$ [29] is tiny compared to the current experimental sensitivity. Thus, the measurement of a^d_{sl} is an excellent probe of the Standard Model and significant deviations from zero would be a signal of New Physics. A current LHCb measurement of a^d_{sl} uses the decays $B^0 \to D^-\mu^+\nu_\mu X$ as well as $B^0 \to D^{*-}\mu^+\nu_\mu X$. The result is $a^d_{sl} = -(0.02 \pm 0.19\,(\mathrm{stat}) \pm 0.30\,(\mathrm{syst}))\%$ and thus consistent with zero at the current precision [10]. With a contribution of $7 \cdot 10^{-4}$, backgrounds coming from Λ^0_b baryon decays make up around 23% of the systematic error. As many Λ^0_b decays have not been measured yet, they had to rely on rough estimates. One of these backgrounds is the decay $\Lambda^0_b \to D^0 p\mu^-\overline{\nu}_\mu X$, which is studied in this thesis. If one misses the proton and randomly adds a pion to the D^0 meson to form a D^* candidate, it mimics a $B^0 \to D^{*-}\mu^+\nu_\mu X$ decay. Thus, the understanding of $\Lambda^0_b \to D^0 p\mu^-\overline{\nu}_\mu X$ helps to improve the measurement of a^d_{sl} by reducing the systematic uncertainties.

2.3 Methods of parameter estimation

This section briefly describes two methods to estimate parameters, which are used in this thesis.

2.3.1 Maximum-Likelihood method

A common task in High Energy Physics is to find the best estimate for a set of parameters $\vec{\theta}$ by a measurement of some variables $\vec{x}$. As an example one wants to measure the mass m_X and the width Γ_X of a particle X decaying into two daughter particles A and B, i.e. $X \to AB$. For this purpose, one measures the energies E and momenta p of the particles A and B in multiple events. Thus, the set of measured variables is $\vec{x} = (E_A, \vec{p}_A, E_B, \vec{p}_B)$ and one determines the "best" value for the parameters $\vec{\theta} = (m_X, \Gamma_X)$. The most frequently used method for the estimate of $\vec{\theta}$ is the Maximum-Likelihood Method. Given a theoretical prediction of the measured distribution in form of a probability density function $f(\vec{x}|\vec{\theta})$ one can define the likelihood function

$$\mathcal{L}(\vec{x}|\vec{\theta}) := \prod_{i=1}^{N} f(\vec{x}_i|\vec{\theta}), \tag{2.14}$$

where N denotes the number of (independent) measurements. The maximum of this likelihood function $\mathcal{L}$ with respect to $\vec{\theta}$ is assumed to be the best estimate of $\vec{\theta}$. Practically one minimises equivalently $-\log(\mathcal{L})$ for computational reasons.

Often, a probability density function P is a linear combination of several components, e.g. a signal P_{sig} and background component P_{bkg}. Thus, the number of events N is a random variable as well. If N obeys the Poisson distribution, the so-called Extended Likelihood Function can be defined as:

$$\mathcal{L}_{\text{ext}}(\vec{x}|N_{\text{sig}}, N_{\text{bkg}}, \vec{\theta}) := \frac{(N_{\text{sig}} + N_{\text{bkg}})^N \exp\left(N_{\text{sig}} + N_{\text{bkg}}\right)}{N!} \prod_{i=1}^{N} \left[f_{\text{sig}} P_{\text{bkg}}(\vec{x}_i|\vec{\theta}) + f_{\text{bkg}} P_{\text{bkg}}(\vec{x}_i|\vec{\theta}) \right], \tag{2.15}$$

where N_j denotes the corresponding yield and $f_j := \frac{N_j}{N}$ the fraction of the signal respectively background component. Thus, the maximisation of the extended likelihood function $\mathcal{L}_{\text{ext}}$ enables to estimate the yields of each component at the same time [18, 30].

2.3.2 Beeston-Barlow method

When one tries to estimate the composition of a data sample, it might happen, that a distribution cannot be described analytically. Thus, one relies on simulations and has to bin the data into n bins. This gives a set of numbers d_i with $i \in [1, n]$, where d_i denotes the number of data events falling into bin i. Let j denote a source contained in the data, P_j its strength and a_{ji} the number of simulated events from source j in bin i, then the predicted number of events in bin i is given by

$$f_i := N_{\text{D}} \sum_{j=1}^{m} \frac{P_j a_{ji}}{N_j}, \tag{2.16}$$

where N_D is the total number of events in the data sample, N_j the number of simulated events of source j and m the number of sources. Starting from a Poissonian distributed probability of observing a particular d_i as

$$\mathrm{e}^{f_i} \frac{f_i^{d_i}}{d_i!} \tag{2.17}$$

the logarithmic likelihood to be maximised looks like

$$\log \mathcal{L} = \sum_{i=1}^{n} \left[d_i \log(f_i) - f_i \right] \tag{2.18}$$

after dropping the constant factorials. This likelihood function is also known as Binned Likelihood.

Nonetheless, the binned likelihood of equation (2.18) does not account for finite sizes of the simulation samples. Due to large computation times simulation samples are often small and there are non-negligible statistical fluctuations in the a_{ji}. Thus the likelihood function has to be modified as follows: The predicted number of events in a bin is now

$$f_i := N_\mathrm{D} \sum_{j=1}^{m} \frac{P_j A_{ji}}{N_j}, \tag{2.19}$$

where A_{ji} is the unknown expected number of events for source j in bin i. The "observed" a_{ji} in the simulation sample is generated from A_{ji} by a Poisson distribution[6]. Thus, the probabilities of observing a set of d_i and a_{ji} have to be combined and the likelihood function to be maximised is

$$\log \mathcal{L} = \sum_{i=1}^{n} \left[d_i \log(f_i) - f_i \right] + \sum_{i=1}^{n} \sum_{j=1}^{m} \left[a_{ji} \log(A_{ji}) - A_{ji} \right]. \tag{2.20}$$

Throughout this analysis, the maximisation of this likelihood function in equation (2.20) is referred to as Beeston-Barlow Method [31].

[6] Actually, the a_{ji} obey a binomial distribution. However, for $A_{ji} << N_j$ it can be approximated by a Poisson distribution.

Chapter 3

The LHCb detector

The Large Hadron Collider (LHC) of the European Organization for Nuclear Research CERN in Geneva, Switzerland is currently the world's most powerful particle accelerator. Having a circumference of 26.7 km, it is designed to either collide protons with a centre-of-mass energy of $\sqrt{s} = 14\,\text{TeV}$ or heavy ions with 2.8 TeV per nucleon [32]. The beams can be brought to collision at four interaction points. At these points, different experiments are placed. Whereas ATLAS and CMS are built as multi-purpose detectors [33, 34] and ALICE studies heavy-ion collisions [35], LHCb is dedicated to study hadrons containing either a heavy b- or c-quark.

Those b- and c-hadrons are mainly produced by gluon-gluon fusion at LHC energies with subsequent hadronisation. These gluons in general carry different momenta leading to a boost of the hadron along the beam-pipe. This is why the LHCb detector is built as a single-arm forward spectrometer. Its layout can be seen in Figure 3.1. It has a forward angular coverage from approximately 10 mrad to 300 mrad in the bending respectively to 250 mrad in the non-bending plane. A right-handed coordinate system is adopted with the z axis along the beam-pipe and the y axis pointing upwards along the vertical. With this choice approximately 25% of all $b\bar{b}$ pairs are produced in the acceptance of the LHCb detector [37] though it covers only 4% of the solid angle as shown in Figure 3.2. The LHCb detector consists of multiple subdetectors and sensors. They can be roughly separated into two groups by their dedicated purpose. They are in principle either used for the reconstruction of particle tracks or to identify the particles and measure their energy. Both groups will be explained in the following.

3.1 Tracking detectors

Tracking describes the whole procedure to reconstruct the trajectories of (charged) particles produced in the proton-proton collision. Together with the dipole magnet that bends charged particles, the particles' charges and momenta can be determined by the deflection of the tracks. The magnet provides a magnetic field of 4 Tm integrated over a length of 10 m. Its main component, the magnetic field in y direction, is shown in Figure 3.7. For the particle tracking, a system of several subdetectors is aligned up- and downstream the dipole magnet, namely the Vertex locator (VELO), the Trigger Tracker (TT) and the Trigger stations (T1-T3) built-up

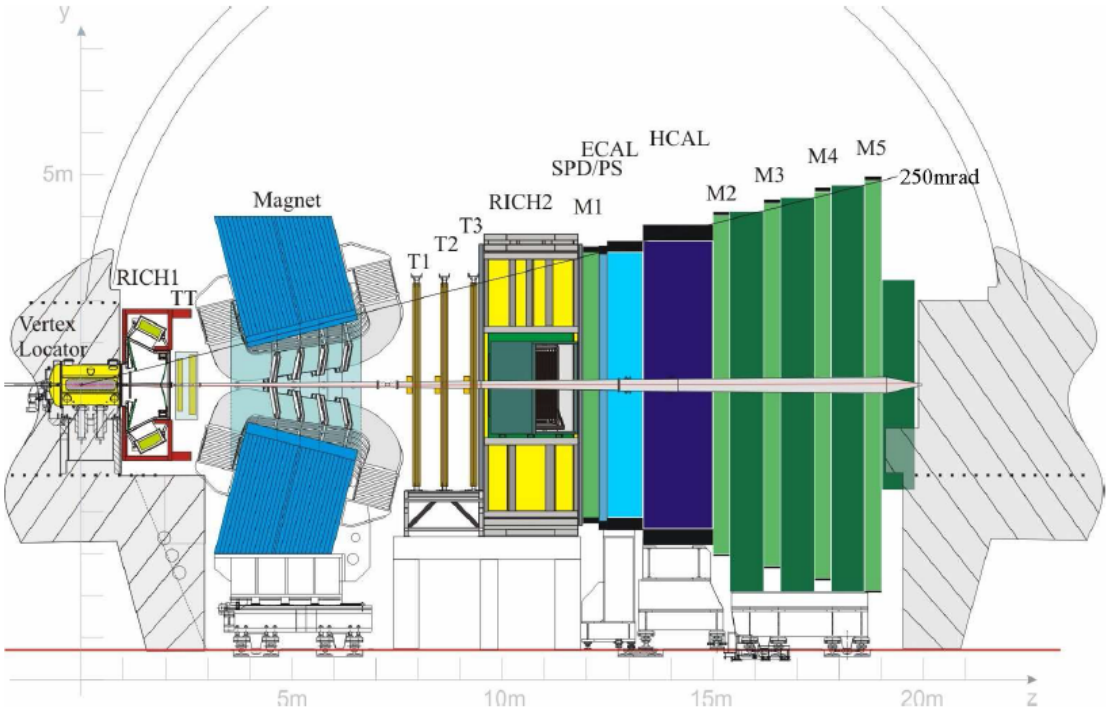

Figure 3.1: Schematic view of the LHCb detector in the $y - z$ plane. Figure taken from [36].

by the Inner Tracker (IT) and the Outer Tracker (OT).

3.1.1 Vertex Locator (VELO)

The VErtex LOcator (VELO) is placed directly around the primary interaction point. Its task is to precisely measure the track coordinates of charged particles and separate the proton-proton interaction point from other vertices, namely either other primary vertices (so called pile-up events) or secondary vertices. The latter ones are typical for b- or c-hadron decays [38] and a good separation and resolution of these vertices is crucial for the LHCb physics programme. An example is the measurement of particles' decay lengths and times for the determination of the rapid $B_s^0 - \overline{B}_s^0$ oscillation frequency [39].

The VELO is built up by silicon modules due to the required high resolution as well as the high particle flux and thus high radiation in the interaction region. It is placed only 7 mm apart from the beam. This is closer than the required aperture of the LHCb beam pipe at injection. Thus, the VELO sensors are made of silicon microstrips shaped as slightly overlapping half-discs. The two halfs can be moved in x- and y-direction to avoid radiation damages unless the beam is stable.

Each module provides a measurement of the r- and ϕ-coordinates. The sensores for these measurements are correspondingly called R- and Φ-sensor, which can be

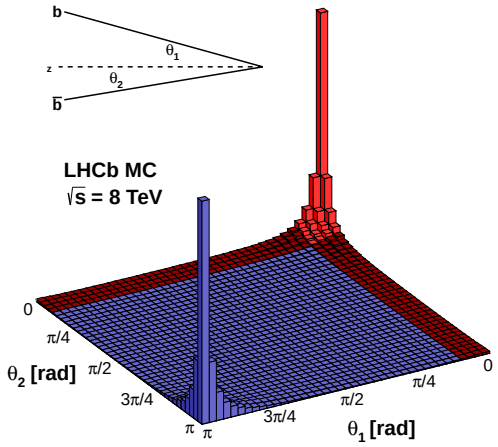

Figure 3.2: Simulation of the $b\bar{b}$ production in pp collisions at $\sqrt{s} = 8\,\text{TeV}$. The angular acceptance of the LHCb detector is coloured in red. Figure taken from [37].

seen in Figure 3.3. An overview over the VELO system with its modules is shown in Figure 3.4. Around the nominal interaction region, the modules are placed closer to each other. Upstream, there are two R sensors dedicated to veto pile-up events. Figure 3.4 furthermore shows the VELO in the closed and opened position.

With this setup, the VELO reaches a track finding efficiency above 98%. Its resolution on vertices is 13 µm in the transverse plane and 71 µm along the beam axis for vertices with 25 tracks. The resolution on the impact parameter is smaller than 35 µm for particles with a transverse momentum larger than 1 GeV [36, 38, 40].

3.1.2 Silicon Tracker (ST)

The Silicon Tracker (ST) uses silicon microstrip detectors with a strip pitch of about 200 µm. It comprises two detectors: the Tracker Truciensis (TT) and the Inner Tracker (IT). The Tracker Turicencis or formerly the Trigger Tracker is located in front of the entrance of the LHCb magnet. It is used for sevaral tasks:

- deliver transverse momentum information for Level-1 trigger,
- reconstruct trajectories of long-lived neutral particles decaying outside the VELO
- reconstruct low-momenta particles bent out by the magnet before reaching the station T1-T3.

The TT consists of one station made of four planes along the beam axis. The first and the fourth layer have vertical readout strips (x layer), while the second (u) and

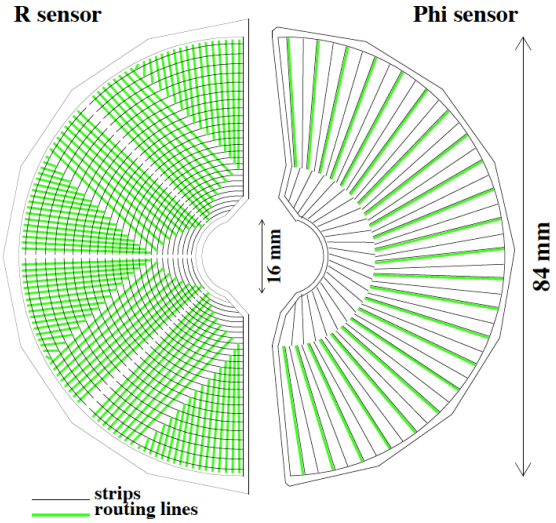

Figure 3.3: Schematic representation of an R and a Φ sensor. The R sensor strips are arranged into four approximately 45° segments and have routing lines perpendicular to the strips. The Φ sensor has two zones with inner and outer strips. The routing lines of the inner strips are orientated parallel to the outer strips. Figure and caption taken from [40].

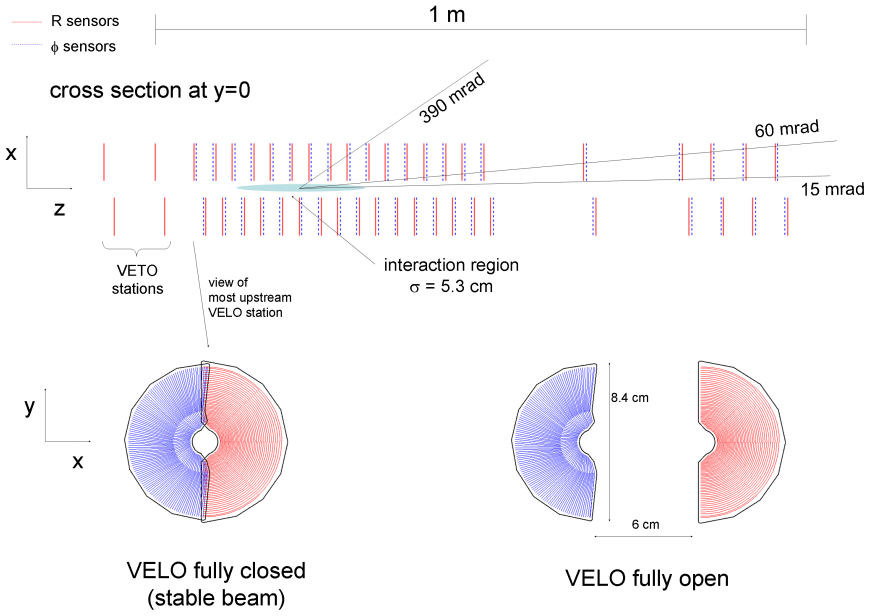

Figure 3.4: Cross section in the (x, z) plane of the VELO silicon sensors, at $y = 0$, with the detector in the fully closed position. The front face of the first modules is also illustrated in both, the closed and opened, positions. The two pile-up veto stations are located upstream of the VELO sensors. Figure and caption taken from [36].

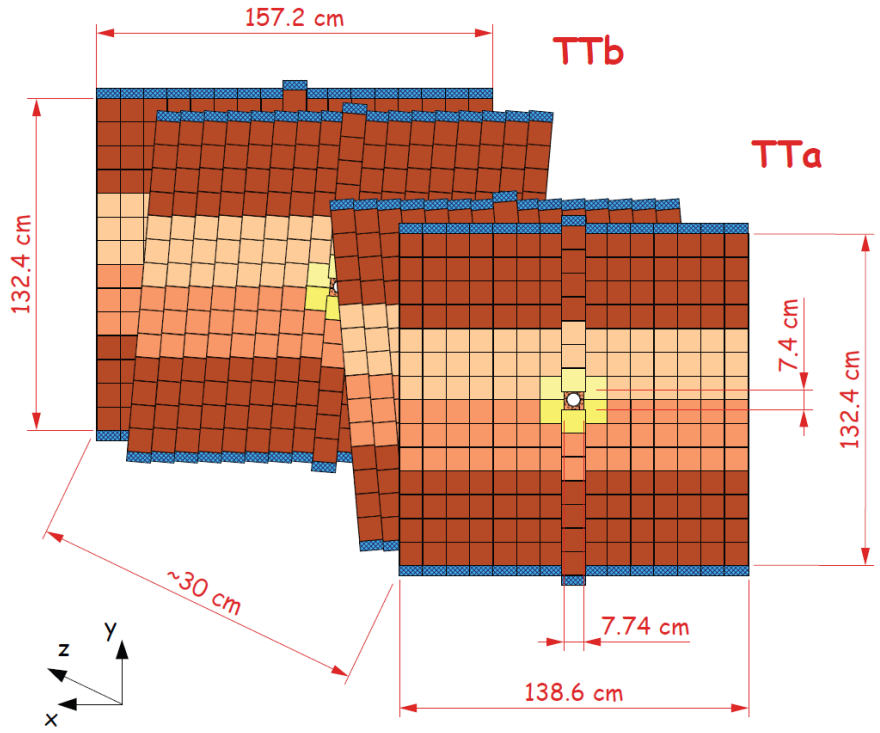

Figure 3.5: Layout of the Tracker Turicensis (TT). Figure taken from [41].

third (v) are rotated by an angle $\pm 5°$ to get a high resolution in the bending plane and additional information in y-direction. Between the u and v layer, there is a gap of around 30 cm. Figure 3.5 shows schematically the layout of the TT. As already mentioned, the Inner Tracker uses the same technology as the TT. It builds the inner part of the three tracking stations T1-T3 (see Figure 3.1), which are located downstream the magnet. Each station consists of four boxes as shown in Figure 3.6. In each box there are again 4 layers, two vertical and two stereo, analogously to the TT. Though the IT only covers 1.3% of the geometrical acceptance, 20% of the track are passing it [36, 41].

3.1.3 Outer Tracker (OT)

The Outer Tracker builds the outer part of the Tracking stations T1-T3 downstream the magnet. It is a gaseous straw tube detector covering an area of approximately $5 \times 6\,\mathrm{m}^2$ with 12 double layers of straw tubes. The straw tubes are filled with a gas mixture of argon (70%), carbon dioxide (28.5%) and oxygen (1.5%). This guarantees a drift time of less than 50 ns enabling to distinguish consecutive proton bunch collisions. Again, the three stations consist of 4 layers each in x-u-v-x geometry. The spatial resolution is 200 µm along the x axis. On the one hand this is worse than the spatial resolution of the IT with 50 µm, but on the other hand the angular coverage is much higher [42].

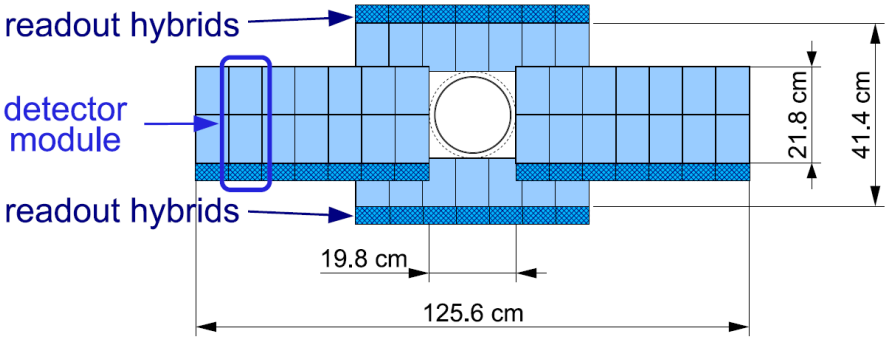

Figure 3.6: Layout of a x detection layer in the second Inner Tracker (IT) station. Figure taken from [36].

3.1.4 Track classification

For the reconstruction of tracks, the registered hits of the VELO, TT, IT and OT are combined to form particle trajectories. Depending on the trajectories one defines different classes of trajectories, which are also sketched in Figure 3.7:

- LONG TRACKS traverse the full tracking system from the VELO to the T stations. Note: Only long tracks are used in this analysis.
- If particles traverse the VELO and TT stations only, their tracks are called UPSTREAM TRACKS.
- Particles decaying outside the VELO acceptance and leaving hits only in the TT and T stations are called DOWNSTREAM TRACKS.
- VELO TRACKS are measured in the VELO only.
- T TRACKS only traverse the T stations.

3.2 Particle identification

The reconstruction of b- and c- hadrons require the identification of the particles associated to the reconstructed tracks. Several facilities for that purpose are available at the LHCb detector, that are described in the following.

3.2.1 Ring Imaging Cherenkov Detector (RICH)

The RICH detectors at LHCb are dedicated to distinguish charged hadrons, especially pions, kaons and protons. They make use of the Cherenkov radiation. If charged particles fly through a dielectric medium with a velocity $\beta = v/c$ that is

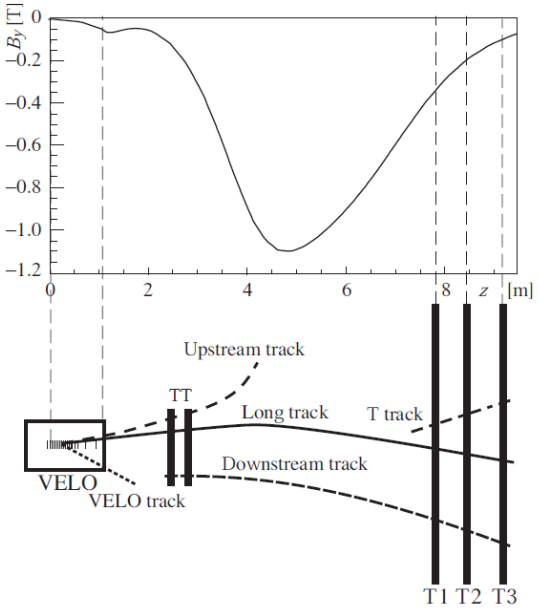

Figure 3.7: A schematic illustration of the various track types: long, upstream, downstream, VELO and T tracks. For reference the main B-field component B_y is plotted above as function of the z coordinate. Figure and caption taken from [43].

faster than the speed of light in that medium, photons are emitted in a cone around their flight path. The opening angle θ_C of that light cone is given by

$$\cos\theta_C = \frac{1}{\beta n}, \tag{3.1}$$

where n denotes the refractive index of the medium [44]. LHCb's RICH detectors measure the opening angle of the Cherenkov cone and use it to determine the velocity. Together with the measured momenta from tracking it is possible to calculate the mass of the particle and thus to identify it. The LHCb detector consists of two RICH detectors. RICH1 is located upstream the magnet before particles might be bent out of the LHCb detector acceptance by the magnet. It contains aerogel and C_4F_{10} gas and is dedicated to measure low-momenta particles between 1 GeV and 60 GeV. However, RICH2 is placed downstream the magnet, filled with CF_4 gas and covers the high-momentum range from 15 GeV to 100 GeV [36, 45].

3.2.2 Calorimeter system

The main purpose of the calorimeter system is to measure the energy of the particles. Furthermore, it provides the identification of electrons, photons and hadrons and delivers trigger signals from photons, electrons and hadrons with high transverse momenta. It contains several subsystems which are all located downstream the magnet.

The first part of the calorimeter system is the scintillating pad detector (SPD). It is used to select charged particles and above all to distinguish between electrons and photons in the subsequent calorimeter parts. After a 2.5 radiation lengths lead wall it is followed by the preshower detector (PS) identifying electromagnetic particles. To measure the energy of electromagnetic particles, the electromagnetic calorimeter (ECAL) is placed behind the PS. It uses the so-called shashlik-technology, i.e. it employs an alternating structure of scintillating tiles and lead plates. The last part of the calorimeter system is the hadronic calorimeter (HCAL). It is a sampling device made of iron as absorber and scintillating tiles as active material and measures the energy of hadrons.

Basically, all calorimeters obey the same principle: Scintillation light is transmitted to a Photo-Multiplier (PMT) by wavelength-shifting fibres. Multianode photomultiplier tubes (MAPMT) read out the single fibres of the SPD / PS cells. Fibre bunches in the ECAL and HCAL modules require individual phototubes [36, 46–49].

3.2.3 Muon chambers

Muons as long-lived and minimum ionising particles can penetrate the whole detector. That is why the muon chambers for the identification of muons are the last part of the detector. There are five muon stations, one (M1) before the calorimeter system and four (M2-M5) behind. To ensure that only muons penetrate the whole system the latter ones are interleaved with 80 cm thick iron absorbers. Besides the inner part of M1, the muon chambers mainly consist of multi-wire proportional chambers (MWPC) providing a fast readout. In the inner part of M1 a gas electron multiplier is used due to the high particle flux [36, 50].

3.3 Trigger

The LHC is designed to collide proton bunches every 25 ns. This is equivalent to a beam crossing rate of 40 MHz. However, it is not possible to record data at this rate. Thus, the task of the LHCb trigger system is to reduce the rate to a recordable level. It has to decide quickly if an event is of interest for the LHCb physics programme. For this purpose, the trigger system is made up of three stages.

The first stage, the Level-0 (L0) trigger, is completely based on hardware. It reduces the beam crossing rate of 40 MHz down to 1 MHz. Due to the high rate, a full event reconstruction is not possible at this stage. Thus, the L0 trigger only tries to reconstruct

- the highest transverse energy E_{T} hadron, electron and photon clusters in the calorimeters,
- the two highest transverse momentum muons in the muon chambers,

because B mesons often produce large transverse momentum respectively energy particles due to their large mass [36]. Furthermore, the pile-up system in the VELO is used to estimate the number of primary pp interactions per bunch-crossing.

The L0 trigger is followed by the software based high-level trigger HLT. The HLT itself is subdivided into the HLT1 and the HLT2. Events passing the L0 trigger enter the HLT1 with a rate of about 1 MHz. Due to limited computing power only a partial event reconstruction using particles in the VELO and T stations is possible. The decision if an event passes the trigger or not is mainly based on the track quality. This reduces the event rate to about 40 kHz and enables HLT2 to fully reconstruct the event. The information of all LHCb subsystems are available at this stage, which allows a more advanced selection. The event rate is reduced to 5 kHz by HLT2, which is low enough to store the data on disk [36, 51, 52].

Chapter 4

Analysis strategy

The aim of this analysis is to measure the branching ratio of the inclusive decay $\Lambda_b^0 \to D^0 p\mu^-\overline{\nu}_\mu X$. The X means, that the Λ_b^0 decays at least into a $D^0 p\mu^-\overline{\nu}_\mu$, but the decay might also include additional particles, e.g. pions. To measure a single branching ratio one needs to know how many Λ_b^0 are produced and how many of them decay via $\Lambda_b^0 \to D^0 p\mu^-\overline{\nu}_\mu$. At a hadron collider like the LHC, it is hard to determine how many particles of a certain kind are produced. In this case one would need to know the $b\bar{b}$ cross section $\sigma(b\bar{b})$ to a high precision, i.e. a measure, how many $b\bar{b}$ quark pairs are produced in a proton-proton (pp) collision. Furthermore, another number one needs to know is how many of these b quarks hadronise to a Λ_b^0. This ratio is called the fragmentation fraction $f_{\Lambda_b^0}$. To avoid these tedious measurements and increase the precision of the result, a normalisation decay, $\Lambda_b^0 \to \Lambda_c^+\mu^-\overline{\nu}_\mu$, is used to rather measure a relative branching ratio,

$$\mathcal{R} = \frac{\mathcal{B}(\Lambda_b^0 \to D^0 p\mu^-\overline{\nu}_\mu X)}{\mathcal{B}(\Lambda_b^0 \to \Lambda_c^+\mu^-\overline{\nu}_\mu)}. \tag{4.1}$$

With this choice $\sigma(b\bar{b})$ and $f_{\Lambda_b^0}$ cancel, since they appear both in the numerator and the denominator. In addition, one has to consider that the D^0 in the signal channel and the Λ_c^+ in the normalisation channel are not directly detected. They decay into more stable particles which are measured and identified in the detector. These subsequent decays are chosen to be $D^0 \to K^-\pi^+$ and $\Lambda_c^+ \to pK^-\pi^+$, because they can be well measured at LHCb. Following the whole decay chain for the signal channel, $\Lambda_b^0 \to D^0 p\mu^-\overline{\nu}_\mu X$, $D^0 \to K^-\pi^+$, and for the normalisation channel, $\Lambda_b^0 \to \Lambda_c^+\mu^-\overline{\nu}_\mu$, $\Lambda_c^+ \to pK^-\pi^+$ one easily sees, that both decays end up in the same final state, namely $pK^-\pi^+\mu^-\overline{\nu}_\mu$. Incidentally, this ensures that potential detection efficiencies, e.g. due to different interaction of particles with the detector material, cancel at first order. Having this in mind, the relative branching ratio splits up to

$$\mathcal{R} = \frac{N_{D^0 p}}{N_{\Lambda_c^+}} \cdot \frac{\epsilon_{\Lambda_c^+}}{\epsilon_{D^0 p}} \cdot \frac{\mathcal{B}(\Lambda_c^+ \to pK^-\pi^+)}{\mathcal{B}(D^0 \to K^-\pi^+)}, \tag{4.2}$$

where, $N_{D^0 p}$ and $N_{\Lambda_c^+}$ denote the signal yields of the channels $\Lambda_b^0 \to D^0 p\mu^-\overline{\nu}_\mu X$ and $\Lambda_b^0 \to \Lambda_c^+\mu^-\overline{\nu}_\mu$ respectively, $\epsilon_{D^0 p}$ and $\epsilon_{\Lambda_c^+}$ are the corresponding reconstruction efficiencies and $\mathcal{B}$ (...) are the branching ratios of the subsequent decays. The

reconstruction efficiencies describe the fact, that not all particle decays are actually detected and reconstructed. Such inefficiencies may have several reasons:

- Each detector has a limited acceptance and a particle may decay outside this acceptance.
- There are dead regions in the detector.
- Selection requirements are applied to suppress background, but usually some signal events are vetoed as well.
- And many more ...

Since the decays of the signal and normalisation channel are semileptonic and thus include a neutrino, which is not reconstructed in the detector, it is not easy to determine the signal yields N_{D^0p} and $N_{\Lambda_c^+}$. The missing neutrino prevents to reconstruct a nice Λ_b^0 mass peak, which would allow an easy distinction between signal and background. Thus, more dedicated methods have to be applied. Regarding Equation (4.2) the analysis proceeds in the following steps:

1. The relevant signal decays have to be reconstructed and selected in the collected data (Chapter 5). Since a huge amount of different particles and decays are produced in a proton-proton (pp) collision, this is an important step to reduce the data size and to separate real signal decays from background.

2. The number of $\Lambda_b^0 \to D^0 p\mu^-\overline{\nu}_\mu X$ events $N_{\Lambda_c^+}$ is determined with a two-dimensional fit to the D^0p mass and the $\log\chi^2_{\mathrm{IP}}$ distribution. The variable $\log\chi^2_{\mathrm{IP}}$ is a measure for the quality of the $D^0p\mu^-$ vertex. It will be thoroughly defined and its choice motivated in Section 6. With, $\log\chi^2_{\mathrm{IP}}$ it is possible to distinguish between nonresonant signal, i.e. Λ_b^0 directly decaying into $D^0p\mu^-\overline{\nu}_\mu$ X without going through intermediate resonances, and background.

3. For the signal event number $N_{\Lambda_c^+}$ in the normalisation channel $\Lambda_b^0 \to \Lambda_c^+\mu^-\overline{\nu}_\mu$, a different approach is chosen. In this channel, the main challenge is to distinguish between $\Lambda_b^0 \to \Lambda_c^+\mu^-\overline{\nu}_\mu$ decays and decays into excited Λ_c^+ states, e.g. $\Lambda_b^0 \to \Lambda_c(2595)^+\mu^-\overline{\nu}_\mu$. These decays can be separated by a fit to the corrected Λ_b^0 mass. The corrected mass is a quantity where one (partially) corrects for the missing neutrino in the decay. A detailed explanation and motivation follows in Chapter 7.

4. As a last step the efficiencies have to be determined. This step makes use of simulations. However, these simulations do not perfectly describe the data, so they first have to be reweighted (Chapter 8).

5. The branching ratios of the subdecays $D^0 \to K^-\pi^+$ and $\Lambda_c^+ \to pK^-\pi^+$ are taken from PDG or other measurements. Their values are $\mathcal{B}(D^0 \to K^-\pi^+) = 0.03880 \pm 0.00050$ [18] and $\mathcal{B}(\Lambda_c^+ \to pK^-\pi^+) = 0.0684 \pm 0.0024$ [53].

6. At this point, all desired observables are obtained and can be used to calculate the relative branching ratio $\mathcal{R}$ in Chapter 12.

Concerning the signal channel $\Lambda_b^0 \to D^0 p \mu^- \overline{\nu}_\mu X$, a special focus is put on the invariant $D^0 p$ mass spectrum. This subsystem allows to do a spectroscopical analysis and study excited Λ_c^+ states. For instance the $\Lambda_c(2880)^+$ appears in this spectrum through the decay chain $\Lambda_b^0 \to \Lambda_c(2880)^+ \mu^- \overline{\nu}_\mu$ and $\Lambda_c(2880)^+ \to D^0 p$. As a side effect of the two-dimensional fit, the masses and the widths of such resonances can be determined if the mass resolution of the detector is known. This is also part of Chapter 7.

Chapter 5

Data reconstruction and selection

The data sample used in this analysis originates from pp collisions and has been recorded in the years 2011 at a center of mass energy $\sqrt{s} = 7\,\text{TeV}$ and 2012 at $\sqrt{s} = 8\,\text{TeV}$, corresponding to an integrated luminosity of $\int \mathcal{L} = 3\,\text{fb}^{-1}$. This chapter describes and motivates the selection criteria for the reconstruction of the decays $\Lambda_b^0 \to D^0 p\mu^-\overline{\nu}_\mu X$ and $\Lambda_b^0 \to \Lambda_c^+\mu^-\overline{\nu}_\mu$[1]. As the D^0 and the Λ_c^+ are not stable enough to be directly indentified and detected, the subsequent decays $D^0 \to K^-\pi^+$ and $\Lambda_c^+ \to pK^-\pi^+$ have been chosen for their reconstruction. These decays leave a clear signature in the detector and can be well reconstructed at LHCb, meaning that the pollution with background is small. Furthermore, with this choice one ends up with the same final state particles for reconstruction in both signal and normalisation channel, namely $pK^-\pi^+\mu^-$. Hence, any inefficiencies due to different interaction of particles with the detector should cancel, at least to first order.

One experimental difficulty arises due to the semileptonic nature of the signal and normalisation channel: The neutrino cannot be reconstructed. Consequently it is not possible to fully reconstruct the Λ_b^0 and to get a Λ_b^0 mass peak for the distinction between signal and background. This leads to a high pollution of the data sample with backgrounds.

5.1 Reconstruction of the decay $\Lambda_b^0 \to D^0 p\mu^-\overline{\nu}_\mu X$

The main strategy in the reconstruction process of the decay $\Lambda_b^0 \to D^0 p\mu^-\overline{\nu}_\mu X$ is to find events with the signature $X_b \to (D^0 \to K^-\pi^+)\mu^-\overline{\nu}_\mu X$, where X_b denotes a b-quark containing hadron, first. Then, a proton track is combined to the $D^0\mu^-$ vertex to make a $\Lambda_b^0 \to D^0 p\mu^-\overline{\nu}_\mu X$ candidate. It is apparent, that a main source of background will be a $B^0/B^+ \to D^0\mu^-\overline{\nu}_\mu X$ decay, where a random proton is added. To better understand the selection criteria and the way, this COMBINATORIAL BACKGROUND is reduced, it might be helpful to have a look at a sketch of a typical $\Lambda_b^0 \to D^0 p\mu^-\overline{\nu}_\mu X$ decay at the left-hand side of Figure 5.1. Due to its relatively long lifetime, it is typical for a Λ_b^0 or in general a b-hadron, that it decays at a so called SECONDARY VERTEX (SV) displaced from the primary pp interaction,

[1] If not stated otherwise, the $\mathcal{CP}$ conjugated decays $\overline{\Lambda}_b^0 \to \overline{D}^0\overline{p}\mu^+\nu_\mu$ and $\overline{\Lambda}_b^0 \to \overline{\Lambda}_c^-\mu^+\nu_\mu$ are included in those samples.

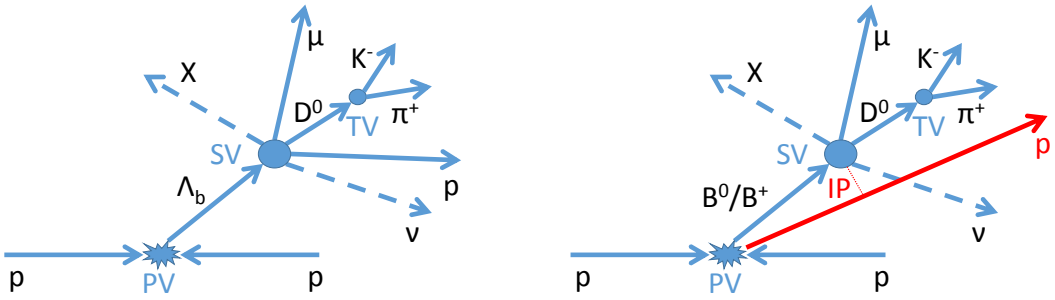

Figure 5.1: Sketch of the decay topology for a typical $\Lambda_b^0 \to D^0 p \mu^- \overline{\nu}_\mu X$ decay (left) and for the background decay $B^0/B^+ \to D^0 \mu^- \overline{\nu}_\mu X$ with a randomly combined proton (right). In these background events, the proton rather poorly makes a vertex with the $D^0\mu^-$ candidate, indicated by a large impact parameter (IP). Particle tracks drawn with a dashed line are not reconstructed. This sketch does neither account for the correct distances between the vertices nor the boost of the particles in z-direction.

the PRIMARY VERTEX (PV). The decay products D^0, μ^- and p originate from the secondary vertex. The neutrino and further possible (especially neutral) particles like pions, denoted as X, are not reconstructed. The D^0 itself lives long enough to decay into a $K^-\pi^+$ at a TERTIARY VERTEX (TV).

Concerning the combinatorial background $B^0/B^+ \to D^0\mu^-\overline{\nu}_\mu X$ with a randomly added proton, there is one important difference to the signal. The proton does not orgin from the secondary vertex but from another source. It should thus have a significant IMPACT PARAMETER (IP) with respect to the primary vertex. The impact parameter is defined as the smallest perpendicular distance between a track and a vertex. An equivalent way is to use the $\log\chi^2_{\text{IP}}$ variable of a given track with respect to a given vertex, which will be very important throughout this analysis. All reconstructed tracks and vertices are fitted in LHCb. From each fit, one can retrieve the fit χ^2 and the corresponding number of degrees of freedom (ndf). The $\log\chi^2_{\text{IP}}$ of the proton is defined as the logarithm of the difference of the $D^0\mu^-$ vertex fit χ^2 with and without the proton, i.e.

$$\log\chi^2_{\text{IP}} := \log\left[\chi^2_{\text{vtx}}(D^0\mu^- p) - \chi^2_{\text{vtx}}(D^0\mu^-)\right]. \tag{5.1}$$

This means the better the proton makes a vertex with the $D^0\mu^-$, the smaller is $\log\chi^2_{\text{IP}}$ and the more likely the event is a real $\Lambda_b^0 \to D^0 p \mu^- \overline{\nu}_\mu X$ decay.

5.1.1 Reconstruction of the D^0 candidate

The first step of the reconstruction process is to reconstruct the D^0. This is supposed to happen via the $D^0 \to K^-\pi^+$ signature. For both, kaon and pion, it is required that their momentum is larger than 2 GeV to ensure, that they are not bent out of the detector by the magnet and that the RICH detectors give reliable results for the

particle idenitification. Their transverse momentum is required to be larger than 300 MeV. This suppresses kaons and pions from the primary interaction, which are usually boosted along the beam pipe, thus having a small transverse momentum. Aside a good track quality quantified with $\chi^2/\text{ndf} < 4$ of the track fit, only tracks with a $\chi^2_{\text{IP}}/\text{ndf} > 4$ with respect to the primary vertex are selected, meaning the kaons and pions are not coming from the primary interaction. LHCb's particle identification system provides a likelihood for a particle hypothesis of each particle candidate. For the pion candidate a likelihood is available, that it is really a pion or that is a kaon and so on. One defines the PIDx variable of a particle candidate, which denotes the difference of the logarithmic likelihoods between the hypotheses, that this particle is of species x and a pion, i.e.

$$\text{PIDx} = \ln \mathcal{L}_x - \ln \mathcal{L}_\pi, \tag{5.2}$$

where $\mathcal{L}_\pi$ denotes the likelihood for the pion hypothesis and $\mathcal{L}_x$ for particle x respectively. The higher PIDx, the more likely the candidate is really a particle x[2]. For the kaon candidate, a PIDK > 4 and for the pion candidate a PIDK < 10 is required. At first glance, it might be confusing why the requirement on the pion's PIDK is so loose. In a pp collision, there are many more pions produced than kaons. Thus, it is much more likely that a pion is misidentified as a kaon and the requirement on the PIDK needs to be tight. However, for pions most of the background are pions, too. Hence, there is less motivation to apply requirements on the pion PID. The pion and kaon candidates and their tracks are now combined to a D^0 candidate with a good vertex quality of $\chi^2_{\text{vtx}}/\text{ndf} < 6$. Another variable one defines for the reconstruction is DIRA. It is defined as the cosine of the angle α between the direction of flight of a particle from some reference vertex and its momentum. If the detector resolution was perfect, DIRA would be one ($\alpha = 0$). Requiring a DIRA close to one ensures, that the assigned momentum and flight direction match to each other. The flight direction is determined by the connection of the reference vertex and the decay vertex of the particle. Throughout this selection, all DIRA requirements are calculated with respect to the primary vertex. Thus, the DIRA requirements on particles not coming from the primary vertex like the D^0 in this case have to be a bit looser as e.g. for the Λ_b^0, which is directly produced at the primary vertex. For the reconstruction of the D^0, events with a DIRA > 0.99 of the D^0 are selected. As last requirement one suppresses combinatorial background by restricting the D^0 to be close to its mean mass, i.e. the mass difference to the PDG value is smaller than 25 MeV and to require a minimum D^0 flight distance with respect to the primary vertex of 5 mm. Figure 5.2 shows the invariant mass of the reconstructed D^0 candidates after the application of all the requirements except for the restriction of the D^0 mass itself. A clear mass peak with very small sidebands indicating a small combinatorial background contribution can be seen.

[2]Throughout this thesis x is either mu for muons, p for protons and K for kaons.

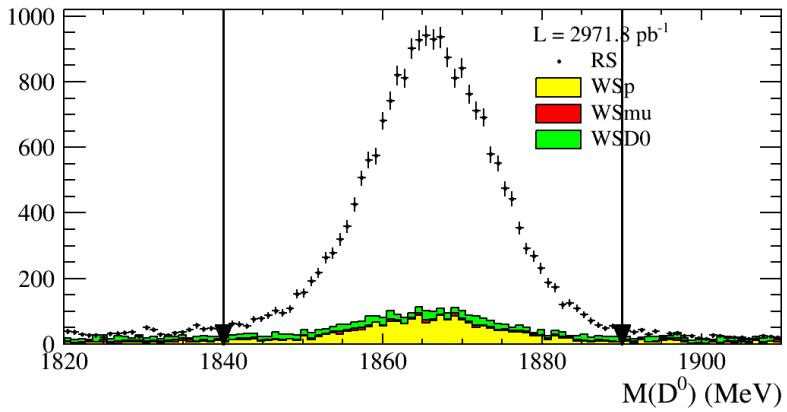

Figure 5.2: Invariant D^0 mass after the application of all selection requirements except for the D^0 mass itself. The arrows indicate where the selection requirements are applied. The colour-shaded areas shows the respective distributions for wrong sign (WS) combinations. A definition and explanation of wrong sign combinations is given at the end of section 5.1.3.

5.1.2 Reconstruction of the $D^0\mu^-$ candidate

Having reconstructed the D^0 candidate, one needs a muon track to combine them. The motivation for the requirements on the muon track is analagous to the kaon and pion for the D^0 reconstruction. Thus they will be just briefly mentioned: The muon is required to have a minimum transverse momentum of 1.2 GeV and a minimum momentum of 6 GeV. The track χ^2/ndf is smaller than 4 and the χ^2_{IP} with respect to the primary vertex larger than 9. PIDmu is required to be greater than 0.3. It might happen, that several hits in the detector are incidentally combined to a track albeit coming from different tracks. The so called ghost probablity gives a measure of this issue and is required to be less than 0.5 for the muon track.

For the combination of D^0 and μ^- the vertex shall be again of good qualitiy, i.e. $\chi^2_{\text{vtx}}/\text{ndf} < 3$. To avoid completely random combinations the invariant $D^0\mu^-$ mass is required to be between 2.2 and 8.0 GeV and to have a minimum transverse momentum of 3 GeV. The minimum DIRA of the $D^0\mu^-$ candidate is 0.999. With a requirement on the flight distance χ^2 to be greater than 25 it is ensured, that the $D^0\mu^-$ decay vertex is certainly displaced form the primary vertex.

5.1.3 Reconstruction of the Λ_b^0 ($D^0\mu^-p$) candidate

The proton's momentum and transverse momentum is required to be larger than 15 GeV and 1 GeV respectively for a good particle identification and to exclude protons boosted from the primary interaction. To reduce the amount of fake protons, i.e. pions or kaons that are misidentified as protons, tight particle identification requirements are applied: PIDp > 10 and PIDp$-$PIDK > 10. Having the definition

of the PIDx variable in Equation 5.2 in mind, PIDx serves always as distinction between a particle x and a pion. Thus, the difference between PIDp and PIDK enables for a better distinction between protons and kaons, since

$$\begin{aligned}\text{PIDp} - \text{PIDK} &= (\ln \mathcal{L}_p - \ln \mathcal{L}_\pi) - (\ln \mathcal{L}_K - \ln \mathcal{L}_\pi) \\ &= (\ln \mathcal{L}_p - \ln \mathcal{L}_K)\,.\end{aligned}$$

The χ^2_{IP} with respect to the primary vertex is greater than 25, since the proton must not come from the primary vertex. In contrast, the proton should make a good vertex with the $D^0\mu^-$ candidate. It is thus required that the $\log \chi^2_{\text{IP}}$ of the proton with respect to the $D^0\mu^-$ vertex is smaller than 1. It should be noted, that throughout this thesis, the label $\log \chi^2_{\text{IP}}$ without further specifications refers to this variable. This last requirement on $\log \chi^2_{\text{IP}}$ is not applied in the signal fit to distinguish nonresonant signal and background as will be thoroughly explained in Chapter 6.

For the combined $D^0\mu^- p$ candidate, the requirement on the angle α between flight direction and momentum is the tightest compared to the daughter candidates. This is obvious since the impact of the detector resolution leading to a discrepancy between flight direction and momentum should be the smallest for the first decay of the decay chain. An angle $\alpha < 0.015$ is required, which is equivalent to a DIRA $\gtrsim 0.999999$.

As stated at the beginning of this chapter, the information on the neutrino is missing in the reconstruction. Thus, the reconstructed Λ_b^0 mass is smeared out and does not peak at the nominal Λ_b^0 mass of 5619.5 MeV. However, there are different ways to at least partially account for the missing neutrino. One of them is the so called CORRECTED MASS of the Λ_b^0. It is defined as

$$m_{\text{corr}} = \sqrt{m^2_{D^0\mu^- p} + p_\perp^2} + p_\perp, \tag{5.3}$$

where $m_{D^0\mu^- p}$ denotes the invariant mass of the $D^0\mu^- p$ candidate and $p_\perp$ its transverse momentum perpendicular to the Λ_b^0 flight direction, which is measured by the connection of the primary vertex and the Λ_b^0 decay vertex [54]. It is the minimum correction to the Λ_b^0 candidate if any daughters are missing. If only a massless particle is missed, the corrected mass would be the mass of the Λ_b^0 [55]. This can be seen as follows: In the rest frame of the Λ_b^0, the Λ_b^0 mass can be written as

$$\begin{aligned} m_{\Lambda_b^0} &= E_{\text{vis}} + E_{\text{miss}} && (5.4)\\ &= \sqrt{M^2_{\text{vis}} + p^2_{\perp,\text{vis}} + p^2_{\parallel,\text{vis}}} + \sqrt{M^2_{\text{miss}} + p^2_{\perp,\text{miss}} + p^2_{\parallel,\text{miss}}}, && (5.5)\end{aligned}$$

where the index vis denotes the respective quantities of the visible, i.e. reconstructed particles and miss the ones of the missing particles. If the missing particle is massless and if one changes to the Λ_b^0 rest frame, where $p_{\perp,\text{vis}} = p_{\perp,\text{miss}} = p_\perp$ and $p_{\parallel,\text{vis}} = p_{\parallel,\text{miss}} = p_\perp$ the Λ_b^0 mass becomes

$$m_{\Lambda_b^0} = \sqrt{M^2_{\text{vis}} + p_\perp^2 + p_\parallel^2} + \sqrt{p_\perp^2 + p_\parallel^2}. \tag{5.6}$$

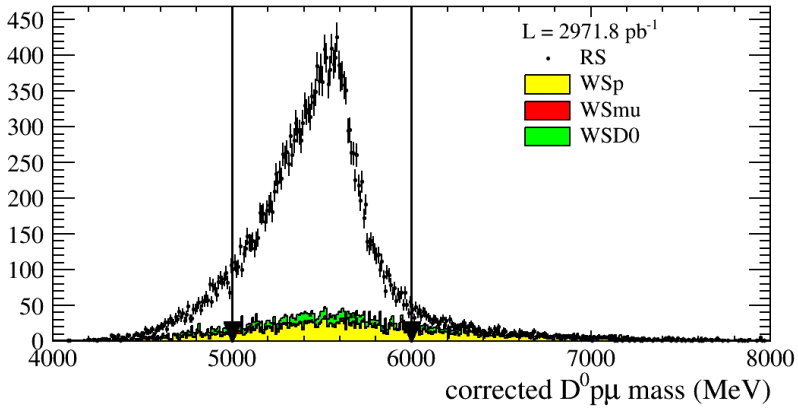

Figure 5.3: Corrected Λ_b^0 mass after the application of all selection requirements except for the corrected Λ_b^0 mass itself. The arrows indicate where the selection requirements are applied. The colour-shaded areas shows the respective distributions for wrong sign (WS) combinations. The corrected Λ_b^0 mass tends to peak near the nominal Λ_b^0 mass of $M(\Lambda_b^0) = (5619.5 \pm 0.4)\,\mathrm{MeV}$ [18].

Furthermore, if the longitudinal momentum can be ignored in the present rest frame the Λ_b^0 mass is described by the corrected mass m_{corr} [56, 57]. Hence, it is required that the corrected Λ_b^0 mass lies around its PDG mass $M(\Lambda_b^0) = (5619.5 \pm 0.4)\,\mathrm{MeV}$ [18] between 5 and 6 GeV. Figure 5.3 shows the distribution of the corrected Λ_b^0 mass. Due to the correction of the missing neutrino it peaks near the PDG mass as explained above.

Another background might be the decay $\Lambda_b^0 \to D^0 p\pi^-$, where the pion is misidentified as muon. In this case, all final state particles are reconstructed and the invariant $D^0\mu^- p$ mass peaks around the Λ_b^0 mass. To veto such backgrounds only events with an invariant $D^0\mu^- p$ mass of less than 5.5 GeV are selected. A detailed discussion of these backgrounds can be found in Chapter 9, especially Figure 9.3 visualises this veto.

Table 5.1 summarises all selection requirements mentioned in the last sections. After the reconstruction and application of these requirements, there are in total 21444 $\Lambda_b^0 \to D^0 p\mu^-\overline{\nu}_\mu X$ candidates left for the analysis. In the nominal signalfit, the cut on $\log\chi^2_{\mathrm{IP}}$ is not applied. In this case, there are 34760 candidates available. Figure 5.4 shows the invariant $D^0 p$ mass (top) and the $\log\chi^2_{\mathrm{IP}}$ distribution (bottom). The first one is used for a spectroscopical analysis later. If this thesis refers to the (invariant) $D^0 p$ mass, there is actually the quantity $M(D^0 p) - M(D^0) + M_{\mathrm{PDG}}(D^0)$ meant, where one first subtracts the reconstructed D^0 mass and then adds up the nominal D^0 mass from the PDG. With this trick, one “subtracts" the finite width of the D^0 from the $D^0 p$ mass spectrum and thus improves the mass resolution especially at $D^0 p$ mass threshold. Some peaking structures can be seen in the spectrum, indicating that the decay $\Lambda_b^0 \to D^0 p\mu^-\overline{\nu}_\mu X$ might happen via intermediate

Table 5.1: Summary of the selection requirements for the decay $\Lambda_b^0 \to D^0 p \mu^- \overline{\nu}_\mu X$.

	Variable	Value
Event	number of long tracks	< 250
μ^-	Momentum	$> 6\,\text{GeV}$
	Transverse momentum	$> 1.2\,\text{GeV}$
	Ghost probability	< 0.5
	Track χ^2/ndf	< 4
	χ^2_{IP} w.r.t. PV	> 9.0
	PIDmu	> 0.3
$D^0 \to K^-\pi^+$	Daughter momentum	$> 2\,\text{GeV}$
	Daughter transverse momentum	$> 300.0\,\text{MeV}$
	Daughter ghost probablity	< 0.5
	Daughter track χ^2/ndf	< 4
	Daughter χ^2_{IP} w.r.t. PV	> 4
	K^- daughter PIDK	> 4
	π^+ daughter PIDK	< 10
	χ^2_{vtx}/ndf	< 6
	DIRA w.r.t. PV	> 0.99
	Mass difference to PDG	$< 25\,\text{MeV}$
	Flight distance w.r.t. PV	$> 5\,\text{mm}$
$D^0\mu^-$	Mass	$\in [2.2, 8.0]$ GeV
	χ^2_{vtx}/ndf	< 3
	DIRA w.r.t. PV	> 0.999
	Flight distance χ^2 w.r.t. PV	> 25
	Transverse momentum	$> 3000\,\text{MeV}$
p	χ^2_{IP} w.r.t. PV	> 25
	PIDp−PIDK	> 10
	PIDp	> 10
	Momentum	$> 15\,\text{GeV}$
	Transverse momentum	$> 1\,\text{GeV}$
	$\log \chi^2_{\text{IP}}$ w.r.t. $D^0\mu^-$ vertex	< 1
$D^0\mu^- p$	arccos(DIRA) w.r.t. PV	< 0.015
	Mass	$< 5.5\,\text{GeV}$
	Corrected mass	$\in [5, 6]$ GeV

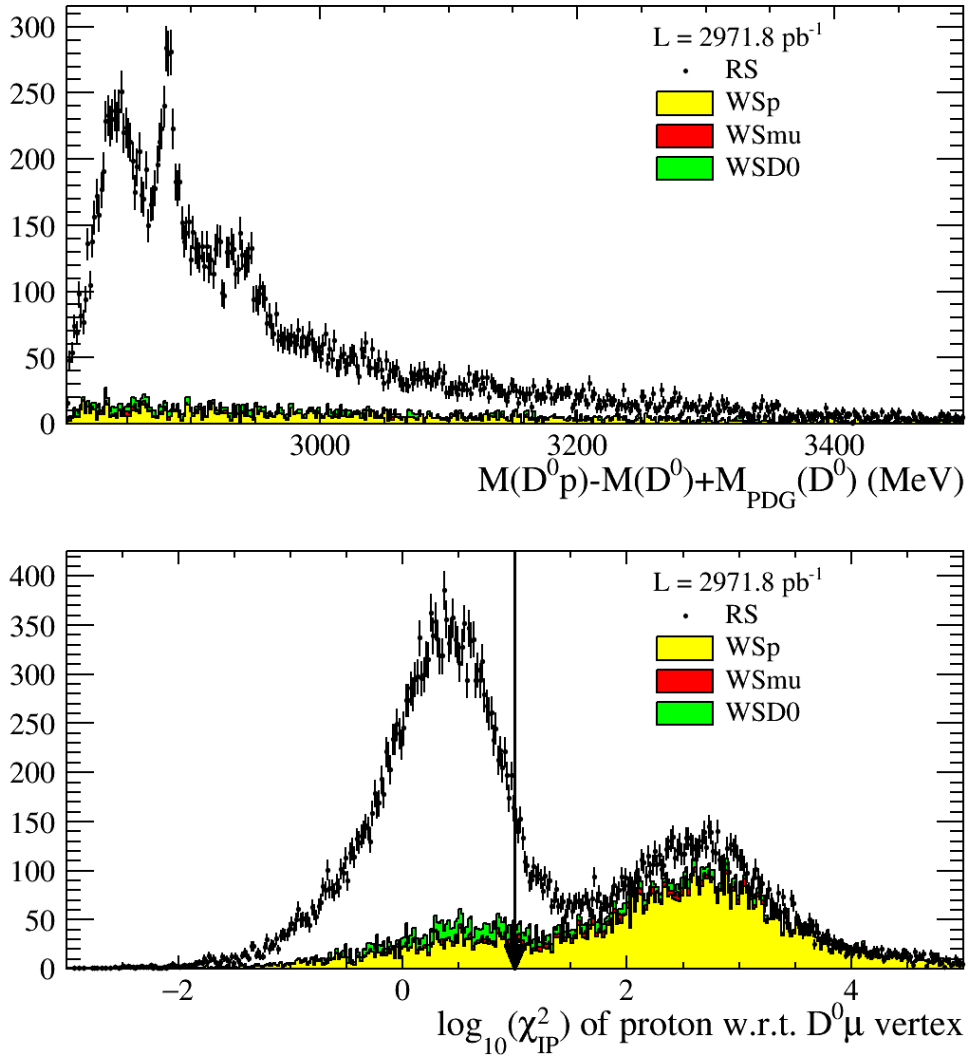

Figure 5.4: Invariant D^0p mass (top) after the application of all selection requirements and $\log\chi^2_{\mathrm{IP}}$ distribution (bottom) after all requirements except for $\log\chi^2_{\mathrm{IP}}$ itself. The arrow in the $\log\chi^2_{\mathrm{IP}}$ distribution indicates where the selection requirement is applied. The colour-shaded areas shows the respective distributions for wrong sign (WS) combinations.

resonances. There is furthermore a broad distribution under the peaks. This is assumed to be either background or nonresonant signal. For their distinction, the $\log \chi^2_{\mathrm{IP}}$ distribution is used. The plot confirms the explanation above: Background events tend to peak at higher $\log \chi^2_{\mathrm{IP}}$ than signal events. This is justified by the so called WRONG SIGN (WS) combinations. To the physical decay $\Lambda_b^0 \to D^0 p \mu^- \overline{\nu}_\mu X$ there are also samples produced with one charge conjugated daughter particle in the final state. There are three possibilities of combining a wrong sign particle:

- **WSp:** $D^0 \overline{p} \mu^-$ final state
- **WSD0:** $\overline{D}^0 p \mu^-$ final state
- **WSmu:** $D^0 p \mu^+$ final state

There is no physical process that allows the decay of a Λ_b^0 into these final states. The most apparent violation of a physical law in these decays is the charge conservation. Whereas the Λ_b^0 is electrically neutral, the final states of WSp and WSmu have a total charge of ∓ 2. For the WSD0 combinations, the electrical charge is fine, but the decay $\Lambda_b^0 \to \overline{D}^0 p \mu^-$ would require the quark transition $b \to \bar{c}$, which is forbidden in the Standard Model. Thus if one reconstructs such unphysical decays these either arise due to random combinations of particle tracks or due to true physical decays, where one misidentifies a particle. As example for the latter case serves a decay like $B^0 \to D^0 \mu^- \pi^+ \pi^+ \pi^0$ where one misidentifies the π^0 as $\overline{p}$ and misses the two π^+. Being caused by either random combinations or misidentification of particles, the wrong sign events provide a first, rough estimate of the $\Lambda_b^0 \to D^0 p \mu^- \overline{\nu}_\mu X$ background behaviour.

5.2 Reconstruction of the decay $\Lambda_b^0 \to \Lambda_c^+ \mu^- \overline{\nu}_\mu$

The reconstruction of the $\Lambda_b^0 \to \Lambda_c^+ \mu^- \overline{\nu}_\mu$ channel with $\Lambda_c^+ \to p K^- \pi^+$ is done quite similarly to the decay $\Lambda_b^0 \to D^0 p \mu^- \overline{\nu}_\mu X$. The main difference between those two channels is, that the proton is now combined with the $K^- \pi^+$ to make a $\Lambda_c^+ \to p K^- \pi^+$ candidate instead of being combined with the $D^0 \mu^-$. As to the rest, the topology is analogous to $\Lambda_b^0 \to D^0 p \mu^- \overline{\nu}_\mu X$. The lifetime of the Λ_b^0 is long enough, such that the Λ_b^0 decays at a secondary vertex into a Λ_c^+ and μ^-. Like the D^0, the Λ_c^+ flies another distance, finally decaying at a tertiary vertex into $p K^- \pi^+$. The strategy for the selection is thus to find decays with the signature $X_b \to (\Lambda_c^+ \to K^- \pi^+ p^+) \mu^- \bar{\nu}_\mu X$.

5.2.1 Reconstruction of the Λ_c^+ ($pK^-\pi^+$) candidate

First of all, requirements on the tracks of the final state particles p, K and π are made. These are required to have a minimum momentum of 2 GeV and a transverse momentum of 250 MeV, their ghost probability should be less than 0.5 and the χ^2_{IP} with respect to the primary vertex is greater than 4. The motivation for these cuts

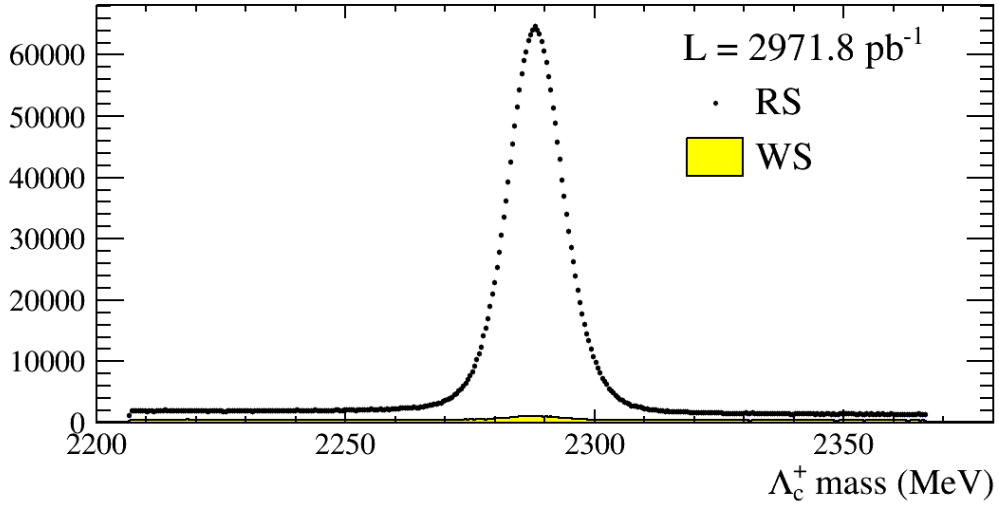

Figure 5.5: Plot of the invariant $pK^-\pi^+$ mass distribution. A clear mass peak identified as the Λ_c^+ can be seen. The yellow shaded area shows events with the WS combination $\Lambda_c^+\mu^+$.

are the same as for the D^0 reconstruction in Section 5.1.1: a good vertex quality, tracks not pointing to the primary vertex, good kinematics for particle identification and for not being bent out by the magnet. To be compatible to the $\Lambda_b^0 \to D^0 p\mu^-\overline{\nu}_\mu X$ decay and to ensure a similar reconstruction of the proton, the requirements on the proton are adopted from the $\Lambda_b^0 \to D^0 p\mu^-\overline{\nu}_\mu X$ reconstruction: A minimum momentum of 15 GeV, a minimum transverse momentum of 1 GeV and a minimum χ^2_{IP} with respect to the primary vertex of 25 is required. Furthermore fake protons are suppressed by demanding PIDp > 10 and PIDp$-$PIDK > 10. The kaon must satisfy PIDK > -5 and the pion PIDK < 20.

For the combined $pK^-\pi^+$, i.e. Λ_c^+ candidate, the vertex must be of good quality, guaranteed by $\chi^2_{\text{vtx}}/\text{ndf} < 3$. Its DIRA is required to be larger than 0.99 to match flight direction and momentum. The difference of the Λ_c^+ mass to its PDG value is required to be smaller than 80 MeV only, since the Λ_c^+ sidebands are later used to subtract combinatorial backgrounds below the Λ_c^+ mass peak. Aside from a minimum transverse momentum of 2.1 GeV, PROMPT Λ_c^+, i.e. Λ_c^+ directly coming from the primvary vertex, are supressed by requiring the logarithm of the Λ_c^+ impact parameter to be grater than -1.5 and a flight distance χ^2 of more than 25, both with respect to the primary vertex. Figure 5.5 shows a clear peak of the invariant Λ_c^+ mass.

5.2.2 Reconstruction of the Λ_b^0 ($\Lambda_c^+\mu^-$) candidate

The reconstruction of the muon track is completely analogous to the description in Section 5.1.2 and hence not discussed here again. The combined $\Lambda_c^+\mu^-$, i.e. the

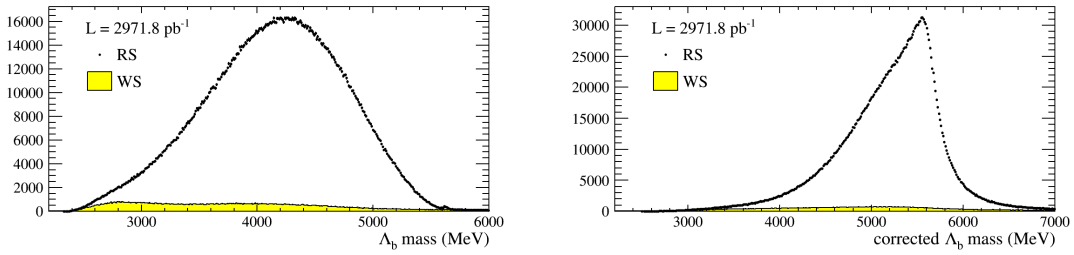

Figure 5.6: Plot of the invariant Λ_b^0 mass distribution (left) and of the corrected Λ_b^0 mass (right). Due to the missing neutrino the Λ_b^0 mass peak is shifted to lower masses compared its nominal mass of 5619.5 MeV. With the correction for the missing neutrino, the peak is close to the nominal Λ_b^0 mass. The yellow shaded area shows events with the WS combination $\Lambda_c^+ \mu^+$.

Λ_b^0 candidate should make a good vertex with a maximum χ^2_{vtx} of 6. Its DIRA is required to be larger than 0.999. Being a semileptonic decay again, only a loose selection on the invariant $\Lambda_c^+ \mu^-$ mass can be applied. It must have a mass between 2.2 and 8.0 GeV.

Compared to $\Lambda_b^0 \to D^0 p \mu^- \overline{\nu}_\mu X$, main backgrounds are not assumed to be of combinatorial nature, but rather Λ_b^0 decays into excited Λ_c^+ states. A good example is the decay $\Lambda_b^0 \to \Lambda_c(2595)^+ \mu^- \overline{\nu}_\mu$ with $\Lambda_c(2595)^+ \to \Lambda_c^+ \pi^0$, where the π^0 is not reconstructed. Its decay topology does not differ from $\Lambda_b^0 \to \Lambda_c^+ \mu^- \overline{\nu}_\mu$, because the $\Lambda_c(2595)^+$ decays immediately. However, if the massive π^0 is missing in addtion, the corrected Λ_b^0 mass should be shifted to lower masses compared to $\Lambda_b^0 \to \Lambda_c^+ \mu^- \overline{\nu}_\mu$. That is why there is not any requirement made on the Λ_b^0 corrected mass here. The different behaviour of the corrected masses is used in the normalisation fit in Chapter 7 to disentangle the signal from those backgrounds.

Table 5.2 summarises all requirements for the reconstruction of the $\Lambda_b^0 \to \Lambda_c^+ \mu^- \overline{\nu}_\mu$ candidates. After application of all these requirements there are in total 2670999 $\Lambda_b^0 \to \Lambda_c^+ \mu^- \overline{\nu}_\mu$ candidates left for the further analysis. Figure 5.6 shows on the left-hand side the invariant mass distribution of the Λ_b^0 candidates and on the right-hand side the corrected Λ_b^0 mass distribution. Whereas the Λ_b^0 mass is shifted to lower masses due to the missing neutrino, the corrected mass peaks close to the PDG mass of about 5619.5 MeV [18].

Table 5.2: Summary of the selection requirements for the reconstruction of $\Lambda_b^0 \to \Lambda_c^+ \mu^- \overline{\nu}_\mu$ candidates.

	Variable	Value
Event	number of long tracks	< 250
μ^-	Transverse momentum	$> 1\,\text{GeV}$
	Momentum	$> 6\,\text{GeV}$
	Ghost probability	< 0.5
	Track χ^2/ndf	< 4
	χ^2_{IP} w.r.t. PV	> 9.0
	PIDmu	> 0.3
$\Lambda_c^+ \to pK^-\pi^+$	Daughter momentum	$> 2\,\text{GeV}$
	Daughter transverse momentum	$> 250.0\,\text{MeV}$
	Daughter ghost probability	< 0.5
	Daughter χ^2_{IP} w.r.t. PV	> 4.0
	p daughter PIDp	> 10
	p daughter PIDp−PIDK	> 10
	p daughter p	$> 15\,\text{GeV}$
	p daughter p_{T}	$> 1\,\text{GeV}$
	p daughter χ^2_{IP} w.r.t. PV	> 25
	K^- daughter PIDK	> -5.0
	π^+ daughter PIDK	< 20.0
	χ^2_{vtx}/ndf	< 3
	DIRA w.r.t. PV	> 0.99
	Mass diff. to PDG	$< 80\,\text{MeV}$
	Transverse momentum	$> 2.1\,\text{GeV}$
	$\log_{10}$(IP) w.r.t. PV	> -1.5
	Flight distance χ^2 w.r.t. PV	> 25
$\Lambda_c^+ \mu^-$	Mass	$\in [2.2, 8.0]$ GeV
	χ^2_{vtx}/ndf	< 6
	DIRA w.r.t. PV	> 0.999

Chapter 6

Signal fit

This chapter describes the way, how the yield N_{D^0p} of the signal decays $\Lambda_b^0 \to D^0 p\mu^-\overline{\nu}_\mu X$ is determined. Due to the missing neutrino, the reconstructed Λ_b^0 mass does not peak at its actual mass and cannot be used to distinguish signal from background. Nonetheless the D^0p subsystem is of particular interest. Recently, BaBar measured the decay of two Λ_c^+ resonances into D^0p, namely $\Lambda_c(2880)^+ \to D^0p$ respectively $\Lambda_c(2940)^+ \to D^0p$ [20]. It is expected, that the $\Lambda_c(2880)^+$ and $\Lambda_c(2940)^+$ also appears in the invariant D^0p mass of the decay $\Lambda_b^0 \to D^0 p\mu^-\overline{\nu}_\mu X$ through the decay $\Lambda_b^0 \to \Lambda_c(2880/2940)^+\mu^-\overline{\nu}_\mu$ with $\Lambda_c(2880/2940)^+ \to D^0p$. Indeed, there are some peaking structures at $M(D^0p)$ around 2880 MeV and 2940 MeV as Figure 5.4 (top) shows. As a nice side effect, the masses and widths of those resonances can be determined, too. However, it is expected that most of the $\Lambda_b^0 \to D^0 p\mu^-\overline{\nu}_\mu X$ decays are nonresonant, i.e. they decay directly into the $D^0 p\mu^-\overline{\nu}_\mu X$ final state without going through an intermediate resonance. It should be stressed, that the measurement of $\mathcal{B}\left(\Lambda_b^0 \to D^0 p\mu^-\overline{\nu}_\mu X\right)$ is an inclusive measurement. This means, that every decay of a Λ_b^0 into a final state including a $D^0 p\mu^-\overline{\nu}_\mu$ is considered as signal. Thus, the nonresonant Λ_b^0 decays as well as the decays via the $\Lambda_c(2880)^+$ and $\Lambda_c(2940)^+$ resonances are counted to the signal yield N_{D^0p}.

Unfortunately, the nonresonant Λ_b^0 decays cannot be disentangled in the D^0p mass from combinatorial background like $B^0/B^+ \to D^0\mu^-\overline{\nu}_\mu X$ with randomly combined protons. As already mentioned in Chapter 9, an appropriate discriminating variable between signal and those combinatorial backgrounds is $\log\chi^2_{\mathrm{IP}}$. Just to remind, it has been defined as the logarithm of the difference between the χ^2_{vtx} of the $D^0\mu^-$ candidate with and without the proton, i.e. $\log\chi^2_{\mathrm{IP}} := \log\left[\chi^2_{\mathrm{vtx}}(D^0p\mu^-) - \chi^2_{\mathrm{vtx}}(D^0\mu^-)\right]$. The smaller $\log\chi^2_{\mathrm{IP}}$, the better the proton makes a vertex with the $D^0\mu^-$ candidate and the more likely it is a $\Lambda_b^0 \to D^0 p\mu^-\overline{\nu}_\mu X$ signal event. Figure 5.4 (bottom) illustrates the discriminating power of $\log\chi^2_{\mathrm{IP}}$ when one compares the data and the wrong sign distributions.

The strategy for the signal fit is to perform a two-dimensional binned likelihood fit to the D^0p mass to learn as much about intermediate resonant states as possible and to the $\log\chi^2_{\mathrm{IP}}$ distribution to disentangle $\Lambda_b^0 \to D^0 p\mu^-\overline{\nu}_\mu X$ signal from combinatorial background. Unfortunately, there is no theoretical description of the $\Lambda_b^0 \to D^0 p\mu^-\overline{\nu}_\mu X$ decay and the distributions of $M(D^0p)$ and $\log\chi^2_{\mathrm{IP}}$. Thus, the most important task is to find a proper parametrisation of the two-dimensional dis-

tribution on an empirical basis. Depending on the respective variables either data driven methods or simulations are used for that purpose as will be described in the following section.

6.1 Empiric determination of the two-dimensional $\log \chi^2_{\mathrm{IP}}/M(D^0p)$ distribution's shape

This section describes the determination of the shapes for the $\log \chi^2_{\mathrm{IP}}$ distribution and the D^0p mass shape. Though there will be a two-dimensional fit in the end, it is assumed that the $\log \chi^2_{\mathrm{IP}}$ and $M(D^0p)$ distributions can be determined separately for each fit component. The two-dimensional fit is rather needed for the separation of the different fit components, for instance the $M(D^0p)$ shapes are very similar for nonresonant signal and background but completely differ in their $\log \chi^2_{\mathrm{IP}}$ shape, i.e. their vertex quality.

For $\log \chi^2_{\mathrm{IP}}$, the functions to be fitted on data are determined with simulations. This determination is done for signal and background separately. Both shapes are then combined and fitted to data.

Concerning the invariant D^0p mass, there do not exist any reliable simulations predicting its shape. Here it is assumed that the behaviour of the combinatorial background component is similar to the wrong sign events. Hence, the $M(D^0p)$ distribution of the wrong sign events is used to get the shape of the background component. The signal component is determined with the data itself. To highly suppress combinatorial background leaking into the D^0p mass distribution, only events with a $\log \chi^2_{\mathrm{IP}} < 1$ are fitted. This corresponds to the distribution shown in Figure 5.4 (top).

6.1.1 $\log \chi^2_{\mathrm{IP}}$ shape

As already mentioned both, $\log \chi^2_{\mathrm{IP}}$ signal and background components, are determined with simulations. The $\log \chi^2_{\mathrm{IP}}$ distribution of the signal simulation in Figure 6.1 reminds of a Gaussian curve, but having different widths to the left and the right from the maximum. Thus, it is parametrised with a so called BIFURCATED GAUSSIAN. A bifurcated Gaussian is an asymmetric Gaussian with two different widths for the left and the right part from the maximum. If $\mathcal{G}(x|x_0,\sigma) = \frac{1}{\sqrt{2\pi}\sigma}\exp\left(-\frac{x-x_0}{2\sigma}\right)$ denotes a usual Gaussian with mean x_0 and width σ, a Bifurcated Gaussian can be written as[1]

$$\mathrm{BfG}(x|x_0,\sigma_{\mathrm{L}},\sigma_{\mathrm{R}}) \propto \begin{cases} \mathcal{G}(x|x_0,\sigma_{\mathrm{L}}) & \text{for } x < x_0 \\ \mathcal{G}(x|x_0,\sigma_{\mathrm{R}}) & \text{for } x > x_0 \end{cases}, \tag{6.1}$$

[1] All fitfunctions in the following are given without normalisation factors. That is why there always appears a $\propto$ sign instead of an equal sign.

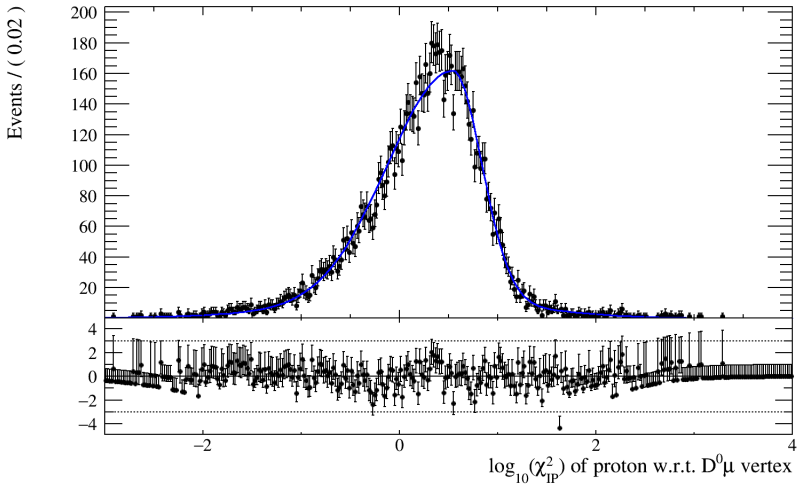

Figure 6.1: Fit to the $\log \chi^2_{\mathrm{IP}}$ distribution of the signal simulation. As parametrisation a double bifurcated Gaussian has been chosen.

The tails on both sides of $\log \chi^2_{\mathrm{IP}}$ are very broad compared to the peaking part. Thus a single bifurcated Gaussian is not sufficient. The final fit function for the signal $\log \chi^2_{\mathrm{IP}}$ shape is the sum of two bifurcated Gaussians, in the following called a double Bifurcated Gaussian DBfG

$$\begin{aligned}&\mathrm{DBfG}(x|x_0, \vec{\sigma_{\mathrm{L}}}, \vec{\sigma_{\mathrm{R}}}, f_{\mathrm{BfG_1}}) \propto \\ &f_{\mathrm{BfG_1}}\mathrm{BfG}(x|x_0, \sigma_{\mathrm{L_1}}, \sigma_{\mathrm{R_1}}) + (1 - f_{\mathrm{BfG_1}})\,\mathrm{BfG}(x|x_0, \sigma_{\mathrm{L_2}}, \sigma_{\mathrm{R_2}}),\end{aligned} \tag{6.2}$$

where $f_{\mathrm{BfG_1}}$ denotes the fraction of the first BfG and the two BfG share a common mean x_0. The fit result for the signal simulation can be seen in Figure 6.1. In order to estimate the quality of the fit, the PULL distribution is also shown in Figure 6.1 below the $\log \chi^2_{\mathrm{IP}}$ distribution. The pull of a variable x is defined as

$$\mathrm{pull}(x) = \frac{N_{\mathrm{meas}}(x) - N_{\mathrm{fit}}(x)}{\sigma_{N_{\mathrm{meas}}}(x)}. \tag{6.3}$$

Referring to Figure 6.1, $N_{\mathrm{meas}}(x)$ denotes the number of entries in the bin with $\log \chi^2_{\mathrm{IP}} = x$, $N_{\mathrm{fit}}(x)$ the corresponding result of the fit in the respective bin and $\sigma_{N_{\mathrm{meas}}}(x)$ the error on $N_{\mathrm{meas}}(x)$. In other words, the pulls are the residuals of the fit normalised to the uncertainty. If the fit describes the data well, the pull distribution should peak and fluctuate around zero with mean 1 [58]. From the pull distribution it can be stated that the chosen fit model describes the data well, especially in the tails. A little bias might be included if one closer looks at the region of $\log \chi^2_{\mathrm{IP}} \approx 0$.

Concerning the $\log \chi^2_{\mathrm{IP}}$ background shape, only a simulation with very little statistics is available. To get a better idea of the background $\log \chi^2_{\mathrm{IP}}$ shape and to increase statistics, right sign and wrong sign events of this sample have been added. In this case, wrong sign events refers to events with a $\Lambda_c^+\mu^+$ in the final state. Compared

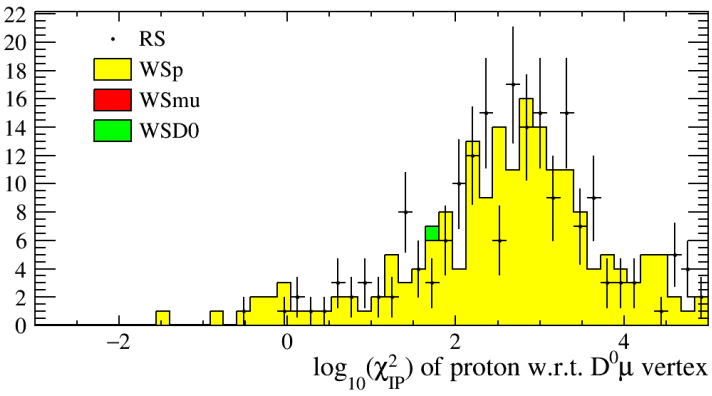

Figure 6.2: Comparison of the $\log \chi^2_{\mathrm{IP}}$ distribution for right sign and wrong sign events in the background simulation. Both, the shapes for right sign and wrong sign are very similar and thus can be added to increase statistics.

to the signal $\log \chi^2_{\mathrm{IP}}$ shape, both, right sign and wrong sign events, describe combinatorial background. Thus, it is assumed that their $\log \chi^2_{\mathrm{IP}}$ shapes are similar as Figure 6.2 confirms. According to this, the addition of right sign and wrong sign is appropriate to increase statistics in this case.

The $\log \chi^2_{\mathrm{IP}}$ distribution of the background simulation looks like a Gaussian around the maximum, but has a long tail to lower $\log \chi^2_{\mathrm{IP}}$ values. That is why a single CrystalBall function is chosen as fit function for the $\log \chi^2_{\mathrm{IP}}$ background shape. This function was first used by the CrystalBall collaboration to account for radiative losses in J/ψ or $\psi(2S)$ decays [59]. It is defined as

$$\mathrm{CB}(x|x_0,\sigma,\alpha,n) \propto \begin{cases} \exp\left(-\frac{(x-x_0)^2}{2\sigma^2}\right) & \text{for } \frac{x-x_0}{\sigma} > -\alpha \\ A \cdot \left(B - \frac{x-x_0}{\sigma}\right)^{-n} & \text{for } \frac{x-x_0}{\sigma} \leq -\alpha \end{cases}, \tag{6.4}$$

where

$$A = \left(\frac{n}{|\alpha|}\right)^n \exp\left(-\frac{|\alpha|^2}{2}\right), \tag{6.5}$$

$$B = \frac{n}{|\alpha|} - |\alpha|. \tag{6.6}$$

Hence, the CrystalBall function is a Gaussian with an enhanced tail at one side of the maximum, due to the power law for $\frac{x-x_0}{\sigma} \leq -\alpha$. So α denotes the transition between the Gaussian and the power law tail and n the latter's exponent.

The result of the fit to the background simulation can be seen in Figure 6.3. According to the pull distribution the fit nicely describes the data points. Nonetheless, one has to note, that statistics here are very little.

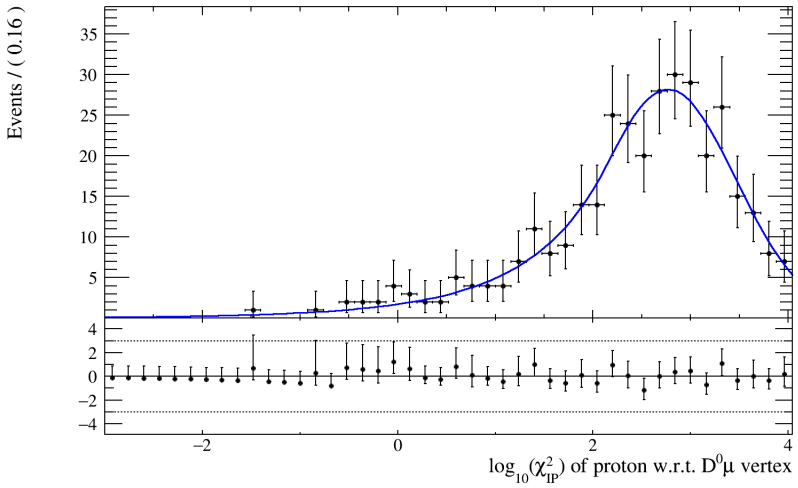

Figure 6.3: Fit to the (RS and WS added) $\log \chi^2_{\mathrm{IP}}$ shape of the background simulation. The distribution is modeled with a CrystalBall function.

6.1.2 One-dimensional fit to the $\log \chi^2_{\mathrm{IP}}$ distribution in data

To control if the chosen parametrization of the $\log \chi^2_{\mathrm{IP}}$ distribution gained from simulation describes data, a one-dimensional $\log \chi^2_{\mathrm{IP}}$-fit on data is performed. For that purpose, the double bifurcated Gaussian as signal component and the CrystalBall as background component are added, i.e. the total probability density function $\mathcal{P}$ for that fit is:

$$\begin{aligned}&\mathcal{P}(x|N_{\mathrm{sig}}, N_{\mathrm{bkg}}, x_{0,\mathrm{sig}}, x_{0,\mathrm{bkg}}\vec{\sigma_{\mathrm{L}}}_{,\mathrm{sig}}, \vec{\sigma_{\mathrm{R}}}_{,\mathrm{sig}}, f_{\mathrm{BfG}_1}, \sigma_{\mathrm{bkg}}, \alpha, n) \propto \\ &N_{\mathrm{sig}}\mathrm{DBfG}(x|x_{0,\mathrm{sig}}, \vec{\sigma_{\mathrm{L}}}_{,\mathrm{sig}}, \vec{\sigma_{\mathrm{R}}}_{,\mathrm{sig}}, f_{\mathrm{BfG}_1}) + N_{\mathrm{bkg}}\mathrm{CB}(x|x_{0,\mathrm{bkg}}, \sigma_{\mathrm{bkg}}, \alpha, n),\end{aligned} \tag{6.7}$$

where N_{sig} denotes the signal yield and N_{bkg} the background yield respectively. The fit result can be seen in Figure 6.4 and the corresponding yields and parameter values are listed in Table 6.1.

The chosen model very nicely describes the data as can be seen in the pull distribution. Thus the chosen parametrisation for the $\log \chi^2_{\mathrm{IP}}$ shape is reasonable. This fit is later also used for systematic studies, since it is already able to distinguish between signal and background yields, see Chapter 5 for further discussions.

6.1.3 D^0p mass shape

To get an idea of the (combinatorial) background shape in the D^0p mass distribution, events with a wrong sign proton, i.e. events with $D^0\overline{p}\mu^-$ in the final state are used since the transition from Λ_b^0 to a $D^0\overline{p}\mu^-$ final state is physically forbidden by charge conservation and should thus give a good proxy for randomly combined $\Lambda_b^0 \to D^0 p\mu^-\overline{\nu}_\mu$ candidates. The $M(D^0p)$ distribution of these wrong sign events is

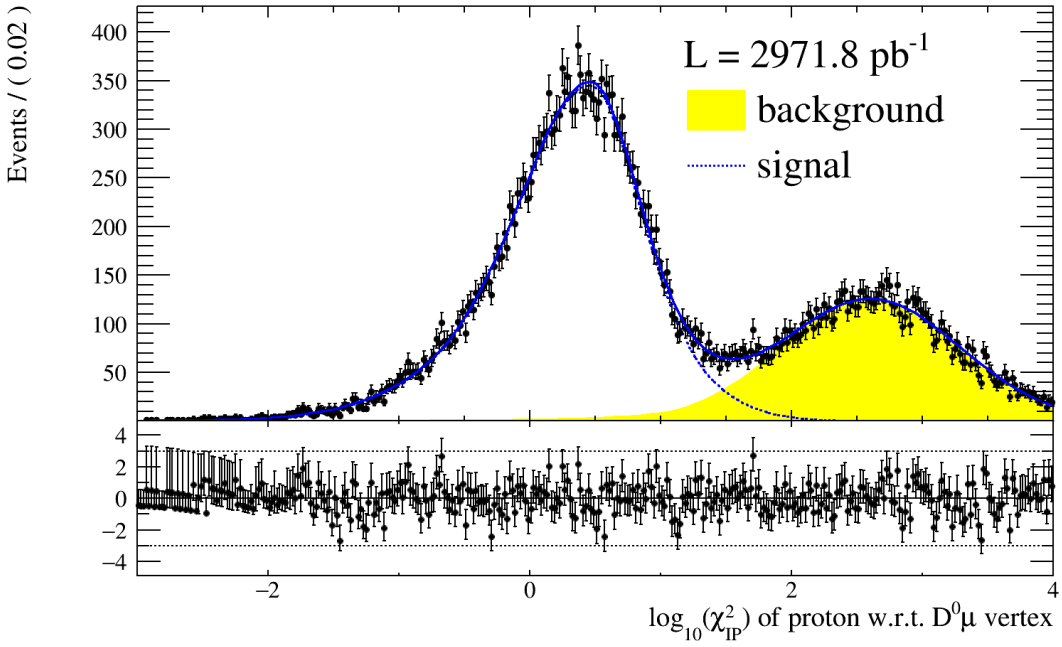

Figure 6.4: $\log \chi^2_{\mathrm{IP}}$ distribution of the data sample. A binned likelihood fit is performed on it with the sum of a double bifurcated Gaussian for the signal (blue, dashed line) and a CrystalBall function for the background component (yellow shaded).

shown in Figure 6.5 and modeled with an empirical background function [60]

$$\mathrm{EBG}(m|m_0, m_1, m_2, p, c_1) = \mathrm{PS}(m|m_1, m_2) \cdot (m - m_0)^p \cdot \exp\left[c_1 \left(1 - \frac{m_0}{m}\right)\right], \tag{6.8}$$

where $m_0 := m_1 + m_2$ denotes the kinematic D^0p mass threshold and PS the phase space function

$$\mathrm{PS}(m|m_1, m_2) = \frac{1}{2m}\sqrt{[m^2 - (m_1 + m_2)^2]\,[m^2 - (m_1 - m_2)^2]}. \tag{6.9}$$

The term with the power p is included as correction, in case the phase-space function does not satisfactorily describe the threshold shape. Here and in the following fits, m_1 and m_2 are fixed to the D^0 respectively proton PDG mass values. Figure 6.5 shows the result of the fit. Again, the model nicely describes the distribution. It should be noted here, that there is no structure observed in this wrong sign mass spectrum. This is a good confirmation, that the identification of the two peaks in the D^0p mass for right sign events as $\Lambda_c(2880)^+$ and $\Lambda_c(2940)^+$ is appropiate.

Unfortunately, there is no reliable simulation predicting the mass shape for the D^0p invariant mass. A shape for the signal therefore has to be determined empirically on data. A fit to the D^0p mass distribution is applied with the requirement

Table 6.1: Results of the onedimensional $\log \chi^2_{\mathrm{IP}}$ fit on data.

Variable	Value
Yields	
signal yield N_{sig}	$(2.325\pm0.028)\cdot 10^4$
background yield N_{bkg}	$(1.086\pm0.026)\cdot 10^4$
Signal (DBfG)	
mean $x_{0,\mathrm{sig}}$	$(4.59\pm0.26)\cdot 10^{-1}$
left width 1 $\sigma_{\mathrm{L,sig,1}}$	$(8.72\pm0.56)\cdot 10^{-1}$
right width 1 $\sigma_{2,\mathrm{sig,1}}$	$(5.74\pm0.44)\cdot 10^{-1}$
left width 2 $\sigma_{\mathrm{L,sig,2}}$	$(4.72\pm0.55)\cdot 10^{-1}$
right width 2 $\sigma_{\mathrm{R,sig,2}}$	$(3.37\pm0.23)\cdot 10^{-1}$
fraction BfG 1 $f_{\mathrm{BfG_1}}$	$(5.61\pm0.89)\cdot 10^{-1}$
Background (CB)	
CB mean $x_{0,\mathrm{bkg}}$	$(2.6\pm0.017)\cdot 10^0$
CB σ_{bkg}	$(6.85\pm0.14)\cdot 10^{-1}$
CB α	$(2.035\pm0.099)\cdot 10^0$
CB n	$(1.62\pm0.45)\cdot 10^0$

that the $D^0p\mu$ system makes a good vertex, i.e. $\log \chi^2_{\mathrm{IP}} < 1$. It is shown in Figure 6.6 top. This hard requirement strongly suppresses combinatorial background and allows to determine the signal distribution. As already stated before, the main part of the signal will be nonresonant. Besides that it is expected to see the two $\Lambda_c(2880)^+$ and $\Lambda_c(2940)^+$ resonances. They are parametrised by a relativistic Breit-Wigner distribution convoluted with a double Gaussian to account for the detector's mass resolution. The relativistic Breit-Wigner distribution is defined as follows:

$$\mathrm{RelBW}(m|m_R,m_1,m_2,\Gamma_0) \propto \frac{m\Gamma(m|m_R,m_1,m_2,\Gamma_0)}{(m^2-m_R^2)^2+(m_R\Gamma(m|m_R,m_1,m_2,\Gamma_0))^2}, \tag{6.10}$$

with

$$\Gamma(m|m_R,m_1,m_2,\Gamma_0) = \Gamma_0\frac{m_R}{m}\frac{S(m|m_1,m_2)}{S(m_R|m_1,m_2)}, \tag{6.11}$$

where PS denotes the phase space function of equation (6.9), m_R the resonance's mass and Γ_0 its width [61]. Thus, each resonance is modeled with

$$\begin{aligned}&\mathrm{RES}(m|m_R,m_1,m_2,\Gamma_0,\sigma_1,\sigma_2,f_1) \propto \\ &\mathrm{RelBW}(m|m_R,m_1,m_2,\Gamma_0)\otimes[f_1\mathcal{G}(m|0,\sigma_1)+(1-f_1)\mathcal{G}(m|0,\sigma_2)]\end{aligned} \tag{6.12}$$

The determination of the mass resolution is thoroughly described in section 6.2. The obtained resolution will be fixed in all fits later.

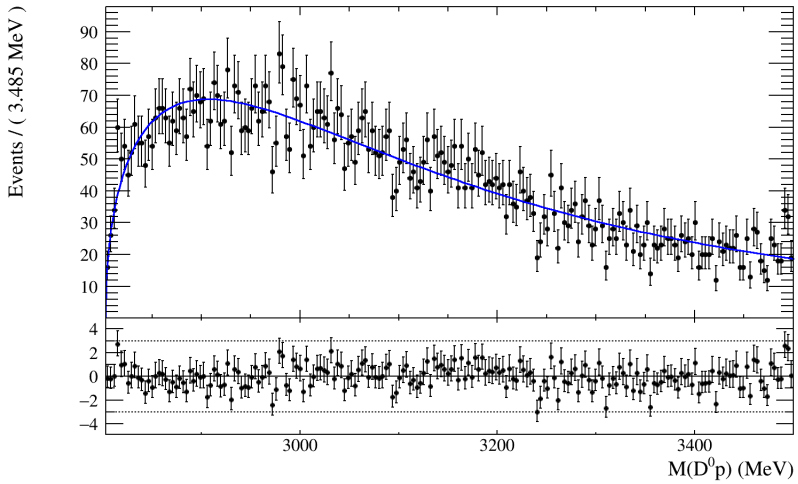

Figure 6.5: Fit to the D^0p mass of wrong sign proton events. As model an empiric background function has been chosen, see equation (6.8)

The non-resonant signal part is modeled with the sum of two exponential functions multiplied by a turn-on function.

$$\mathrm{TDExp}(m|m_0, c_0, c_1, c_2, f_{c_1}) \propto \left(1 - \mathrm{e}^{c_0(m-m_0)}\right) \cdot \left[f_{c_1}\mathrm{e}^{c_1 m} + (1 - f_{c_1})\mathrm{e}^{c_2 m}\right]. \tag{6.13}$$

The turn-on factor is needed to model the steep rise at the D^0p mass threshold.

The fit to the invariant D^0p mass distribution, that is shown on the upper side of Figure 6.6 does not describe the data at low D^0p mass. Different models for the non-resonant component have been tried to describe this steep curvature without success. However, when adding another resonant component, the fit converges and describes the data well as can be seen on the lower side of Figure 6.6. This additional component will be labeled “low mass enhancement" throughout the analysis. Thus, the total fit function consists of four parts: The non-resonant part modeled with the “turn-on double exponential" function TDExp of Equation (6.13) and relativistic Breit-Wigner functions according Equations (6.12) for the $\Lambda_c(2880)^+$, $\Lambda_c(2940)^+$ and the low mass enhancement. The fit results can be seen in Figure 6.6 (bottom) and Table 6.2.

Note, that at this point, the additional resonant component, the low mass enhancement, is merely introduced to enable the fit to converge and match the data. In principle, there are several possible reasons for such an enhancement, but there is some motivation to choose a resonant model as additional component: On the one hand the peak looks similar to the other resonances. On the other hand, there is a similar peak seen in other analyses e.g. BaBar is discussing a (much less pronounced) peak at an invariant D^0p mass of about 2840 MeV in its study on the D^0p final state in [20]. The reason for this peak is not understood so far and is currently studied in different ongoing LHCb analyses. Besides some detector effects,

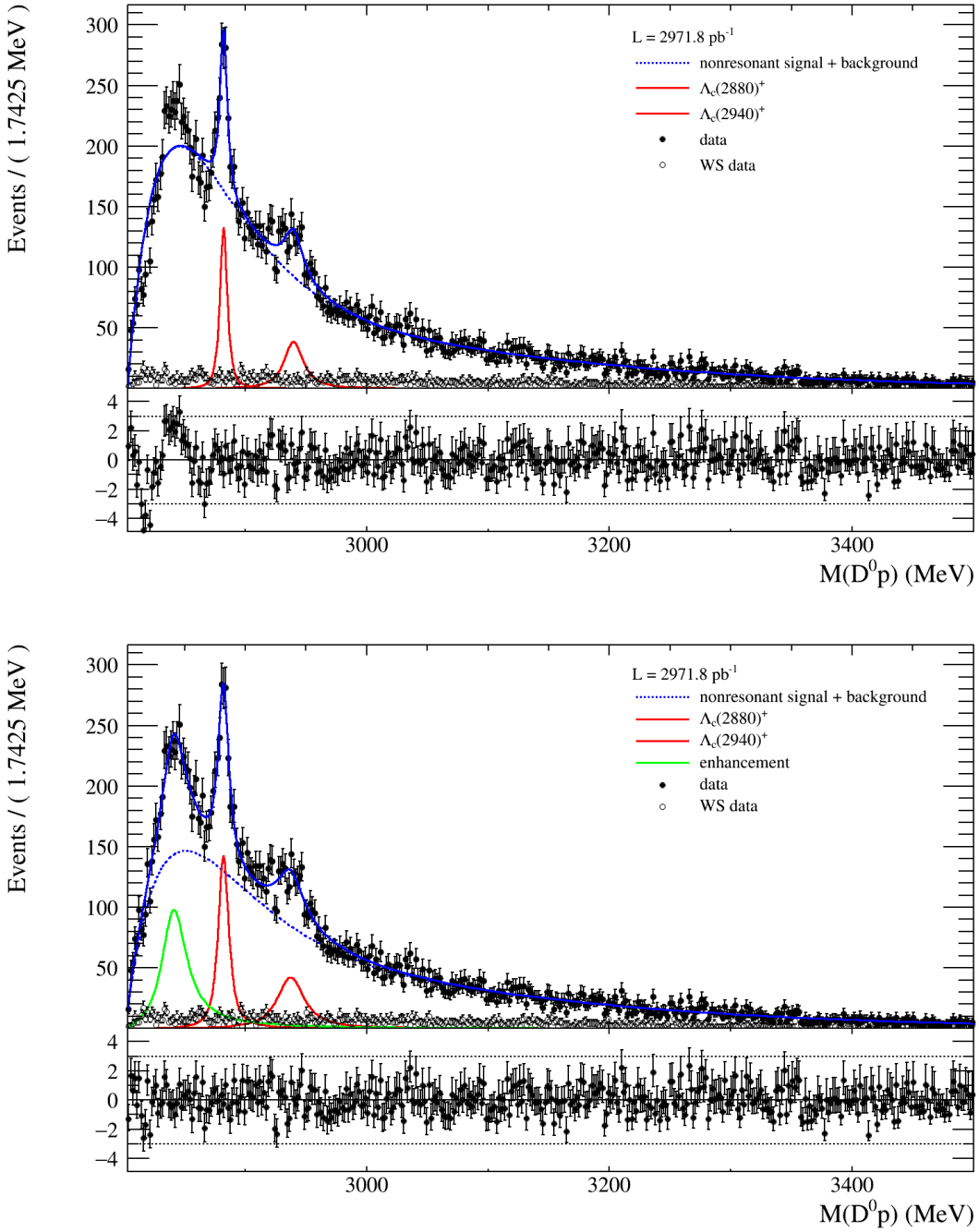

Figure 6.6: Invariant D^0p mass distribution when requiring $\log \chi^2_{\mathrm{IP}} < 1$. The upper figure shows a fit with two resonances (red lines) for the $\Lambda_c(2880)^+$ and $\Lambda_c(2940)^+$ and a nonresonant part (blue dashed line). Different attempts have been made to get a proper and converging fit, matching the data at low D^0p mass, without success. This issue can be solved by adding an additional resonant component (lower figure, green line), obeying the same fit model like the two resonances.

Table 6.2: Results of the D^0p mass fit.

Variable	Value
Yields	
$\Lambda_c(2880)^+$ signal yield $N_{\Lambda_c(2880)^+}$	$(1.2\pm0.14)\cdot10^3$
$\Lambda_c(2940)^+$ signal yield $N_{\Lambda_c(2940)^+}$	$(9.4\pm2.3)\cdot10^2$
mass enhancement yield N_{enh}	$(2.06\pm0.4)\cdot10^3$
nonresonant yield N_{nonres}	$(1.672\pm0.063)\cdot10^4$
$\Lambda_c(2880)^+$ **resonance**	
mean $m_{\Lambda_c(2880)^+}$ [MeV]	$(2.88197\pm0.00034)\cdot10^3$
width $\Gamma_{0,\Lambda_c(2880)^+}$ [MeV]	$(7.5\pm1.3)\cdot10^0$
$\Lambda_c(2940)^+$ **resonance**	
mean $m_{\Lambda_c(2940)^+}$ [MeV]	$(2.9375\pm0.0017)\cdot10^3$
width $\Gamma_{0,\Lambda_c(2940)^+}$ [MeV]	$(2.34\pm0.6)\cdot10^1$
Low mass enhancement	
mean m_{enh} [MeV]	$(2.84204\pm0.00087)\cdot10^3$
width $\Gamma_{0,\text{enh}}$ [MeV]	$(2.44\pm0.37)\cdot10^1$
nonresonant part	
turn on mass threshold m_0 [MeV]	$(2.80119\pm0.0005)\cdot10^3$
turn on slope c_0 [MeV^{-1}]	$(-4.0\pm7.4)\cdot10^{-4}$
exponential 1 slope c_1 [MeV^{-1}]	$(-2.3\pm0.11)\cdot10^{-2}$
exponential 2 slope c_2 [MeV^{-1}]	$(-6.84\pm0.39)\cdot10^{-3}$
fraction exponential 1 f_{c_1}	$(7.41\pm0.22)\cdot10^{-1}$

backgrounds or kinematical reflections it is not excluded, that a new particle is seen here. A thorough discussion, if this additional component is actually needed and what might cause this peak follows in Chapter 11. In the following, this component is treated as signal since it appears very clear when requiring $\log\chi^2_{\text{IP}} < 1$, i.e. in the background suppressed region making a good decay vertex.

6.2 Determination of the mass resolution

Due to resolution effects, the width of a resonance in a mass spectrum can appear wider than its natural width. In this analysis, the effect is accounted for by convoluting the Breit-Wigner, which is assumed to be the natural shape of the resonance, with a double Gaussian, describing the smearing of the resonance due to finite mass resolution, see Equation (6.12).

The determination of the mass resolution is performed in a simulation by comparing the generated (also called “true") mass with the reconstructed mass. The mean of the mass difference distribution is expected to be zero and the width refers to the mass resolution. The distribution is described by a double Gaussian function $f_1\mathcal{G}(m|m_0,\sigma_1) + (1-f_1)\mathcal{G}(m|m_0,\sigma_2)$ to properly describe the broadening of the mass difference distribution in the tails. To account for a potential mass de-

Table 6.3: Results of the fits to the mass difference distributions for the determination of the mass resolution. Only the values, which are required for the further analysis are quoted here.

Resonant component	σ_1[MeV]	σ_2[MeV]	f_1[MeV]
$\Lambda_c(2880)^+$	1.576±0.065	3.9±1.9	0.814±0.073
$\Lambda_c(2940)^+$	1.966±0.045	5.8±1.5	0.789±0.029
enhancement	0.830±0.041	1.75±0.16	0.524±0.072

pendence, this fit is performed in several bins of the true invariant D^0p mass. The left-hand side of Figure 6.7 exemplarily shows the mass difference between reconstructed and generated mass together with the fit of a double Gaussian in the bin $2910 < M(D^0p) < 2980\,\text{MeV}$. This bin corresponds to the $\Lambda_c(2940)^+$ resonance. The fits of all bins can be seen in Appendix A, Figure A.1. The widths σ_1 and σ_2 and the fraction of the first Gaussian f_1 obtained by these fits in the respective bins are used for the parametrisation of the resonances in the nominal D^0p mass fit as described by Equation (6.12). Table 6.3 summarises the obtained values, which are used for the further analysis. Though there is a mass dependence of the resolution over the whole D^0p mass spectrum it is assumed, that the mass resolution can be considered as constant over the natural width of the resonances. The right-hand side of Figure 6.7 shows the root-mean-square of the mass difference distributions in the different bins. This serves as a measure for the mass resolution and how it evolves since it is hard to assign a single value for the mass resolution due to the fit of a double Gaussian. At D^0p mass threshold, the D^0 and the proton are at rest. Thus, the measured D^0p mass is just the sum of the PDG masses of the D^0 and the proton. Hence, there is no sensitivity to a mass resolution at threshold. If the measured D^0p mass is above the threshold, there are contributions from the momenta of the D^0 and the proton to the measured D^0p mass, too, influencing the mass resolution. As the uncertainties of the momenta gets larger for increasing momenta, the mass resolution increases as well. The PDG values for the the natural widths of the two resonances are $\Gamma_{\Lambda_c(2880)^+,\text{PDG}} = (5.8 \pm 1.1)\,\text{MeV}$ and $\Gamma_{\Lambda_c(2940)^+,\text{PDG}} = (17^{+8}_{-6})\,\text{MeV}$. Thus, the resolution and natural width are of same order for the $\Lambda_c(2880)^+$. Concerning the $\Lambda_c(2940)^+$ resonance, the natural width dominates.

6.3 Nominal fit in two dimensions

With a two-dimensional fit to the D^0p mass and the $\log\chi^2_{\text{IP}}$ distribution, it is possible to distinguish between nonresonant signal and background in the D^0p mass spectrum as already explained. Thus, the different pieces of the previous sections are put together for a fit of both distributions.

It is assumed that the $\log\chi^2_{\text{IP}}$ distribution is the same for all 4 different signal components (non-resonant signal, $\Lambda_c(2880)^+$, $\Lambda_c(2940)^+$, enhancement), since their de-

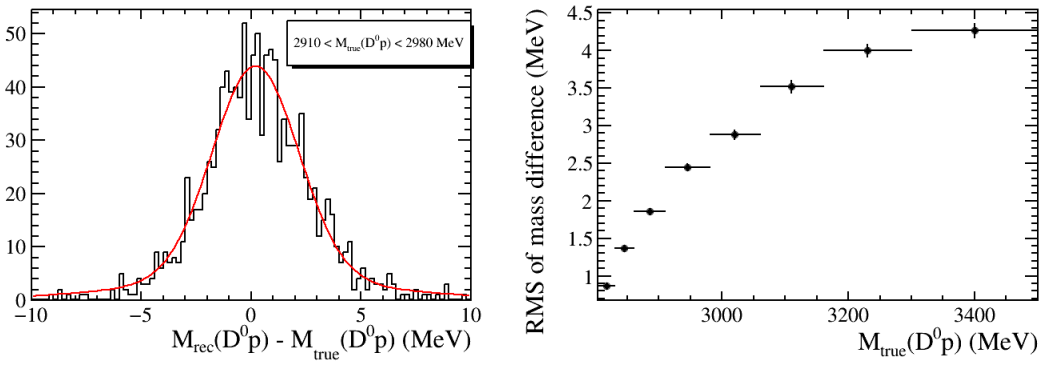

Figure 6.7: Left: Fit of a Gaussian to the difference between generated and reconstructed D^0p mass of the simulation sample in the range $2910 < M(D^0p) < 2980\,\mathrm{MeV}$, corresponding to the bin of the $\Lambda_c(2940)^+$ resonance. Right: root-mean-square (RMS) of the mass difference distributions for each bin. The RMS serves as a measure for the mass resolution since it is not easy to assign a single value for the mass resolution, since the distribution is modeled with a double Gaussian.

cay topologies are the same[2]. Hence, their $\log\chi^2_{\mathrm{IP}}$ distributions share all parameters. For the $\log\chi^2_{\mathrm{IP}}$ signal part a double Bifurcated Gaussian DBfG is chosen, whereas the background is modeled by a CrystalBall function CB. The D^0p mass signal components are modeled with the same parametrisation as described in Section 6.1.3. The empiric background function EBG is used to describe the background. Thus, the total parametrisation $\mathcal{P}_{\mathrm{2D}}$ of the two-dimensional $\log\chi^2_{\mathrm{IP}}/M(D^0p)$ distribution is

$$
\begin{aligned}
&\mathcal{P}_{\mathrm{2D}}(x,m|\vec{\lambda}) \propto \\
&\mathrm{DBfG}(x|x_{0,\mathrm{sig}},\vec{\sigma}_{\mathrm{L,sig}},\vec{\sigma}_{\mathrm{R,sig}},f_{\mathrm{BfG_1}}) \\
&\quad\cdot[\;\; N_{\mathrm{nonres}}\cdot\mathrm{TDExp}(m|m_0,c_0,c_1,c_2,f_{c_1}) \\
&\qquad + N_{\Lambda_c(2880)^+}\cdot\mathrm{RES}(m|m_{\Lambda_c(2880)^+},m_1,m_2,\Gamma_{0,\Lambda_c(2880)^+},\vec{\sigma}_{\Lambda_c(2880)^+},f_{1,\Lambda_c(2880)^+}) \\
&\qquad + N_{\Lambda_c(2940)^+}\cdot\mathrm{RES}(m|m_{\Lambda_c(2940)^+},m_1,m_2,\Gamma_{0,\Lambda_c(2940)^+},\vec{\sigma}_{\Lambda_c(2940)^+},f_{1,\Lambda_c(2940)^+}) \\
&\qquad + N_{\mathrm{enh}}\cdot\mathrm{RES}(m|m_{\mathrm{enh}},m_1,m_2,\Gamma_{0,\mathrm{enh}},\vec{\sigma}_{\mathrm{enh}},f_{1,\mathrm{enh}})\;] \\
&\quad + \mathrm{CB}(x|x_{0,\mathrm{bkg}},\sigma_{\mathrm{bkg}},\alpha,n)\cdot N_{\mathrm{bkg}}\cdot\mathrm{EBG}(m|m_0,m_1,m_2,p,c_{1,\mathrm{bkg}}),
\end{aligned}
\tag{6.14}
$$

where x denotes $\log\chi^2_{\mathrm{IP}}$, m the invariant D^0p mass, $\vec{\lambda}$ the set of all fit parameters and N_i the yields of the respective components. All other parameters are explained in the sections before, where the different functions have been introduced. All parameters are floating except for the mass resolution parameters of the resonant components in RES(...) and the D^0 and proton mass (m_1 respectively m_2), that are required in the phase space function PS, which again is part of the relativistic Breit-Wigner and the empiric background function. The results of the fit are shown in Table 6.4

[2]Presumed, that the enhancement indeed emerges to be a resonance or another signal component.

and the projections can be seen in Figure 6.8. The model very nicely describes the data. The pull distributions do not show any abnormalities. A discussion of the result follows in Section 6.5.

6.4 Fit to the wrong sign proton data as cross-check

As a cross-check, the two-dimensionsal fit is performed for the wrong sign data with the same parametrisation as for the right sign data in Section 6.3. However, due to the absence of resonances, it is purely described by the nonresonant functions, i.e. the nonresonant signal component and the background component. The respective plots can be seen in Figure 6.9. No structure in the mass distribution is seen, especially the $\Lambda_c(2880)^+$ and $\Lambda_c(2940)^+$ resonances vanish in the wrong sign D^0p. Interesting is to note, that besides the two resonances even the enhancement vanishes. Thus, it cannot be explained by random combinations of the particles. Concerning the $\log\chi^2_{\mathrm{IP}}$ distribution, there is nevertheless a "signal-like" part. This is presumably background from $B^0/B^+ \to D^0\mu^-\overline{\nu}_\mu X$ decays, where the X is of "wrong charge" and moreover misidentified as (anti)proton. Since the physics are different for right sign and wrong sign events, the yield obtained in this WS fit cannot easily be subtracted from the nominal fit to account for fake proton backgrounds. A more thorough study on fake backgrounds will be performed in Chapter 9.

6.5 Extraction of $\Lambda_b^0 \to D^0p\mu^-\overline{\nu}_\mu X$ signal yield and $\Lambda_c(2880)^+$/ $\Lambda_c(2940)^+$ properties

From the previous fits, different results can be obtained. The most important result is the $\Lambda_b^0 \to D^0p\mu^-\overline{\nu}_\mu X$ signal yield N_{D^0p} for the determination of $\mathcal{R}$. This result is obtained by the nominal two-dimensional fit. The obtained yields for the nonresonant component, the $\Lambda_c(2880)^+$ and the $\Lambda_c(2940)^+$ as well as the enhancement, which can be found in Table 6.4, are summed up. Thus, the total $\Lambda_b^0 \to D^0p\mu^-\overline{\nu}_\mu X$ signal yield is

$$\begin{aligned} N_{D^0p} &= N_{\mathrm{nonres}} + N_{\Lambda_c(2880)^+} + N_{\Lambda_c(2940)^+} + N_{\mathrm{enh}} \\ &= (2.293 \pm 0.088) \cdot 10^4. \end{aligned}$$

Remember, that the aim of this thesis is to measure the inclusive branching ratio of $\Lambda_b^0 \to D^0p\mu^-\overline{\nu}_\mu X$. That is why all components ending up in a final state containing a D^0 meson, a proton and a muon are summed up for the total signal yield. Again, it has to be confirmed in chapter 11, that it is appropriate to consider the enhancement as signal.

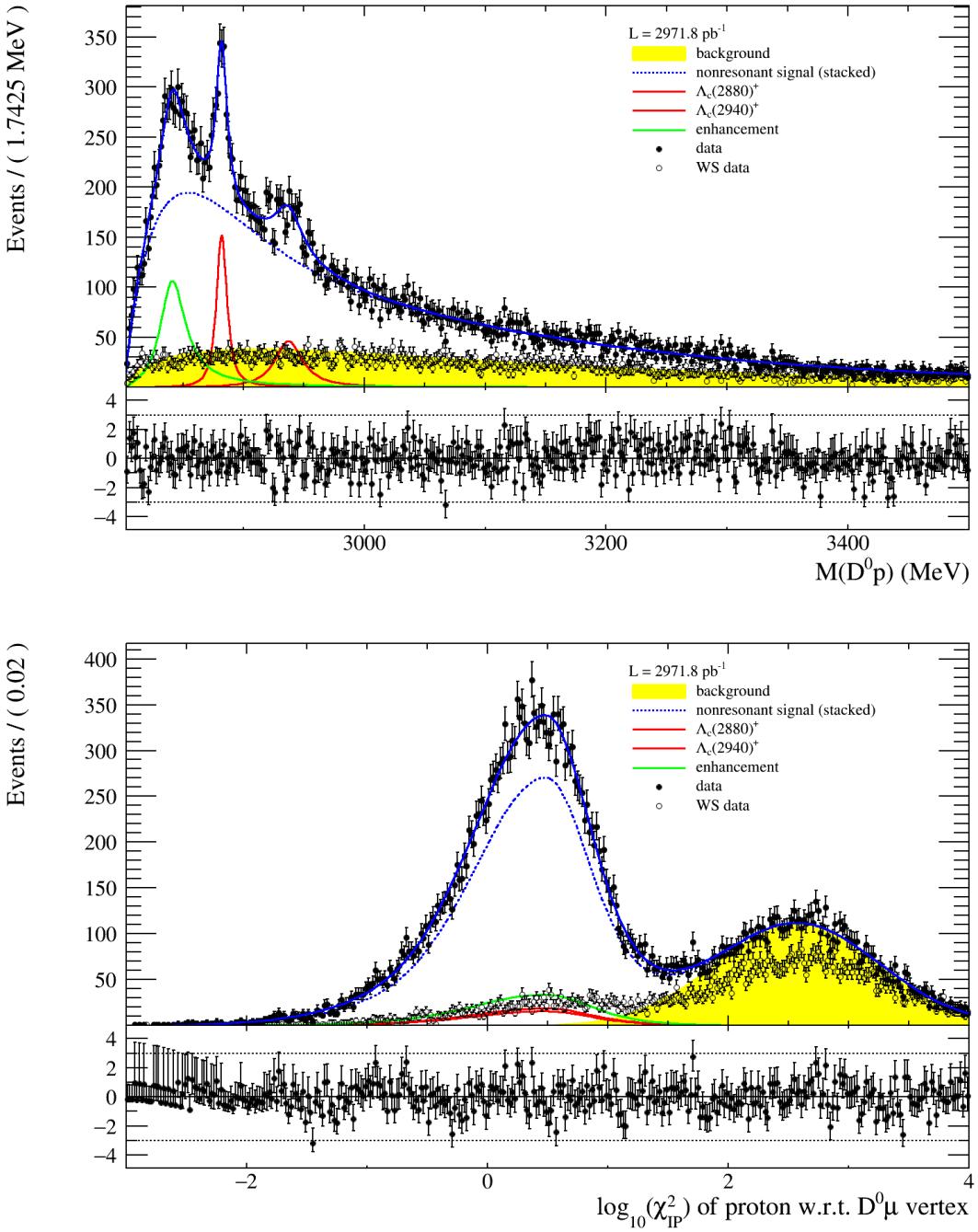

Figure 6.8: Two-dimensional fit to the $\Lambda_b^0 \to D^0 p \mu^- \overline{\nu}_\mu X$ candidates. Top: projection of invariant $D^0 p$ mass. Bottom: projection of $\log \chi^2_{\mathrm{IP}}$ distribution projection. The fit model is described in the text. The yellow shaded area shows the background component, stacked on top the nonresonant signal component marked as blue, dashed line. The two identified $\Lambda_c(2880)^+$ and $\Lambda_c(2940)^+$ resonances are drawn with a red solid line, the additional enhancement in green. For comparison the open circles show the wrong sign events.

Table 6.4: Results of the twodimensional M($D^0 p$) and $\log \chi^2_{\mathrm{IP}}$ fit.

Variable	Value
Yields	
$\Lambda_c(2880)^+$ signal yield $N_{\Lambda_c(2880)^+}$	$(1.28 \pm 0.15) \cdot 10^3$
$\Lambda_c(2940)^+$ signal yield $N_{\Lambda_c(2940)^+}$	$(1.06 \pm 0.24) \cdot 10^3$
mass enhancement yield N_{enh}	$(2.29 \pm 0.45) \cdot 10^3$
nonresonant signal yield N_{nonres}	$(1.83 \pm 0.069) \cdot 10^4$
background yield N_{bkg}	$(9.42 \pm 0.14) \cdot 10^3$
$\Lambda_c(2880)^+$ **resonance**	
mean $m_{\Lambda_c(2880)^+}$ [MeV]	$(2.88197 \pm 0.00034) \cdot 10^3$
width $\Gamma_{0,\Lambda_c(2880)^+}$ [MeV]	$(7.4 \pm 1.3) \cdot 10^0$
$\Lambda_c(2940)^+$ **resonance**	
mean $m_{\Lambda_c(2940)^+}$ [MeV]	$(2.9374 \pm 0.0016) \cdot 10^3$
width $\Gamma_{0,\Lambda_c(2940)^+}$ [MeV]	$(2.44 \pm 0.55) \cdot 10^1$
Low mass enhancement	
mean m_{enh} [MeV]	$(2.84222 \pm 0.00088) \cdot 10^3$
width $\Gamma_{0,\mathrm{enh}}$ [MeV]	$(2.51 \pm 0.37) \cdot 10^1$
Nonresonant signal	
turn on mass threshold m_0 [MeV]	$(2.80127 \pm 0.00057) \cdot 10^3$
turn on slope c_0 [MeV^{-1}]	$(-2.0 \pm 36.0) \cdot 10^{-4}$
exponential 1 slope c_1 [MeV^{-1}]	$(-2.34 \pm 0.14) \cdot 10^{-2}$
exponential 2 slope c_2 [MeV^{-1}]	$(-7.03 \pm 0.78) \cdot 10^{-3}$
fraction exponential 1 f_{c_1}	$(7.36 \pm 0.25) \cdot 10^{-1}$
Background (mass)	
Empiric BG $c_{1,\mathrm{bkg}}$ [MeV^{-1}]	$(-1.595 \pm 0.05) \cdot 10^1$
Empiric BG p	$(5.6 \pm 3.0) \cdot 10^{-2}$
Signal ($\log \chi^2_{\mathrm{IP}}$)	
mean $x_{0,\mathrm{sig}}$	$(4.8 \pm 0.16) \cdot 10^{-1}$
left width 1 $\sigma_{\mathrm{L,sig},1}$	$(9.76 \pm 0.27) \cdot 10^{-1}$
right width 1 $\sigma_{\mathrm{R,sig},1}$	$(6.22 \pm 0.32) \cdot 10^{-1}$
left width 2 $\sigma_{\mathrm{L,sig},2}$	$(5.37 \pm 0.24) \cdot 10^{-1}$
right width 2 $\sigma_{\mathrm{R,sig},2}$	$(3.41 \pm 0.15) \cdot 10^{-1}$
fraction BfG 1 f_{BfG_1}	$(4.21 \pm 0.42) \cdot 10^{-1}$
Background ($\log \chi^2_{\mathrm{IP}}$)	
CB mean $x_{0,\mathrm{bkg}}$	$(2.573 \pm 0.012) \cdot 10^0$
CB σ_{bkg}	$(6.87 \pm 0.11) \cdot 10^{-1}$
CB α	$(7.1 \pm 3.8) \cdot 10^0$
CB n	$(3.0 \pm 1.4) \cdot 10^0$

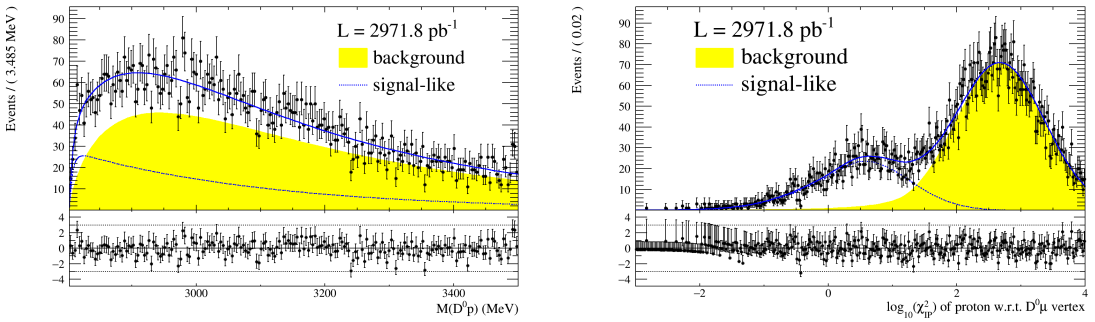

Figure 6.9: Invariant D^0p mass (left) and $\log \chi^2_{\mathrm{IP}}$ (right) distribution for "wrong sign" (WS) events. The signal-like component (blue, dashed line) of the fit can be assigned to $B^0/B^+ \to D^0\mu^-\overline{\nu}_\mu X$ decays, where the X is a fake proton of "wrong" charge.

As a side effect, the properties of the $\Lambda_c(2880)^+$ and $\Lambda_c(2940)^+$ resonances are extracted from the fit of the invariant D^0p mass. In this case it is not needed to distinguish between nonresonant signal and background, since only the peaks are of interest. To avoid uncertainties caused by this distinction, the properties of the two resonances are taken from the one-dimensional fit to the invariant D^0p mass (see Table 6.2):

$$\begin{aligned}
\Lambda_c(2880)^+ : \qquad & m_{\Lambda_c(2880)^+} = (2881.97 \pm 0.34)\,\mathrm{MeV}, \\
& \Gamma_{\Lambda_c(2880)^+} = (7.5 \pm 1.3)\,\mathrm{MeV}, \\
\Lambda_c(2940)^+ : \qquad & m_{\Lambda_c(2940)^+} = (2937.5 \pm 1.7)\,\mathrm{MeV}, \\
& \Gamma_{\Lambda_c(2940)^+} = (23.4 \pm 6.0)\,\mathrm{MeV}.
\end{aligned}$$

The PDG values for the properties of the two resonances are $m_{\Lambda_c(2880)^+,\mathrm{PDG}} = (2881.53 \pm 0.35)\,\mathrm{MeV}$ and $\Gamma_{\Lambda_c(2880)^+,\mathrm{PDG}} = (5.8 \pm 1.1)\,\mathrm{MeV}$ for the $\Lambda_c(2880)^+$ as well as $m_{\Lambda_c(2940)^+,\mathrm{PDG}} = (2939.3^{+1.4}_{-1.5})\,\mathrm{MeV}$ and $\Gamma_{\Lambda_c(2940)^+,\mathrm{PDG}} = (17^{+8}_{-6})\,\mathrm{MeV}$ for the $\Lambda_c(2940)^+$ respectively. These values are based on a BaBar measurement of the D^0p final state and a Belle measurement of $\Lambda_c(2880)^+/\Lambda_c(2940)^+$ decays into $\Sigma_c(2455)^{0,++}\pi^\pm$ [62]. The obtained results are in good agreement with the current world averages.

Though the reason for the low mass enhancement is not understood so far and it cannot be concluded, if a new particle is seen, the obtained mass and width are quoted here for the sake of completeness:

$$\begin{aligned}
\text{enhancement} : \qquad & m_{\mathrm{enh}} = (2842.04 \pm 0.87)\,\mathrm{MeV}, \\
& \Gamma_{\mathrm{enh}} = (24.4 \pm 3.7)\,\mathrm{MeV}.
\end{aligned}$$

Chapter 7

Fit to the reference channel $\Lambda_b^0 \to \Lambda_c^+ \mu^- \overline{\nu}_\mu$

This chapter describes the measurement of the signal yield $N_{\Lambda_c^+}$ in the normalisation channel $\Lambda_b^0 \to \Lambda_c^+ \mu^- \overline{\nu}_\mu$ ($\Lambda_c^+ \to pK^-\pi^+$). The method is different to the one in the signal channel $\Lambda_b^0 \to D^0 p\mu^- \overline{\nu}_\mu X$ due to several reasons: All of the final state particles of the subdecay $\Lambda_c^+ \to pK^-\pi^+$ can be reconstructed and the statistics is much higher. Going through an intermediate resonance, it is possible to see a clear Λ_c^+ mass peak as shown in Figure 7.1. In $\Lambda_b^0 \to D^0 p\mu^- \overline{\nu}_\mu X$ decays, the major part of the decays was non-resonant. The small sidebands indicate a small combinatorial background in the subdecay $\Lambda_c^+ \to pK^-\pi^+$. The background contribution coming from a random combination of a Λ_c^+ with a muon can be estimated by investigating the wrong sign final states combinations $\Lambda_c^+ \mu^+$. Since a Λ_b^0 cannot decay into a $\Lambda_c^+ \mu^+$ due to charge conservation, this unphysical combination serves as model for randomly combined $\Lambda_c^+ \mu^-$. The second reason why a different method is chosen compared to the $\Lambda_b^0 \to D^0 p\mu^- \overline{\nu}_\mu X$ channel, is the fact that the Λ_b^0 can decay into several excited Λ_c^+ states, in the following denoted as Λ_c^{*+} for any excited Λ_c^+ state. Contrary to $\Lambda_b^0 \to D^0 p\mu^- \overline{\nu}_\mu X$, the yield of the decay $\Lambda_b^0 \to \Lambda_c^+ \mu^- \overline{\nu}_\mu$ is measured exclusively. This means, that all decays going through intermediate resonances etc. have to be subtracted. It has been shown in [11], that the $\Lambda_b^0 \to \Lambda_c^+ \mu^- \overline{\nu}_\mu$ data is polluted by the decays $\Lambda_b^0 \to \Lambda_c(2595)^+ \mu^- \overline{\nu}_\mu$ and $\Lambda_b^0 \to \Lambda_c(2625)^+ \mu^- \overline{\nu}_\mu$. These excited Λ_c^{*+} baryons instantly decay for instance in $\Lambda_c^+ \pi^+ \pi^-$ or $\Lambda_c^+ \pi^0$. If these (neutral) pions are not reconstructed, those decays cannot be distinguished from $\Lambda_b^0 \to \Lambda_c^+ \mu^- \overline{\nu}_\mu$ by its topology. Thus, a fit of $\log \chi^2_{\mathrm{IP}}$, a measure for the vertex quality, as done in Chapter 6 would not help to distinguish between $\Lambda_b^0 \to \Lambda_c^+ \mu^- \overline{\nu}_\mu$ and $\Lambda_b^0 \to \Lambda_c^{*+} \mu^- \overline{\nu}_\mu$ and a different approach for the determination of $N_{\Lambda_c^+}$ has to be chosen.

The solution of the latter problem is to fit the corrected $pK^-\pi^+\mu^-$ alias Λ_b^0 mass. It has been stated in Chapter 5, that the corrected $pK^-\pi^+\mu^-$ or Λ_b^0 mass peaks close to the nominal Λ_b^0 mass, if the missing particle is massless. Concerning the $\Lambda_b^0 \to \Lambda_c^{*+} \mu^- \overline{\nu}_\mu$ decays, on misses not only the neutrino, but furthermore massive particles like the neutral pions. Thus, the corrected Λ_b^0 mass is shifted to lower masses, enabling a fit to distinguish between the semileptonic Λ_b^0 decay into a Λ_c^+ or Λ_c^{*+}. This assumption on the corrected mass is verified in Section 7.2.

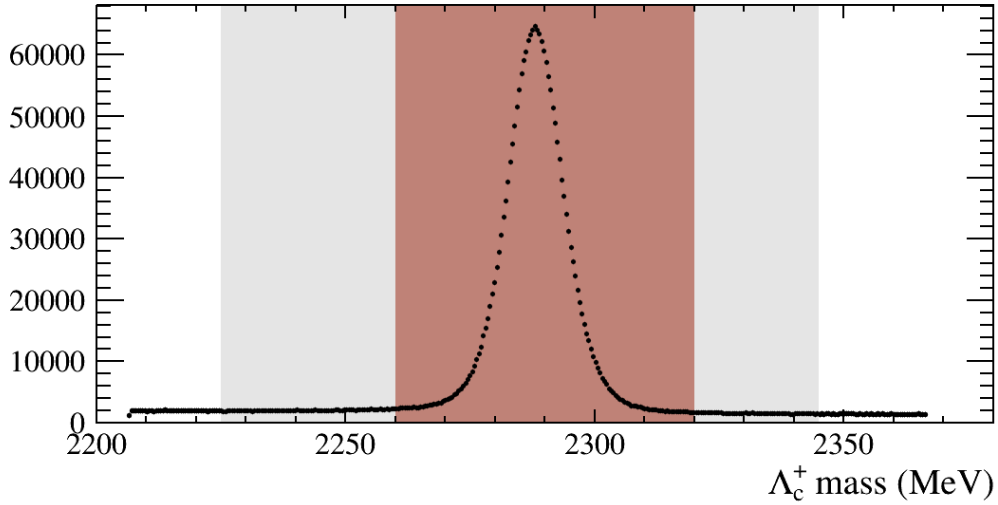

Figure 7.1: Plot of the invariant $pK^-\pi^+$ mass distribution. A clear mass peak identified as the Λ_c^+ can be seen. The dark shaded area indicates the chosen signal band and the light grey area the background bands for the sideband subtraction.

7.1 Reduction and handling of backgrounds

This section describes the ways, how different sources of backgrounds are either handled or reduced.

7.1.1 Non Λ_c^+ background

As already mentioned, the reconstruction of $pK^-\pi^+$ yields a nice mass peak forming the hadronically decaying Λ_c^+, which can be seen in Figure 7.1. Events outside of this peak can be explained by a random combination of a proton, a kaon and a pion. Nonetheless, there is also a certain amount of this “combinatorial" background in the peak region. It is statistically eliminated by a sideband subtraction. For this purpose, one assumes that the distribution of a kinematic variable of background under the peak region (also called signal band) is very similar to the distribution of the background in the (averaged) sidebands. Thus, the background distribution of a certain kinematic variable in the peak region is eliminated by subtracting the distribution of that variable in the sidebands. The signal band is chosen to lie in the invariant $pK^-\pi^+$ mass range of $M(pK^-\pi^+) \in [2260, 2320]$ MeV. The background bands are $M(pK^-\pi^+) \in [2225, 2260]$ MeV or $M(pK^-\pi^+) \in [2320, 2345]$ MeV. The chosen bands are visualised in Figure 7.1.

7.1.2 Random combinations of Λ_c^+ and μ^-

The next possible source of backgrounds are random combinations of a correctly reconstructed Λ_c^+ baryon and a muon μ^-. Due to the missing neutrino $\overline{\nu}_\mu$, there is no signal mass peak and it is not possible to use a sidebandsubtraction on the invariant $pK^-\pi^+\mu^-$ ($\Lambda_c^+\mu^-$) mass. Thus, wrong sign events, i.e. "unphysical" events with a $\Lambda_c^+\mu^+$ in the final state as explained above are used to estimate the amount of random $\Lambda_c^+\mu^-$ background. It is assumed that the shape and the number of the wrong sign events are compatible with the shape and number of random $\Lambda_c^+\mu^-$ combinations. Finally, the amount of wrong sign events is subtracted from the "right sign" events to statistically eliminate this source of backgrounds.

7.1.3 Peaking backgrounds

The third source of backgrounds is peaking background from partially reconstructed decays. This means, that there are physical decays mimicking to be signal, since some of the particles are not reconstructed. In this case, the $\Lambda_b^0 \to \Lambda_c^+\mu^-\overline{\nu}_\mu$ data is polluted by the decays $\Lambda_b^0 \to \Lambda_c^*(2595)^+\mu^-\overline{\nu}_\mu$ and $\Lambda_b^0 \to \Lambda_c^*(2625)^+\mu^-\overline{\nu}_\mu$ [11]. A Λ_c^{*+} subsequently decays into a Λ_c^+ and a not reconstructed neutral remnant, e.g. π^0, $\pi^+\pi^-$. Since this decay happens instantaneously, it looks the same as $\Lambda_c^+ \to pK^-\pi^+$ in the detector. As already explained, those decays can be distinguished from $\Lambda_b^0 \to \Lambda_c^+\mu^-\overline{\nu}_\mu$ by their corrected Λ_b^0 mass. Thus, these kind of backgrounds are not subtracted from the data, but rather included as component into the fit to the corrected Λ_b^0 mass.

7.2 Fit to the corrected $pK^-\pi^+\mu^-$ (Λ_b^0) mass

In this chapter it is verified in a simulation, that the corrected $pK^-\pi^+\mu^-$ mass is different for $\Lambda_b^0 \to \Lambda_c^+\mu^-\overline{\nu}_\mu$, $\Lambda_b^0 \to \Lambda_c^*(2595)^+\mu^-\overline{\nu}_\mu$ and $\Lambda_b^0 \to \Lambda_c^*(2625)^+\mu^-\overline{\nu}_\mu$. Figure 7.2 shows the simulated corrected $pK^-\pi^+\mu^-$ mass distributions for the different decays.
With the help of Figure 7.2, one can draw the following conclusions:

- The corrected $pK^-\pi^+\mu^-$ mass indeed looks different for $\Lambda_b^0 \to \Lambda_c^+\mu^-\overline{\nu}_\mu$ and $\Lambda_b^0 \to \Lambda_c^{*+}\mu^-\overline{\nu}_\mu$ decays. It peaks close to the nominal Λ_b^0 mass for $\Lambda_b^0 \to \Lambda_c^+\mu^-\overline{\nu}_\mu$, whereas it is shifted to lower masses for the decays into the excited Λ_c^{*+} states.

- It is not possible to distinguish in the Λ_b^0 corrected mass spectrum between the semileptonic Λ_b^0 decays into $\Lambda_c^*(2595)^+$ and $\Lambda_c^*(2625)^+$ as their shapes are too similar.

The latter conclusion is not really a problem since the only result of interest is the $\Lambda_b^0 \to \Lambda_c^+\mu^-\overline{\nu}_\mu$ signal yield. A distinction among the excited states is not needed. In

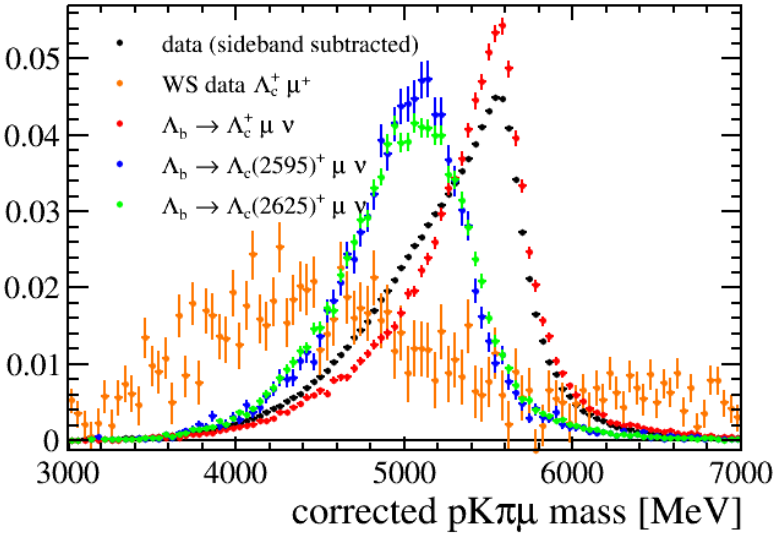

Figure 7.2: Comparison of the $pK^-\pi^+\mu^-$ corrected mass for the semileptonic Λ_b^0 decays via Λ_c^+, $\Lambda_c^*(2595)^+$ and $\Lambda_c^*(2625)^+$ gained from simulation. The black points show the sideband subtracted data distribution. The shape of the combinatorial $\Lambda_c^+\mu^-$ background (WS events), which is subtracted for the fit, is shown in orange.

the fit, there will be just one common component for both final states. Having this in mind, the fit procedure is performed as follows:

1. The data is sideband-subtracted using the $pK^-\pi^+$ (i.e. Λ_c^+) mass bands.
2. The corrected $pK^-\pi^+\mu^-$ mass distribution from wrong sing events is subtracted from the respective distribution from the right sign data.
3. A fit of the $pK^-\pi^+\mu^-$ mass is performed using the Beeston-Barlow method (see Section 2.3.2) to account for uncertainties in the corrected mass templates from simulation. The fitted parameters are the Λ_c^+ signal yield and one common yield for the two excited Λ_c^{*+} channels.

The results can be seen in Figure 7.3 and Table 7.1. They are presented in different ways: The left-hand side shows the fit result with the adjusted templates according to the Beeston-Barlow method, i.e. the templates have been modified binwise within their uncertainties to better match the data. The agreement with the data is remarkable, even on a logarithmic scale, shown in the bottom row of Figure 7.3. The right-hand side compares data and fit result with the bare templates. Slight deviations can be figured out here, above all in the tails with few statistics. The $\Lambda_b^0 \to \Lambda_c^+ \mu^- \overline{\nu}_\mu$ signal yield $N_{\Lambda_c^+}$, obtained by the fit to the corrected $pK^-\pi^+\mu^-$ mass and required for the determination of $\mathcal{R}$, is:

$$N_{\Lambda_c^+} = (1.544 \pm 0.011) \cdot 10^6$$

Table 7.1: Results of the Λ_c^+ corrected mass fit.

Variable	Value
Λ_c^+ candidates $N_{\Lambda_c^+}$	$(1.544 \pm 0.011) \cdot 10^6$
excited Λ_c^{*+} candidates	$(4.375 \pm 0.096) \cdot 10^5$
combinatoric background	$(1.196 \pm 0.033) \cdot 10^4$

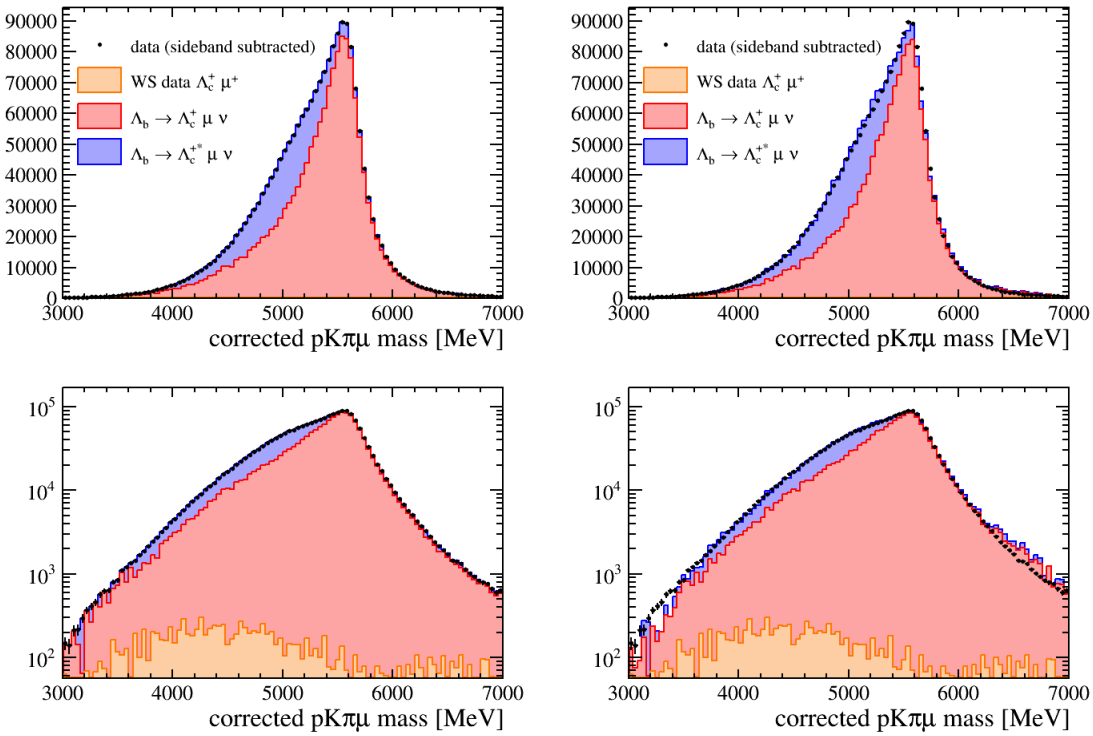

Figure 7.3: Fit to the $pK^-\pi^+\mu^-$ corrected mass for the determination of the $\Lambda_b^0 \to \Lambda_c^+\mu^-\overline{\nu}_\mu$ signal yield. The left plot shows the fit result with the adjusted templates according to the Beeston-Barlow method, the right one the bare templates without any modification. The top row shows the result on a linear, the bottom row on logarithmic scale.

Chapter 8

Efficiencies

The detection and reconstruction of particle decays is not perfect at all, i.e. not all particles and tracks originating from the pp interaction are detected and recorded. The ratio of the detected and selected signal yields and the total number of decays, which took place, is referred to as “efficiencies". There are several reasons for inefficiencies. Here are some examples:

- Particles escape the geometrical detector acceptance.
- There are dead regions in the detector.
- Applying selection requirements for the reduction of backgrounds prevents signal events to pass these requirements as well.

For the measurement of the number of signal events, the exact knowledge / determination of all efficiencies is crucial. The way, how the efficiencies for the $\Lambda_b^0 \to D^0 p\mu^-\overline{\nu}_\mu X$ and $\Lambda_b^0 \to \Lambda_c^+\mu^-\overline{\nu}_\mu$ decays are accounted for the measurement of the relative branching ratio $\mathcal{R}$, is shown in Equation (4.2).

For this analysis, the efficiencies are determined using simulated events. These simulation samples contain information about all generated as well as reconstructed events for which detector effects are accounted for. The simple way is to divide the number of reconstructed and selected simulated events by the number of generated events. This efficiency is hereafter called selection efficiency ϵ_{sel}. However, some generated events are rejected before they enter the simulation process, since above all the simulation of the detector takes a lot of time. Thus, several requirements are already applied during generation to reduce the computation time of the simulation production, for instance all generated events are required to be in the LHCb acceptance. A further acceleration of the production process can be achieved with additional requirements on the final state particles' (transverse) momenta. Concerning the $\Lambda_b^0 \to D^0 p\mu^-\overline{\nu}_\mu X$ and $\Lambda_b^0 \to \Lambda_c^+\mu^-\overline{\nu}_\mu$ channel, these requirements are different and likewise the efficiencies of the generation process. Thus, the so-called generator level efficiency ϵ_{gen} also has to be determined for both channels. The total efficiency used for the calculation of $\mathcal{R}$ is the product $\epsilon_{\text{gen}} \cdot \epsilon_{\text{sel}}$.

Unfortunately, it is known that the simulations do not perfectly describe the data. Since the decay $\Lambda_b^0 \to D^0 p\mu^-\overline{\nu}_\mu X$ is not well-known, the physical properties are not correctly modeled in simulation and thus disagree with data. Additionally,

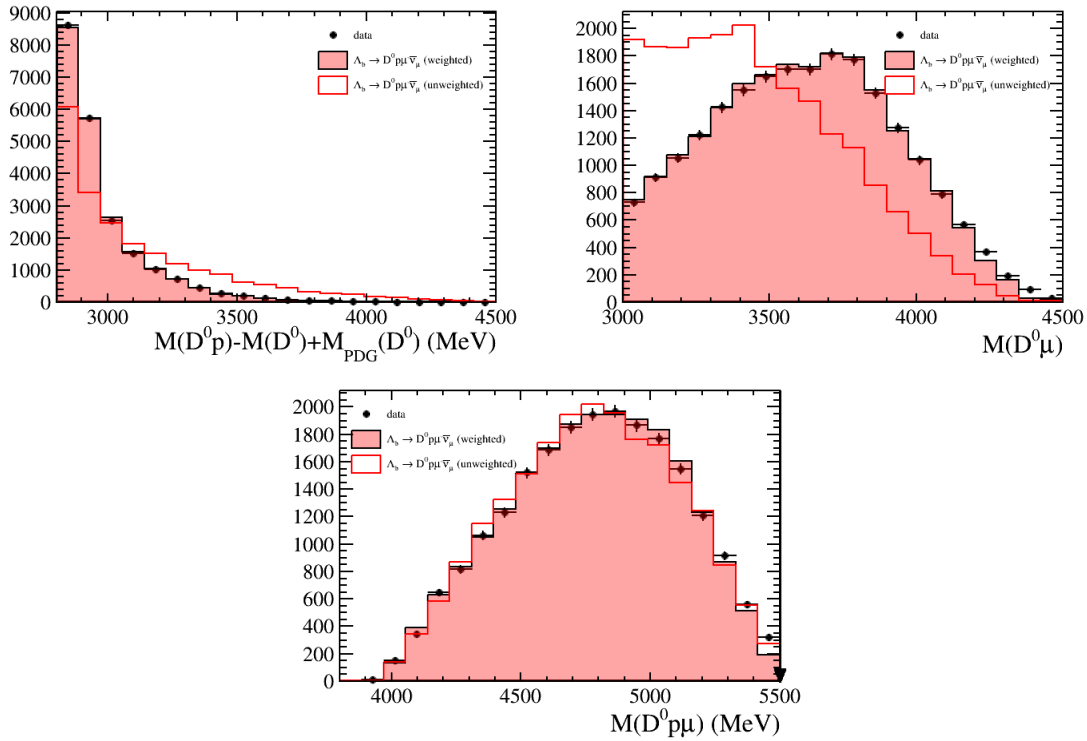

Figure 8.1: Comparison of data (black points) and simulation for the $\Lambda_b^0 \to D^0 p\mu^-\overline{\nu}_\mu X$ channel before (red line) and after (red shaded area) three-dimensional reweighting as described in the text (see Sec. 8.2).

no theoretical prediction of the $\Lambda_b^0 \to D^0 p\mu^-\overline{\nu}_\mu X$ channel is available. The plots in Figure 8.1 show a comparison of data (black points) and the simulation (red lines). A huge disagreement between the (unweighted) simulation and data can be seen, above all in the $M(D^0p)$ and $M(D^0\mu^-)$ distributions. In order to adjust the decay kinematics, the simulated events hence have to be reweighted. This leads to a more proper estimate of the efficiency. Several reweigthing steps are applied and will be described in the following. The effect of the reweighting is also shown in Figure 8.1. A discussion on it follows.

8.1 Kinematic reweighting of the simulated $\Lambda_b^0 \to D^0 p\mu^-\overline{\nu}_\mu X$ and $\Lambda_b^0 \to \Lambda_c^+\mu^-\overline{\nu}_\mu$ decays

The production of Λ_b^0 baryons depends strongly on their transverse momentum as Figure 8.2 (left) taken from Reference [63] shows. This dependence is not well emulated in the simulation and thus has to be corrected. This was already done in the semileptonic LHCb-measurement of $|V_{ub}|$ in Ref. [11] using the decay $\Lambda_b^0 \to J/\psi\, D^0 p$. To calculate the weights, data and simulation of this hadronic Λ_b^0 decay

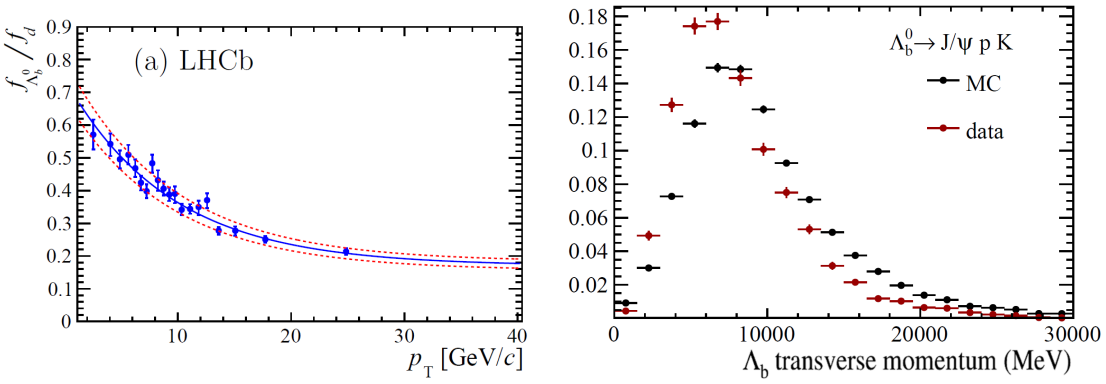

Figure 8.2: Left: Ratio of Λ_b^0 to B^0 production as a function of p_T. Figure taken from [63]. Right: Transverse Λ_b^0 momentum for $\Lambda_b^0 \to J/\psi\, D^0 p$ decays in data and simulation. Figure taken from the documentation belonging to [11].

channel was compared as shown in Figure 8.2 (right). In this analysis, the applied weights are determined from the same channel with the help of the distributions in Figure 8.2 (right). The reweighting is applied in both, $\Lambda_b^0 \to D^0 p\mu^- \overline{\nu}_\mu X$ and $\Lambda_b^0 \to \Lambda_c^+ \mu^- \overline{\nu}_\mu$, channels according to the true Λ_b^0 transverse momentum p_T, i.e. the actual generated transverse momentum.

8.2 Reweighting of the simulated $\Lambda_b^0 \to D^0 p\mu^- \overline{\nu}_\mu X$ decays

It has already been mentioned that the decay dynamics of the $\Lambda_b^0 \to D^0 p\mu^- \overline{\nu}_\mu X$ decay is not correctly modeled in the simulation. Since there are no theoretical predictions for that channel, the reweighting of the simulation has to be done directly on data. To come as close to data as possible, a three-dimensional reweighting in the variables, M($D^0 p$), M($D^0\mu^-$), M($D^0 p\mu^-$) has been chosen. This choice is not trivial and above all not obvious, but there are several reasons for it:

1. The simulation shows large differences compared to the data distribution in these variables.

2. These variables are already available at generator level, i.e. before detector effects are simulated. To calculate the selection efficiency, the simulation has to be reweighted at generator stage as well.

3. There are no selection requirements on these variables. Otherwise, no weights could be assigned to events, not fulfilling the requirements[1].

[1]There exists a selection requirement on M($D^0 p\mu^-$) in this analysis to eliminate $\Lambda_b^0 \to D^0 p\pi^-$

The reweighting and the calculation of the efficiencies is performed with the following steps:

1. **Determination of the weights**
   There are two normalised three-dimensional histograms drawn for both, data[2] as well as simulated events after reconstruction, applying selection cuts and the kinematic reweighting. The dimensions of these histograms are the three mass variables mentioned above. The histogram containing the weights is now calculated by dividing the histogram with the data through the histogram containing the simulated events.

2. **Assigning weights to the events**
   Now, this weight histogram is used to assign a weight w to each selected and generated event. To get the correct bin in the weight histogram, the generated masses $M_{\text{true}}(D^0p)$, $M_{\text{true}}(D^0\mu^-)$ and $M_{\text{true}}(D^0p\mu^-)$ are used, in the following briefly denoted as $\vec{M}_{\text{true}}$.

3. **Calculation of the efficiency**
   The efficiency is calculated with

$$\epsilon = \frac{\sum_{i=1}^{N_{\text{sel}}} w_i(\vec{M}_{\text{true}})}{\sum_{i=1}^{N_{\text{gen}}} w_i(\vec{M}_{\text{true}})}, \tag{8.1}$$

   where N_{sel} and N_{gen} denote the number of selected respectively generated events. To account for the loss of statistical power due to reweighting, both, the numerator and denominator in Equation (8.1), are multiplied by the renormalisation factor $\sum_{i=1}^{N_{\text{gen}}} w_i / \sum_{i=1}^{N_{\text{gen}}} w_i^2$. This does not affect the central value of ϵ, but influences the statistical error, which is calculated using binomial statistics [64], i.e.

$$\sigma_\epsilon = \sqrt{\frac{\epsilon(1-\epsilon)}{n}}, \tag{8.2}$$

   with $n := \sum_{i=1}^{N_{\text{gen}}} w_i(\vec{M}_{\text{true}})$.

It becomes clear, that with this procedure, one must not apply selection requirements on the weighting variables, since otherwise the weights outside the cut region are zero. Hence, it would not be clear, how to reweight the generated events not fulfilling the selection requirements. The distribution of the masses after reweighting are shown in Figure 8.1. The agreement between data and the reweighted simulation

background, but less than 0.5% of all events have their generated mass above this value. Thus, its impact on the efficiency can be neglected.

[2] Note, that again a $\log \chi^2_{\text{IP}} < 1$ is required to suppress combinatorial background.

is much better than without reweighting. Nonetheless, some discrepancies can be seen at higher $D^0\mu^-$ and $D^0p\mu^-$ masses. They arise due to empty bins in either data or simulation. The last two bins in $M(D^0\mu^-)$ in Figure 8.1 serve as an good example. No simulated events exist here, though there is still data. Nonetheless, these events are weighted with zero, resulting in slight discrepancies. Many more comparisons between data and simulation before and after reweighting can be found in the Appendix B in Figure B.1.

Concerning the channel $\Lambda_b^0 \to \Lambda_c^+\mu^-\overline{\nu}_\mu$, no further reweighting is applied since the agreement in the comparison between data and simulation seems to be sufficient. Several comparison plots for this channel can be found in Figure C.1 in Appendix C. With this framework, the efficiencies are calculated at different stages of the simulation process.

8.3 Generator level efficiencies

As a reminder, generator level efficiencies arise due to the fact, that one demands the generated events to be in the LHCb acceptance and apply some (loose) requirements on the kinematics to accelerate the simulation process. The generator level samples are reweighted as described above: the $\Lambda_b^0 \to \Lambda_c^+\mu^-\overline{\nu}_\mu$ sample with the kinematic p_T (Λ_b^0) reweighting and the $\Lambda_b^0 \to D^0p\mu^-\overline{\nu}_\mu$ sample with both reweightings. For signal and normalisation channel, the following generator level efficiencies are obtained:

$$\epsilon_{\mathrm{gen},\Lambda_c^+} = 0.345 \pm 0.016,$$
$$\epsilon_{\mathrm{gen},D^0p} = 0.2026 \pm 0.0070.$$

The quoted error is statistical and calculated as described in the previous section.

8.4 Reconstruction and selection efficiencies

The reconstruction and selection efficiencies are calculated analogously. The same reweighting procedure on the different samples is performed. The results for signal and normalisation channel are:

$$\epsilon_{\mathrm{sel},\Lambda_c^+} = (3.810 \pm 0.023) \times 10^{-3},$$
$$\epsilon_{\mathrm{sel},D^0p} = (8.30 \pm 0.17) \times 10^{-3}.$$

Again, the error relies to limited simulation statistics.

8.5 Total efficiencies

To summarise the values above, the total efficiencies for the channels are:

$$\epsilon_{D^0p} = \epsilon_{\mathrm{gen},D^0p} \cdot \epsilon_{\mathrm{sel},D^0p} = (1.682 \pm 0.067) \times 10^{-3},$$
$$\epsilon_{\Lambda_c^+} = \epsilon_{\mathrm{gen},\Lambda_c^+} \cdot \epsilon_{\mathrm{sel},\Lambda_c^+} = (1.314 \pm 0.063) \times 10^{-3}.$$

This results in an efficiency ratio of

$$\frac{\epsilon_{\Lambda_c^+}}{\epsilon_{D^0 p}} = 0.781 \pm 0.049,$$

which is later used when determining the relative branching ratio $\mathcal{R}$. The quoted errors are statistical and propagated from the the two latter sections. Systematic uncertainties due to the reweighting itself are discussed in Chapter 10.

Chapter 9

Backgrounds

The big disadvantage of semileptonic decays is that the neutrino cannot be reconstructed. At hadron colliders like the LHC, it is impossible to know the kinematics of the initial state, so one does not have enough constraints to reconstruct the full kinematic information about the decaying particle. Being aware of these problems due to the experimental setup, it is clear, that one cannot use a well reconstructed Λ_b^0 mass peak to separate signal from background. A main source of background is expected to be the decay $B^0/B^+ \to D^0\mu^-\overline{\nu}_\mu X$ where one randomly combines a proton to this decay. This background is handled by the fit of the $\log\chi^2_{\mathrm{IP}}$ distribution. Other sources of backgrounds and their possible impact on the obtained signal yield N_{D^0p} are discussed in the following. For the $\Lambda_b^0 \to \Lambda_c^+\mu^-\overline{\nu}_\mu$ channel it is assumed, that all non-negligible backgrounds are accounted for due to the sideband-subtraction and including wrong sign events as well as resonant mode components in the fit. Thus, the discussion in this chapter refers completely to the $\Lambda_b^0 \to D^0p\mu^-\overline{\nu}_\mu X$ channel.

9.1 Proton misidentification

A possible source of backgrounds is to misinterpret a decay as $\Lambda_b^0 \to D^0p\mu^-\overline{\nu}_\mu X$ if one misidentifies a final state particle. In this analysis, it is most likely that the proton is fake, since the final state pion and kaon are reconstructed to a D^0 yielding in a nice peak and the muon leaves a clear signature in the detector due to its relatively long lifetime and low interaction with matter. Examples for this kind of backgrounds are the decays $B_s^0 \to D^0K^+\mu^-\overline{\nu}_\mu X$ and $B^0/B^+ \to D^0\pi^+\mu^-\overline{\nu}_\mu X$, where either the K^+ or π^+ is misidentified as proton. Though there are tight requirements on the proton identification at selection stage, the data is still polluted by misidentified particles. To identify the amount of misidentified protons, a slightly different data sample than the nominal one is used. In this sample, no requirements on the proton idenfication are applied. All other requirements are the same as described in Section 5. However, the removal of the particle identification requirements for the protons lets the data size of the sample rapidly increase. To keep the data size acceptable, a so called 5% prescaling is applied, i.e. only 5% of all events are actually stored. The decision, if a particle is stored or not, is made by random. That is why absolute numbers quoted in this section cannot be compared to the obtained signal yields etc. in the previous sections. The study on misidentified backgrounds is done in

three steps.

9.1.1 Definition of particle identification regions - Number of particle candidates

As a first step, it has to be defined, what requirements have to be fulfilled, that a particle is called a proton, pion or kaon. For that purpose, the PID (for Particle IDentification) variables are used. Remember, that LHCb's particle identification system provides likelihoods for each particle hypothesis. The PID variables describe differences between the logarithms of these likelihoods, e.g. PIDp is defined as the difference of the logarithmic likelihoods between the proton and pion hypothesis. A value of PIDp > 0 hence means, that the particle is more likely a proton than a pion. Respectively, the PIDK compares kaon to pion hypothesis. If one wants to separate protons from kaons, it is useful to look at PIDp−PIDK. The definition what will be called proton is motivated by the requirements applied in the analysis (see Section 5). In detail, the regions for the identification of protons, pions and kaons are:

- pion: PIDp < 10.0 and PIDK < 0.0
- proton: PIDp − PIDK > 10.0 and PIDp > 10.0
- kaon: PIDp − PIDK < 10.0 and PIDK > 0.0

Furthermore, these regions and their population are visualised in Figure 9.1. From this, the number of candidates for each particle species is obtained, in the following denoted as N^i_{cand}, with $i \in [\pi, K, p]$. The number of candidates are

$$N^{\pi}_{\text{cand}} = 5052 \pm 71, \tag{9.1}$$
$$N^{K}_{\text{cand}} = 2175 \pm 47, \tag{9.2}$$
$$N^{p}_{\text{cand}} = 989 \pm 31. \tag{9.3}$$

9.1.2 Determination of "true" candidates with PID efficiencies

This choice of regions is a bit arbitrary and it does not prevent real protons, pions and kaons to enter the other regions. With the PID variables, it is only possible to increase or decrease the probability, that a particle enters a "foreign" region. Thus, one needs to determine the efficiencies that a real proton, pion or kaon passes the requirements for the identification of being a proton, kaon or pion. For this purpose, the LHCb PIDcalib tool is used [65]. This tool includes calibration samples of decays, cleanly reconstructed without use of the PID variables. For instance, one uses the decay $\Lambda \to p\pi^-$ for the determination of proton efficiencies. Since no requirement on the PID has been applied before, it is now possible to study the impact of

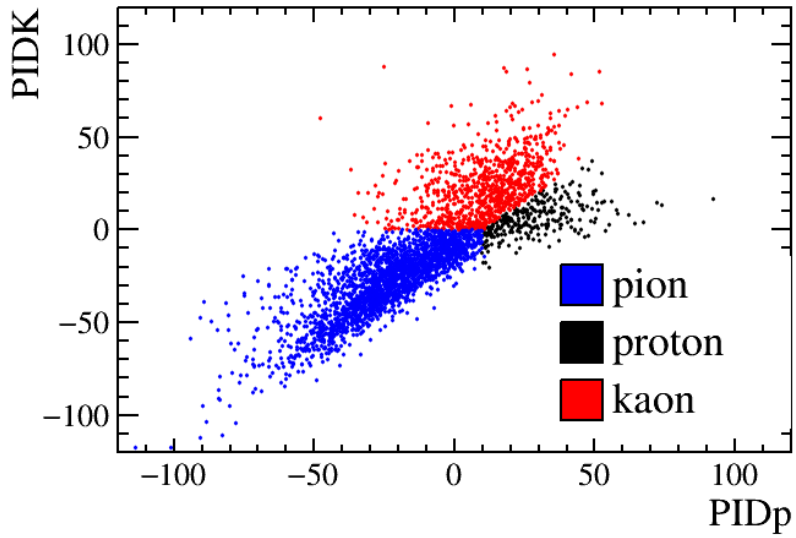

Figure 9.1: Defined regions for the number of particle candidates. Events in black are defined as protons, red as kaons and blue as pions.

these requirements. The PID efficiency for each of the 9 possible combinations (real particle to be identified as other particle according to PID) is determined binwise depending on the particle momentum. The results can be seen in Figure 9.2. The top left figure clearly shows that pions and kaons hardly fulfil the tight requirements PIDp > 10 and PIDp−PIDK > 10 made on the proton identification in the reconstruction of $\Lambda_b^0 \to D^0 p\mu^- \overline{\nu}_\mu X$ and $\Lambda_b^0 \to \Lambda_c^+ \mu^- \overline{\nu}_\mu$. Only, if they have a momentum of about 20 GeV there is a little chance to pass the selection. To determine a final value for each identification efficiency and to account for differences in the kinematics between the decays of the test samples and the $\Lambda_b^0 \to D^0 p\mu^- \overline{\nu}_\mu X$ decay, the histograms are weighted with respect to the kinematic distribution of the $\Lambda_b^0 \to D^0 p\mu^- \overline{\nu}_\mu X$ data. The result is:

$$\begin{pmatrix} \epsilon_{\pi^+\to\pi^+} & \epsilon_{K^-\to\pi^+} & \epsilon_{p\to\pi^+} \\ \epsilon_{\pi^+\to K^-} & \epsilon_{K^-\to K^-} & \epsilon_{p\to K^-} \\ \epsilon_{\pi^+\to p} & \epsilon_{K^-\to p} & \epsilon_{p\to p} \end{pmatrix} = \begin{pmatrix} 0.9409 & 0.0241 & 0.1309 \\ 0.0474 & 0.9681 & 0.3798 \\ 0.0117 & 0.0077 & 0.4893 \end{pmatrix}$$

Here, $\epsilon_{i\to j}$ denotes the efficiency, that a real (true) particle i is identified as what is called j according to the particle regions defined in Section 9.1.1. For the following steps, PID efficiency errors are assumed to be negligible compared to the corresponding uncertainties of the particle candidates N^i_{cand}. With the PID efficiencies $\epsilon_{i\to j}$ and the number of particle candidates N^k_{cand}, the number of real (true) particles can now be estimated by solving the matrix equation

$$\begin{pmatrix} N^\pi_{\text{cand}} \\ N^K_{\text{cand}} \\ N^p_{\text{cand}} \end{pmatrix} = \begin{pmatrix} \epsilon_{\pi\to\pi} & \epsilon_{K\to\pi} & \epsilon_{p\to\pi} \\ \epsilon_{\pi\to K} & \epsilon_{K\to K} & \epsilon_{p\to K} \\ \epsilon_{\pi\to p} & \epsilon_{K\to p} & \epsilon_{p\to p} \end{pmatrix} \begin{pmatrix} N^\pi_{\text{true}} \\ N^K_{\text{true}} \\ N^p_{\text{true}} \end{pmatrix}.$$

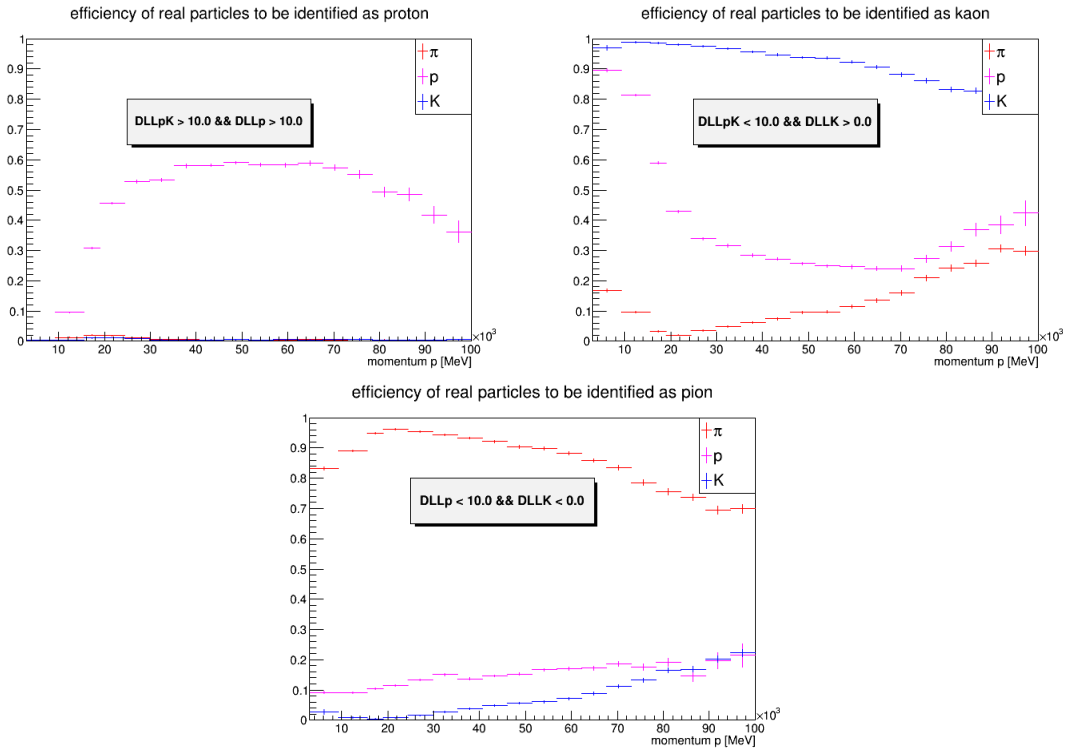

Figure 9.2: Efficiencies that real protons, kaons and pions are identified as protons (top left), kaons (top right) or pions (bottom). The tight requirements on the proton PID applied in this analysis ensures that only few kaons and pions enter the proton region paying the prize, that one looses a lot of protons as well.

Assuming that the efficiency matrix is invertible, one obtains

$$N^{\pi}_{\text{true}} = 5075 \pm 76, \tag{9.4}$$
$$N^{K}_{\text{true}} = 1260 \pm 55, \tag{9.5}$$
$$N^{p}_{\text{true}} = 1880 \pm 65. \tag{9.6}$$

N^{i}_{true} denotes the number of real particles i in the sample.

9.1.3 Estimate of misidentified protons

Using the results of the previous subsections it is now possible to estimate the number of misidentified protons, i.e. “true" kaons or pions entering the proton region. This is calculated by multiplying the number of “true" particles N^{i}_{true} with

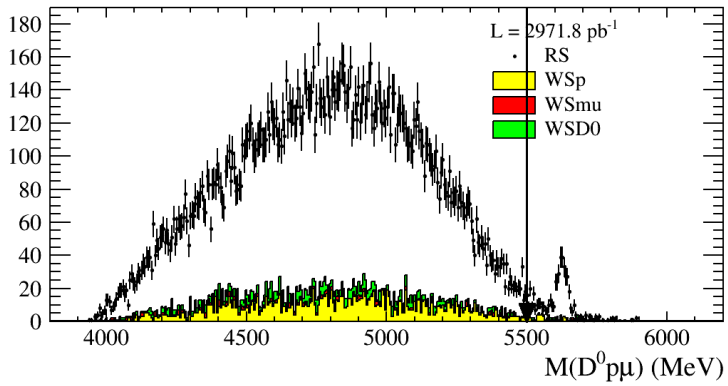

Figure 9.3: Invariant $D^0 p\mu^-$ mass. A peak at Λ_b^0 mass ($\approx 5620\,\text{MeV}$) can be seen caused by misidentified muons coming from hadronic decays like $\Lambda_b^0 \to D^0 p\pi$ where the pion is misidentified as muon. A veto on the $D^0 p\mu^-$ mass indicated by the arrow eliminates such backgrounds.

the PID efficiency $\epsilon_{i\to p}$ to be identified as proton.

$$N^\pi = \epsilon_{\pi\to p} N^\pi_{\text{true}} = 59.25 \pm 0.89, \tag{9.7}$$
$$N^K = \epsilon_{K\to p} N^K_{\text{true}} = 9.74 \pm 0.42, \tag{9.8}$$
$$N^p = \epsilon_{p\to p} N^p_{\text{true}} = 920 \pm 32. \tag{9.9}$$

Thus, the amount of misidentified protons is at a single-digit percent level, namely $(6.98 \pm 0.24)\%$. Note again, that the absolute values cannot be compared to the signal yields obtained in previous parts of this analysis. It is only the lastly quoted ratio which can be used in the following.

9.2 Misidentified muons

Though not as prominent as misidentified protons, the misidentification of muons is also considered. One possibility is that the muon is misidentified from an exclusive 3-body decay of the Λ_b^0 for instance $\Lambda_b^0 \to D^0 p\pi^-$. If this is the case, the decay is not semileptonic but rather hadronic. Consequently, the Λ_b^0 can be fully reconstructed since all final state particles are seen. This leads to a peak in the invariant $D^0 p\mu^-$ mass around the nominal Λ_b^0 mass. There is indeed such a peak as figure 9.3 shows. Thus, this kind of backgrounds can be easily eliminated by vetoing $D^0 p\mu$ masses around the Λ_b^0 mass, in this case all masses above 5500 MeV.

The situation becomes more tricky, if the background is coming from a multi-body Λ_b^0 decay, i.e. a decay with more than three final state particles. Since this analysis aims to measure the inclusive branching ratio $\mathcal{B}\,(\Lambda_b^0 \to D^0 p\mu^- \overline{\nu}_\mu X)$, misidentified muons could also come from decays like $\Lambda_b^0 \to D^0 p3\pi$, where one of the 3 pions is misidentified as muon. These backgrounds are not easy to eliminate, since the

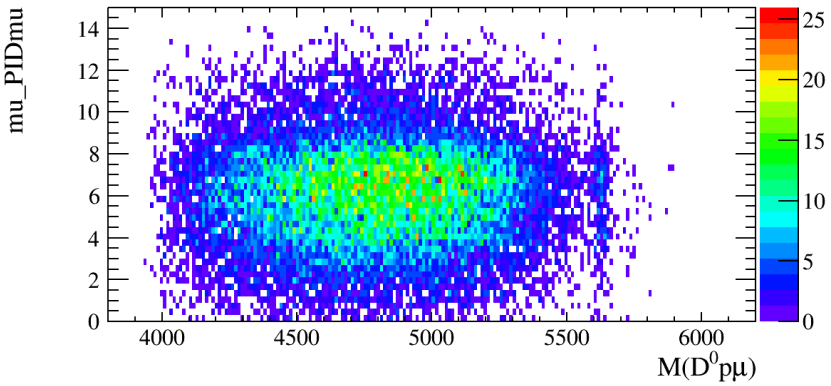

Figure 9.4: Invariant $D^0 p\mu^-$ mass versus PIDmu of the muon. No structures tending to low PIDmu can be seen.

other 2 pions are not reconstructed and the decay is thus not peaking in $D^0 p\mu^-$ mass. Nonetheless, if they are existent in the data sample, it might be possible, that such backgrounds tend to sit at lower PIDmu of the muon saying the lower the PIDmu of a muon is the more likely it is to be a misidentified particle. Unfortunately, no distinct structures can be seen in Figure 9.4. This might be a hint that these backgrounds play a minor role. Assuming that the decay $\Lambda_b^0 \to D^0 p3\pi$ behaves in comparison to $\Lambda_b^0 \to D^0 p\pi^-$ similar to the meson decays $B^0 \to D^- 3\pi$ and $B^0 \to D^-\pi^+$ with $\mathcal{B}(B^0 \to D^- 3\pi) = (2.76 \pm 0.13) \cdot 10^{-3} \approx \mathcal{B}(B^0 \to D^-\pi^+) = (2.68 \pm 0.13) \cdot 10^{-3}$ (see [18]), they should have similar branching ratios and thus should equally leak as background into this analysis. A comparison with $\mathcal{B}(B^0 \to D^- 3\pi)/\mathcal{B}(B^0 \to D^-\ell^+\nu_\ell) \approx 10\%$ and the misidentification probability of a hadron of less than 10% [66] justifies the assumption that this background leaks with about 1% in the signal yield. Furthermore, there are other possible but not yet measured peaking backgrounds such as $\Lambda_b^0 \to D^0 p\rho^-$ or $\Lambda_b^0 \to D^0 p\pi^-\rho^0$. Since they have not been measured so far, their contribution can only be guessed. Starting from the 1% contribution of $\Lambda_b^0 \to D^0 p3\pi$ a conservative estimate of a total peaking background ratio of $(5.0 \pm 2.5)\%$ is assumed. The large error accounts for the uncertainty in the estimate how many other decay channels and how strongly they contribute.

9.3 Prompt D^0 mesons

With prompt D^0, one denotes D^0 mesons coming directly from the primary pp interaction, thus being not a product of other decaying particles. The production of prompt D^0 is usually a lot higher than the production of Λ_b^0 baryons. Prompt D^0 can be mixed up with the $\Lambda_b^0 \to D^0 p\mu^-\overline{\nu}_\mu X$ if one adds a fake muon or a muon from another source and a proton e.g. from the primary interaction. One typically measures a prompt D^0 background of about 1% in semileptonic b-hadron decays

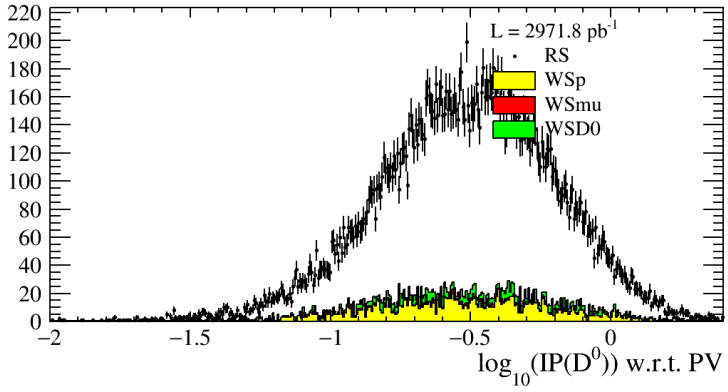

Figure 9.5: Logarithm of the D^0 impact parameter with respect to the primary pp interaction. No special behaviour of the wrong sign combinations indicating an enhancement of prompt D^0 background can be seen.

[10]. As cross-check, the logarithm of the D^0 impact parameter with respect to the primary vertex is drawn. Prompt D^0 should have a smaller impact parameter compared to D^0 coming from the Λ_b^0 decay. This should become more clearly visible in wrong sign combinations with respect to the right sign data. However, Figure 9.5 does not show any discrepancies between data and wrong sign combinations, which would indicate the influence of prompt D^0 backgrounds. Furthermore, one requires in the reconstruction process that the D^0 candidate is combined with a μ^- and a p to form a Λ_b^0 candidate at a secondary vertex displaced from the primary interaction. Thus, it seems that the selection requirements in the reconstruction process suppress the prompt D^0 background to an negligible amount compared to other backgrounds.

9.4 Other possible backgrounds

In this section, some possible backgrounds not being studied in this analysis are mentioned. Some of these decays have not been measured or seen so far, but should be possible.

- $\Lambda_b^0 \to D^0 D^- p$:
  This decay has not been measured yet. For semileptonic $D^- \to \mu^- X$ decays, where one misses the X, this channel mimics to be $\Lambda_b^0 \to D^0 p \mu^- \overline{\nu}_\mu X$ signal.

- $\Lambda_b^0 \to D^- \Lambda_c^+$:
  This decay has not been measured yet. It fakes to be signal, if the kaon of $\Lambda_c^+ \to pK^-\pi^+$ is misidentified as muon and the D^- decays to the doubly Cabbibo-suppressed mode $D^- \to K^-\pi^0$ with missing the π^0.

- prompt $\Lambda_c(2880)^+$ or $\Lambda_c(2940)^+$ decays with a randomly combined μ^-:
  This background should be reduced by requiring the $\Lambda_c(2880)^+$ respectively

$\Lambda_c(2940)^+$ vertex to be well separated from the PV as done by the combination with a muon to make a Λ_b^0 candidate.

Since the two Λ_b^0 decays mentioned above have not been measured yet, it is hard to estimate their contribution. To account for these backgrounds, it is assumed that the conservative estimate in Section 9.2 with an uncertainty of 2.5% covers them as well.

9.5 Backgrounds summary and estimate of background yield

The largest background contributions leaking into the signal yield N_{D^0p} obtained by the two-dimensional fit are discussed to come from either misidentified protons or muons. All other backgrounds seem to be negligible compared to the latter ones or are included in a conservative estimate with a large uncertainty. Adding them up leads to a total ratio of background events in the signal yield of $(12.0 \pm 2.5)\%$. This corresponds to a number of background events of

$$N_{D^0p}^{\text{bgd}} = 2750 \pm 100.$$

Note, that the error on the background ratio will be assigned as the systematic uncertainty.

Chapter 10

Systematics

In this section, studies on systematic uncertainties are presented. They will not be presented as systematic uncertainty on $\mathcal{R}$, but rather discussed separately for the signal yields and the efficiencies.

10.1 Branching ratio uncertainty of subsequent decays

Regarding Equation (4.2), a precise knowledge of the daughter decays' $D^0 \to K^-\pi^+$ and $\Lambda_c^+ \to pK^-\pi^+$ branching ratios is essential for the determination of $\mathcal{R}$. The values used in this analysis are taken from PDG [18] for $\mathcal{B}(D^0 \to K^-\pi^+)$ and from a recent Belle measurement [53] for $\mathcal{B}(\Lambda_c^+ \to pK^-\pi^+)$. They are

$$\mathcal{B}(D^0 \to K^-\pi^+) = 0.03880 \pm 0.00050,$$
$$\mathcal{B}(\Lambda_c^+ \to pK^-\pi^+) = 0.0684 \pm 0.0024.$$

Their errors are assigned as systematic uncertainty of $\mathcal{R}$. They correspond to a relative systematic uncertainty of 1.29% respectively 3.51%.

10.2 Kinematic p_{T} (Λ_b^0) reweighting of $\Lambda_b^0 \to D^0 p\mu^-\overline{\nu}_\mu X$ and $\Lambda_b^0 \to \Lambda_c^+\mu^-\overline{\nu}_\mu$ simulated events

To account for the wrong emulation of the Λ_b^0 kinematics in the simulation, both, the $\Lambda_b^0 \to D^0 p\mu^-\overline{\nu}_\mu X$ and the $\Lambda_b^0 \to \Lambda_c^+\mu^-\overline{\nu}_\mu$ simulation events have been reweighted in the transverse momentum of the Λ_b^0. Compared to the reweighting of the $\Lambda_b^0 \to D^0 p\mu^-\overline{\nu}_\mu X$ decay model, this is a minor correction and it is thus sufficient to compare the efficiency ratio $\frac{\epsilon_{\Lambda_c^+}}{\epsilon_{D^0 p}}$ with and without the kinematic p_{T} (Λ_b^0) reweighting. The difference between both cases is assigned as systematic uncertainty and amounts to 0.00878 corresponding to 1.12%.

Table 10.1: Comparison of the efficiency $\epsilon_{\mathrm{sel},D^0p}$ for different numbers of bins in each dimension.

# bins	$\epsilon_{\mathrm{sel},D^0p}$	difference to nominal reweighting	in %
5	$(9.2\pm0.15)\cdot10^{-3}$	8.94×10^{-4}	10.77%
10	$(8.77\pm0.15)\cdot10^{-3}$	4.71×10^{-4}	5.68%
15	$(8.4\pm0.17)\cdot10^{-3}$	1.02×10^{-4}	1.23%
20	$(8.3\pm0.17)\cdot10^{-3}$	0.	0.00%
25	$(7.99\pm0.18)\cdot10^{-3}$	-3.14×10^{-4}	−3.78%
30	$(7.88\pm0.19)\cdot10^{-3}$	-4.18×10^{-4}	−5.03%
40	$(8.06\pm0.22)\cdot10^{-3}$	-2.44×10^{-4}	−2.94%

10.3 Reweighting of $\Lambda_b^0 \to D^0 p\mu^-\overline{\nu}_\mu X$ simulated events

10.3.1 Choice of reweighting dimensions

As it is not obvious which variables are the best for the reweighting of the $\Lambda_b^0 \to D^0 p\mu^-\overline{\nu}_\mu X$ simulation sample to determine the efficiency, the choice of a certain set of weighting variables is another source of a systematic uncertainty on the final result. Having a closer look at the comparisons between data and reweighted simulation (see Fig. B.1) one might argue, that both distributions still are not in good agreement regarding the particles' momenta. Thus, another three-dimensional reweighting in the momenta of the $D^0p\mu^-$, $D^0\mu^-$ and D^0 candidates is performed and compared with the nominal reweighting. The difference in the efficiencies ϵ_{D^0p} is 4.05×10^{-5} or 2.41%.

10.3.2 Number of bins per dimension

To reweight the data, the three dimensions are binned. Each dimension has been split up in 20 bins. It is thus interesting to see, how strong the efficiency depends on the choice of the number of bins. For this purpose the reweighting is redone for a variety of different numbers of bins. The results of the efficiency ϵ_{D^0p} and the difference to the nominal reweighting can be seen in Table 10.1. A binning with 5 bins per dimension is too coarse to satisfy the behaviour of the three dimensions. Using 40 bins per dimension, there are too many vanishing weighting bins where there is no data or simulation, hence pulling the other one down and distorting the reweighting. This effect can be nicely seen in Figure 10.1. As systematic uncertainty, the biggest deviation except for the reweighting with 5 or 40 bins per dimension is assigned, namely 5.68%.

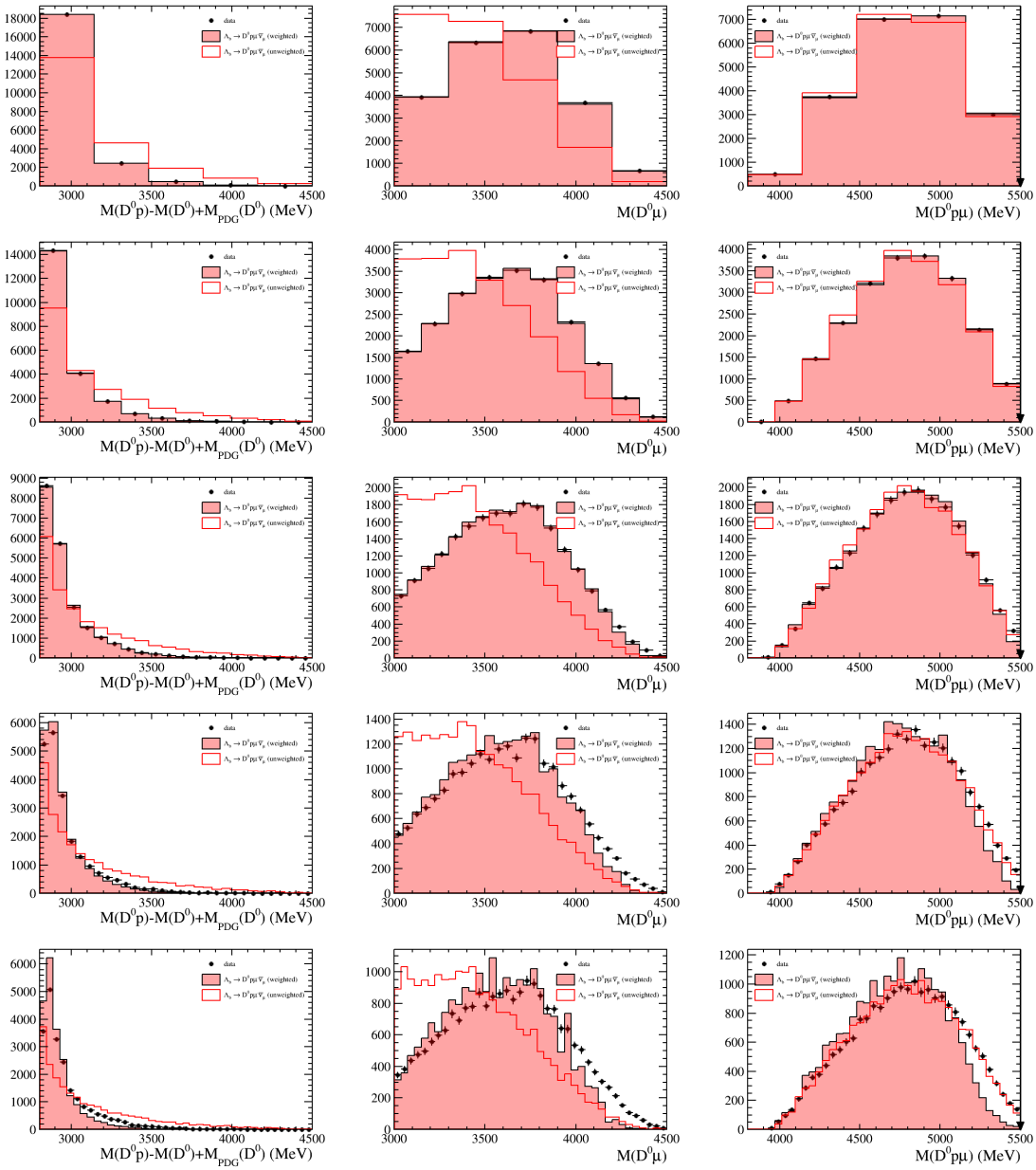

Figure 10.1: Comparison of data (black points) and simulation for the $\Lambda_b^0 \to D^0 p\mu^- \overline{\nu}_\mu X$ channel before (red line) and after (red shaded area) three-dimensional reweighting as described in the text (see Sec. 8.2) for different number of bins per dimension, namely 5, 10, 20, 30, 40 bins per dimension from top row to bottom row.

Table 10.2: Comparison of the efficiency $\epsilon_{\text{sel},D^0p}$ for different allowed maximum weights.

maximum weight	$\epsilon_{\text{sel},D^0p}$	difference to nominal reweighting	in %
5	$(8.79\pm0.15)\cdot10^{-3}$	4.84×10^{-4}	5.83%
10	$(8.4\pm0.16)\cdot10^{-3}$	9.60×10^{-5}	1.16%
15	$(8.32\pm0.17)\cdot10^{-3}$	2.00×10^{-5}	0.24%
20	$(8.3\pm0.17)\cdot10^{-3}$	0.	0.00%
25	$(8.3\pm0.17)\cdot10^{-3}$	-5.96×10^{-6}	−0.07%
30	$(8.29\pm0.17)\cdot10^{-3}$	-1.06×10^{-5}	−0.13%
40	$(8.28\pm0.17)\cdot10^{-3}$	-2.07×10^{-5}	−0.25%

10.3.3 Maximum allowed weight

When reweighting events, there might be some outliers getting a much higher weight than most of the other events. Such events dominate a reweighting disproportionally. To shrinken the impact of single outlier events, a maximum allowed weight of 20 has been defined in the reweighting process. All events with a higher weight are weighted with this maximum weight. Analogously to the study of the reweighting in different bins per dimension, a check of the efficiencies obtained by different maximum weights is done. The results can be seen in Table 10.2. Again, a maximum weight of 5 is a too tight restriction since there are too many events with weights larger than 5. Apart from that, the biggest discrepancy to the nominal case is taken as systematic uncertainty. The impact on $\mathcal{R}$ due to the allowed maximum weight amounts to 1.16%. Thus, it is a small effect compared to other systematics.

10.4 Choice of fit strategy

The determination of the $\Lambda_b^0 \to D^0 p\mu^-\overline{\nu}_\mu X$ signal yield is based on a two-dimensional fit to the D^0p mass and the $\log\chi^2_{\text{IP}}$ distribution. However, the distinction between signal and background is mainly based on the $\log\chi^2_{\text{IP}}$ distribution. Hence, it should be sufficient, to fit to the $\log\chi^2_{\text{IP}}$ distribution only, to extract the signal yield N_{D^0p}. As a cross-check, the signal yield N_{D^0p} is determined by a one-dimensional fit on the $\log\chi^2_{\text{IP}}$ distribution as described and reported in Section 6.1.2. The results are listed there in Table 6.1. The difference between this one-dimensional fit and the nominal two-dimensional fit amounts to 317.0 events which is equivalent to 1.38%.

10.5 Knowledge of backgrounds

A limited knowledge of the backgrounds contributing to the signal yields raises another systematic uncertainty. Different sources of backgrounds have been discussed in Chapter 9. In the end, it is concluded that the background fraction in the obtained signal yield N_{D^0p} is estimated to be $f_{\text{bkg}} = (12.0 \pm 2.5)\%$. Propagating the

Table 10.3: Summary of all considered systematics.

Systematic	N_{D^0p}	$N_{\Lambda_c^+}$	ϵ_{D^0p}	$\epsilon_{\Lambda_c^+}$	$\frac{\epsilon_{\Lambda_c^+}}{\epsilon_{D^0p}}$	$\mathcal{B}\,(\Lambda_c^+ \to pK^-\pi^+)$	$\mathcal{B}\,(D^0 \to K^-\pi^+)$
branching ratios	—	—	—	—	—	3.51%	1.29%
signal fit	1.38%	—	—	—	—	—	—
backgrounds	2.85%	—	—	—	—	—	—
Λ_b^0 p_T reweighting	—	—	—	—	1.12%	—	—
$\Lambda_b^0 \to D^0 p\mu^-\overline{\nu}_\mu X$ reweighting	—	—	2.41%	—	2.41%	—	—
bins per reweighting dimension	—	—	5.68%	—	5.68%	—	—
maximum weight in reweighting	—	—	1.16%	—	1.16%	—	—
total	3.17%	0.00%	6.27%	0.00%	6.37%	3.51%	1.29%

uncertainty on that estimate to the calculation of $\mathcal{R}$, this means a systematic uncertainty on N_{D^0p} due to the limited knowledge of the backgrounds of 576.0 events or 2.85%. Note, that the relative error is 2.85% and not just 2.5%, since one has to scale it up to the background subtracted signal yield $(1 - f_\mathrm{bkg})N_{D^0p}$.

10.6 Systematics overview

Table 10.3 summarises all considered systematics and gives a total value for each quantity. The reweighting process due to the poor physics description in the simulation is clearly the dominant systematic. It is followed by the uncertainty on the $\Lambda_c^+ \to pK^-\pi^+$ branching ratio. Summing them all up in quadrature, the total systematic error on $\mathcal{R}$ is

$$\Delta\mathcal{R}_\mathrm{syst.} = 0.0014$$
$$\frac{\Delta\mathcal{R}_\mathrm{syst.}}{\mathcal{R}} = 7.8\%$$

Chapter 11

Checks concerning the enhancement at low D^0p mass

In Chapter 6 it has been stated, that the fit to the D^0p mass spectrum needs an additional component to parametrise an anomalous enhancement at low D^0p masses right after threshold. The enhancement's yield is counted as signal to N_{D^0p} in this analysis. The following sections ought to show, that this is reasonable with the current knowledge about the enhancement.

The fit has converged and matched the data well, if this enhancement had been modeled like the two $\Lambda_c(2880)^+$ and $\Lambda_c(2940)^+$ resonances. This does not mean that there is really an additional or new resonance seen at all. There might be other reasons for the enhancement :

- Detector threshold / acceptance effects,
- Low mass behaviour induced by some selection requirements,
- Feed-down from partially reconstructed decays,
- Threshold enhancement due to wide resonances below D^0p mass threshold.

In this chapter, several checks are presented to either explain the origin of this enhancement or rule out some of the ideas. It should be mentioned, that there will not be a final answer to that question. If this was really something new, it would be really hard to prove it with a semileptonic decay channel. There is currently another LHCb analysis on the exclusive hadronic decay $\Lambda_b^0 \to D^0p\pi^-$ running, seeing a similar enhancement at low D^0p mass. This channel enables to study the enhancement with more methods for instance with an amplitude analysis. Hopefully, one can find a final answer with that decay. Nonetheless, the checks presented here are inevitable.

11.1 Detector threshold / acceptance effect

One possible explanation of the enhancement might be a simple threshold respectively acceptance effect of the detector. Such an effect could also be caused by the application of some selection requirements. To clarify this possibility and estimate the effects of the detector and the selection requirements, the simulation samples at

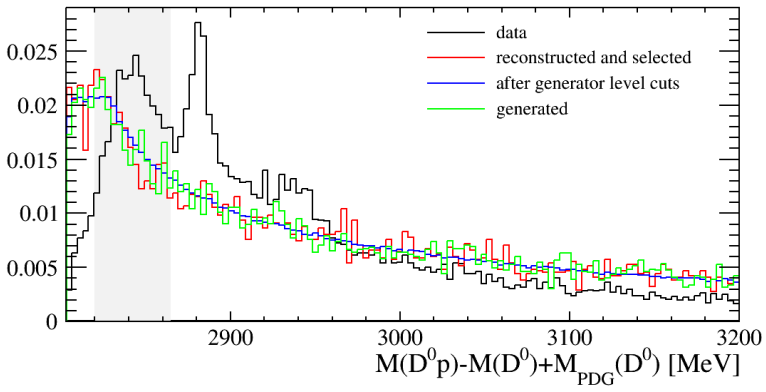

Figure 11.1: Simulated (true) invariant D^0p mass at different stages, namely after generation (green), detector simulation (blue) and reconstruction and selection (red). The black line shows the measured data. The simulated distributions in the highlighted enhancement region behaves very similar at all stages. Thus, the reconstruction and selection process is not responsible for the enhancement.

generator level and at reconstruction / selection level are used. Figure 11.1 shows the invariant D^0p mass at different stages of generation and reconstruction. The green distribution shows the D^0p mass at generation level, i.e. there is no simulation of the detector or any reconstruction applied here. In blue, one sees the D^0p mass after the simulation of the detector and in red the mass after reconstruction and selection. For comparison, the measured data distribution is shown in black as well. In this case, always the so called “true" masses are plotted, i.e. there are no influences of the detector resolution in these distributions. The simulations show a similar behaviour at all stages, especially in the enhancement region, which is highlighted in Figure 11.1. Thus, there is no significant acceptance effect arising, neither due to the detector itself nor due to the reconstruction and selection process that would lead to a peaking structure in the data distribution. Thus, the enhancement cannot be caused by such an effect.

At this point, it should be mentioned that there are other analyses seeing a similar behaviour in this D^0p mass region. First of all, there is a study by BaBar on the D^0p final state aiming to measure the $\Lambda_c(2880)^+$ and $\Lambda_c(2940)^+$ resonance (and in the latter case to even observe it) as shown in Figure 11.2 a). While discussing their systematics, they are wondering if this bump at roughly 2840 MeV might change their results by adding an additional resonance component to their fit, see Figure 11.2 c). Though that bump is much less pronounced compared to the enhancement in this anlaysis, it appears at the same mass. Since the impact is not that large on their final result, they just include the deviations as systematic uncertainty, unfortunately without trying to understand the origin of this bump [20].

Furthermore, there are two more ongoing LHCb studies on either prompt D^0p events and, as already mentioned, on the hadronic $\Lambda_b^0 \to D^0p\pi^-$ decay. It can be

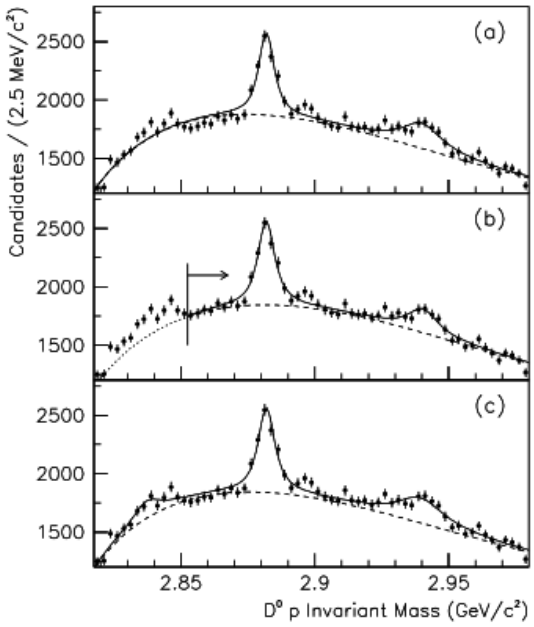

Figure 11.2: BaBar study on the D^0p final state. They suspect to see a structure similar to the enhancement in the current analysis and fit it in c) with an additional resonance component for their systematic studies. Figure taken from [20].

disclosed that they are struggling with the same problem, seeing a pronounced enhancement around 2840 MeV without being (currently) able to explain it. However, since there does not exist any approved material, nothing of their studies can be shown in this thesis.

Being seen in different channels and analyses substantiates the assumption, that there is a physical reason for the enhancement.

11.2 Threshold enhancement from other resonances

In principle, it might be possible that resonances below the D^0p mass threshold of 2803 MeV can enter the distribution due to their finite width. If this was the case, one would expect a very steep rise of the distribution at threshold region compared to a normal phase space behaviour. Though this does not seem to be the case if one looks left to the highlighted region in Figure 11.1, there are two resonance candidates which might cause such a threshold enhancement and should be briefly discussed here. There exists the broad $\Lambda_c(2765)^+$ about which is hardly anything known. Its width is currently quoted with 50 MeV in the PDG [18], but internal LHCb measurements on Λ_b^0 form factors show, that this is an overestimate of the

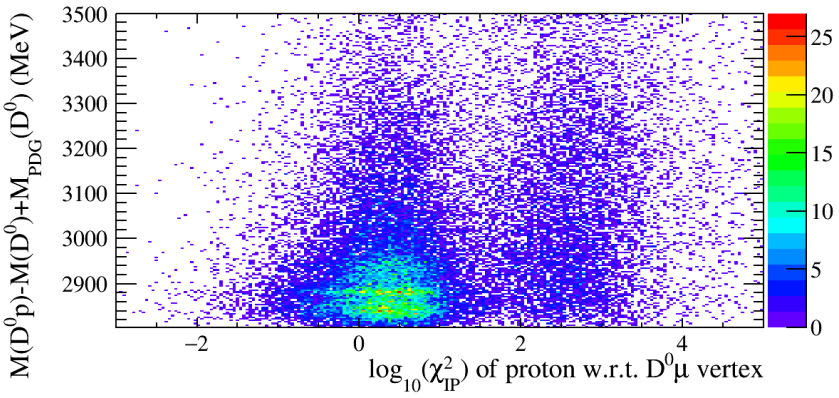

Figure 11.3: Invariant D^0p mass versus $\log\chi^2_{\mathrm{IP}}$ distribution. The $\Lambda_c(2880)^+$ and $\Lambda_c(2940)^+$ are clearly visible as bands in D^0p mass tending to cluster around $\log\chi^2_{\mathrm{IP}} \approx 0.5$. The observed enhancement behaves very similar compared to the resonances excluding that the enhancement can not be caused by combinatorial backgrounds.

$\Lambda_c(2765)^+$ width. The leakage into the D^0p mass spectrum should thus be negligible.

Another resonance exactly sitting at the D^0p mass threshold is the $\Sigma_c(2800)^+$. So far, it is only seen in the hadronic decay $\Sigma_c(2800)^+ \to \Lambda_c^+\pi^0$, but the decay $\Sigma_c(2800)^+ \to D^0p$ is not forbidden by any conservation law[1]. The mean mass of the $\Sigma_c(2800)^+$ with 2792^{+14}_{-5} MeV is indeed below the D^0p mass threshold of 2803 MeV, but it has a width of 62^{+60}_{-40} MeV [18] and is thus a possible candidate for a threshold enhancement. The $\Sigma_c(2800)^+$ itself could come from the decay $\Lambda_b^0 \to \Sigma_c(2800)^+\mu^-\overline{\nu}_\mu$, which has not been observed yet either. Thus, it is hard to estimate how probable a threshold enhancement by this $\Sigma_c(2800)^+$ is. Since this thesis aims for an inclusive measurement of the decay $\Lambda_b^0 \to D^0p\mu^-\overline{\nu}_\mu X$, the enhancement would still be signal if it was caused by either the decay of the $\Lambda_c(2765)^+$ or $\Sigma_c(2800)^+$, similar to the semileptonic Λ_b^0 decays via the $\Lambda_c(2880)^+$ or $\Lambda_c(2940)^+$ resonance.

11.3 Possible background sources

It has to be checked that the peaking structure of the enhancement is not caused by any kind of background. One can easily exclude that combinatorial background causes the enhancement. Firstly, it does not appear in the wrong sign D^0p mass distribution as already shown in Figure 6.9. Second, a two-dimensional plot of the invariant D^0p mass versus $\log\chi^2_{\mathrm{IP}}$ distribution shows that the enhancement obeys the same line structure over $\log\chi^2_{\mathrm{IP}}$ than the $\Lambda_c(2880)^+$ and $\Lambda_c(2940)^+$ resonances as can be seen in Figure 11.3. This means that the decay topology looks exactly

[1] The quark content of the $\Sigma_c(2800)^+$ is (udc)

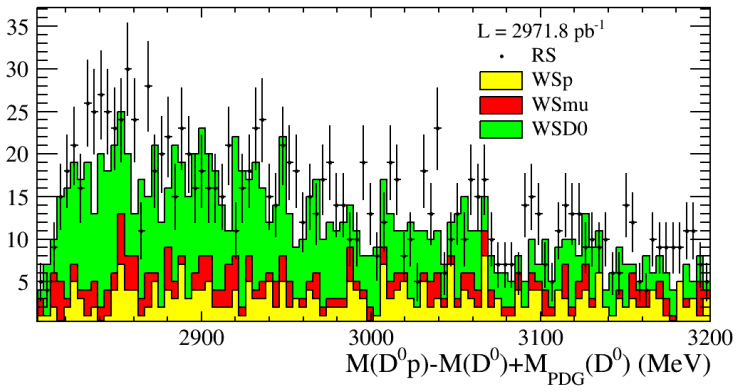

Figure 11.4: Invariant D^0p mass for events in the D^0 mass sidebands $M(D^0) < 1820\,\text{MeV}$ or $M(D^0) > 1910\,\text{MeV}$. No enhancement or any other peaking structure can be seen, indicating that fake D^0 backgrounds don't cause the enhancement.

the same for the enhancement and the resonances leading to the conclusion that the enhancement looks like signal.

Albeit, peaking backgrounds could enter the D^0p mass spectrum due to either a misidentified D^0 or p. For this purpose, the invariant D^0p mass is plotted for the D^0 mass sidebands, namely for events with $M(D^0) < 1820\,\text{MeV}$ or $M(D^0) > 1910\,\text{MeV}$. As these events are clearly away from the D^0 mass peak, they have to be background. Figure 11.4 shows that neither the enhancement nor any of the identified Λ_c^+ resonances appears here. This is a clear sign, that backgrounds from fake D^0 do not cause the enhancement.

It is left to check for fake protons. When estimating the amount of fake protons in Section 9.1, only an average value for the total misidentification ratio has been given. However, it is conceivable, that the misidentification ratio depends on the D^0p mass and is particularly high in the enhancement region. Thus, the estimate of the misidentification ratio is repeated for three bins in D^0p mass to see if fake protons are more likely to be in the enhancement region. One obtains for the misidentification ratio:

- $(3.64 \pm 0.27)\%$ for $M(D^0p) < 2860\,\text{MeV}$,
- $(6.12 \pm 0.32)\%$ for $2860 < M(D^0p) < 3000\,\text{MeV}$,
- $(11.63 \pm 0.73)\%$ for $M(D^0p) > 3000\,\text{MeV}$.

The bins have been chosen such that the first one only covers the enhancement region, the second bin the $\Lambda_c(2880)^+$ and $\Lambda_c(2940)^+$ resonances and the third bin the region above. Interestingly, the misidentification ratio is the smallest in the enhancement region. It is the region with least pollution from fake backgrounds. A further cross-check can be seen in Figure 11.5. Here, the invariant D^0p mass is plotted for different tight requirements on the particle identification (PIDp and

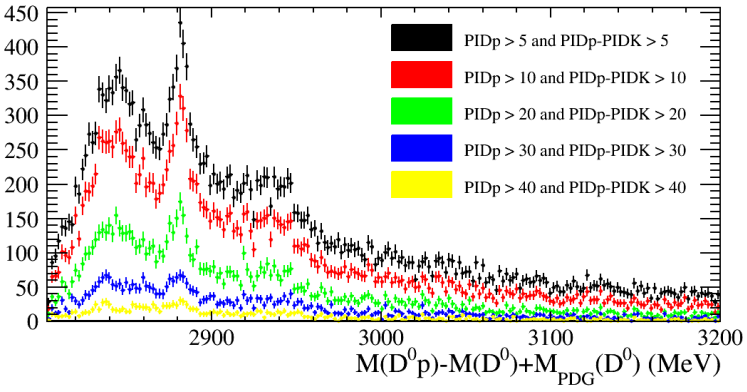

Figure 11.5: Invariant D^0p mass for different requirements on the proton's particle identification variables PIDp and PIDp−PIDK (for a definition of these variables see Chapter 5). The enhancement does not disappear with tighter requirements on the proton identification. This confirms that real protons make up the enhancement.

PIDp−PIDK) of the proton. All other requirements are the same as described in Chapter 5. If the enhancement is made up of events with particles misidentified as protons, then it should disappear if one tightens the requirements on the proton identification. However, this is not the case here. The enhancement stays as pronounced as the $\Lambda_c(2880)^+$ resonance for increasing PIDp and PIDp−PIDK variables and should thus be made up of real protons.

11.4 Partially reconstructed decays

Assuming that real protons and D^0 cause the enhancement, it is not confirmed that this enhancement is a resonance decaying into a D^0p. It might be, that one sees a so called "feed-down" from a partially reconstructed decay. Partially reconstructed decay means that not all particles participating in an event are reconstructed. A good example are semileptonic decays like $\Lambda_b^0 \to D^0 p \mu^- \overline{\nu}_\mu X$ since the neutrino is not reconstructed. This is furthermore an inclusive measurement, i.e. there might be in addition some not reconstructed particles X like kaons or pions. Above all the reconstruction of neutral pions is hard at LHCb. One possibility of getting a peak in D^0p mass without being a direct decay product would be that the inital Λ_b^0 decays semileptonically into some resonance R and this resonance R afterwards decays into a D^*p. The D^* decays into a $D\pi$ in turn. The total decay chain would then be $\Lambda_b^0 \to R\mu^-\overline{\nu}_\mu$, $R \to D^*p$ and $D^* \to D\pi$. If one misses the final state π and combines the D and the p to look at the invariant Dp mass, a peak would appear here, which is not the product of a direct resonant decay $\tilde{R} \to Dp$, but rather just the "reflection" or "feed-down" from a different decay of another resonance R. To check if the enhancement is a feed-down from a different decay and a potentially well-

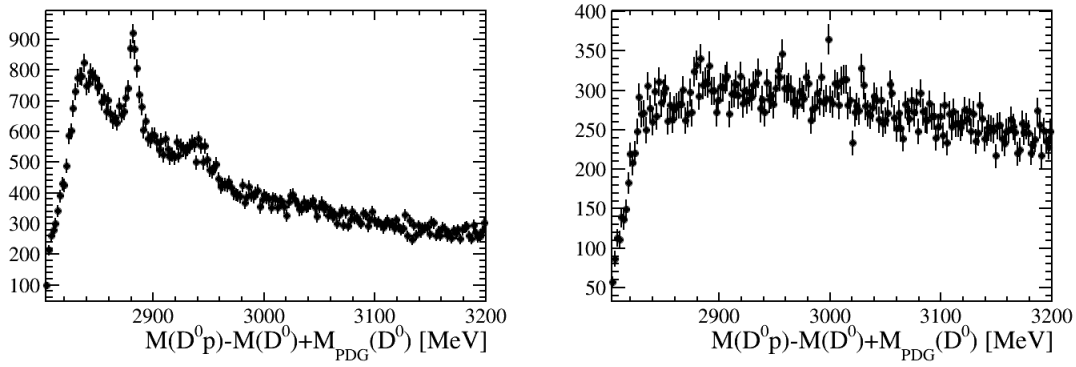

Figure 11.6: Invariant D^0p mass where no other (charged) hadron leaves the $D^0p\mu^-$ decay vertex (left) and with at least one additional hadron coming from the $D^0p\mu^-$ decay vertex. In the first case the $\Lambda_c(2880)^+$ and $\Lambda_c(2940)^+$ resonance as well as the enhancement are clearly visible. In the latter case with additional hadrons, the peaking structure and above all the enhancement vanishes. As a consequence, it is very probable that the enhancement originates from direct decays into D^0p.

known resonance, a tool recently developed by Marian Stahl, a Heidelberg Ph.D. student, is used. It enables to isolate tracks, i.e. it is possible to require and control, how many tracks come from a certain decay vertex. With this tool, two further plots of the D^0p invariant mass are produced and plotted in Figure 11.6: The left-hand side shows the invariant D^0p mass distribution with the requirement that no other charged hadron (e.g. π, K) track comes from the $D^0p\mu^-$ decay vertex. Thus, the plot shows Λ_b^0 decays into the $D^0p\mu^-$ final state without any other charged particles. Since neutral particles do not leave tracks in the detector, a contribution from neutral particles cannot be excluded, though. A D^0p mass spectrum similar to the distribution of the nominal fit in Figure 6.8 can be seen there including the resonances $\Lambda_c(2880)^+$ and $\Lambda_c(2940)^+$ as well as the enhancement. In the right plot of Figure 11.6 it is required that there is at least one additional charged particle coming from the $D^0p\mu^-$ decay vertex. Following this, it shows the invariant D^0p mass distribution for partially reconstructed decays. The $\Lambda_c(2880)^+$, $\Lambda_c(2940)^+$ resonances as well as the enhancement have vanished. This is a clear sign, that the enhancement likely decays into D^0p and is not an effect of partially reconstructed decays with missing a charged particle.

It should be noted again, that it is hard to conclude anything for additional neutral particles since they do not leave a track in the detector. Having D mesons in a mass spectrum, it is very common that one sees peaks coming from a partially reconstructed decay with a $D^* \to D\pi$. As a last check a possible impact on the D^0p mass spectrum for the special case of a $D^{*0} \to D^0\pi^0$ decay with missing the π^0 is estimated: Assuming that there exists a resonance R^+, obeying the decay chain $\Lambda_b^0 \to R^+\mu^-\overline{\nu}_\mu$, $R^+ \to D^{*0}p$ and $D^{*0} \to D^0\pi^0$, the question comes up, which mass

this resonance R^+ must have, to cause a peak in D^0p mass in the enhancement region. A simple phase space simulation delivers that this mass of R^+ should be about 2980 MeV. Indeed, there exists a resonance, namely the $\Xi_c(2980)^+$ with a mass of (2971 ± 3.3) MeV [18]. However, the quark content of a Ξ_c^+ is (ucs), whereas neither a D^{*0} nor the proton contain a s quark. Thus, the decay $\Xi_c(2980)^+ \to D^{*0}p$ would need to decay via the weak interaction. Nonetheless, the $\Xi_c(2980)^+$ is heavy enough to decay also strongly. That is why the potential decay $\Xi_c(2980)^+ \to D^{*0}p$ is highly suppressed. So there is currently no resonance known that can decay via a $D^{*0}p$ and have a mass that allows to peak in the D^0p mass.

11.5 General conclusions on the enhancement

In the previous sections, different attempts have been made to find either a solution or rule out some potential reasons of the enhancement seen in the invariant D^0p mass spectrum of the $\Lambda_b^0 \to D^0p\mu^-\overline{\nu}_\mu X$ channel. An effect from the detector as well as backgrounds especially from misidentified particles seems to be very unlikely. By all indications, there are real D^0 and protons involved in the nature of the enhancement. It is likely that the process responsible for the enhancement is directly decaying into a D^0p final state without being a “feed-down" from a partially reconstructed decay, whereas the presence of neutral particles cannot be ruled out. Finally, it can not be concluded if there is a new resonance appearing in the invariant D^0p mass spectrum. If this enhancement would be a new Λ_c^+ resonance, then it should be seen in the $\Lambda_c^+\pi^+\pi^-$ final state as well, which is not the case [18]. The question on the origin of the enhancement is still open and interesting to pursue. One has to keep in mind, that the main purpose of this thesis is the measurement of the inclusive branching ratio $\mathcal{B}\,(\Lambda_b^0 \to D^0p\mu^-\overline{\nu}_\mu X)$. Considering the fact that a lot of potential background sources causing the enhancement can be ruled out and the enhancement seems to decay into a D^0 and a proton, it should be justified that the yield of the enhancement is counted as signal to the total signal yield N_{D^0p} in the nominal fit (see Chapter 6).

Chapter 12

Results

This chapter summarises all the ingredients needed for the calculation of the relative branching ratio $\mathcal{R}$. As a reminder, the relative branching ratio of the decays $\Lambda_b^0 \to D^0 p\mu^-\overline{\nu}_\mu X$ and $\Lambda_b^0 \to \Lambda_c^+\mu^-\overline{\nu}_\mu$ is calculated by:

$$\mathcal{R} = \frac{\mathcal{B}(\Lambda_b^0 \to D^0 p\mu^-\overline{\nu}_\mu X)}{\mathcal{B}(\Lambda_b^0 \to \Lambda_c^+\mu^-\overline{\nu}_\mu)} = \frac{N_{D^0p}}{N_{\Lambda_c^+}} \cdot \frac{\epsilon_{\Lambda_c^+}}{\epsilon_{D^0p}} \cdot \frac{\mathcal{B}(\Lambda_c^+ \to pK^-\pi^+)}{\mathcal{B}(D^0 \to K^-\pi^+)}. \tag{12.1}$$

Concerning the signal yield N_{D^0p} of the $\Lambda_b^0 \to D^0 p\mu^-\overline{\nu}_\mu X$ channel, not all backgrounds could be separated in the signal fit, since it is only able to separate random background. In Chapter 9 additional background contributions like fake protons etc. have been discussed and a background yield $N_{D^0p}^{\text{bgd}}$ has been assigned. Thus the final calculation of R is modified to

$$\mathcal{R} = \frac{N_{D^0p} - N_{D^0p}^{\text{bgd}}}{N_{\Lambda_c^+}} \cdot \frac{\epsilon_{\Lambda_c^+}}{\epsilon_{D^0p}} \cdot \frac{\mathcal{B}(\Lambda_c^+ \to pK^-\pi^+)}{\mathcal{B}(D^0 \to K^-\pi^+)}. \tag{12.2}$$

Note, that for the fit to the reference channel $\Lambda_b^0 \to \Lambda_c^+\mu^-\overline{\nu}_\mu$ and the determination of $N_{\Lambda_c^+}$ it is assumed, that all non-negligible backgrounds are considered in the fit. The efficiency ratio $\frac{\epsilon_{\Lambda_c^+}}{\epsilon_{D^0p}}$ has been determined by the use of simulation samples. These had to be reweighted to better emulate the data distribution.

An overview of all important variables can be found in Table 12.1. With these values, me obtains for the relative branching ratio

$$\mathcal{R} = 0.0180 \pm 0.0013\,(\text{stat}) \pm 0.0014\,(\text{syst}).$$

The statistical and the systematic uncertainties are of same order. Concerning the statistical uncertainties, the main contribution comes from the statistical uncertainty on the efficiency ratio. The systematic uncertainties are dominated by the reweighting of the $\Lambda_b^0 \to D^0 p\mu^-\overline{\nu}_\mu$ channel.

As a side effect, the widths and masses of the peaking structures in the invariant

Table 12.1: Final results needed for the calculation of the relative branching ratio $\mathcal{R}$ according to Equation (12.2). The errors correspond to the statistical (first) and systematic (second) precision.

Variable	Value
Signal yields	
N_{D^0p}	$(2.29\pm0.09\pm0.07)\cdot10^4$
$N_{\Lambda_c^+}$	$(1.54\pm0.01\pm0.00)\cdot10^6$
Backgrounds	
$N^{\mathrm{bgd}}_{D^0p}$	$(2.75\pm0.10\pm0.00)\cdot10^3$
Branching ratios	
$\mathcal{B}(D^0\to K^-\pi^+)$	$(3.88\pm0.00\pm0.05)\cdot10^{-2}$
$\mathcal{B}(\Lambda_c\to p^+K^-\pi^+)$	$(6.84\pm0.00\pm0.24)\cdot10^{-2}$
Efficiencies	
ϵ_{D^0p}	$(1.68\pm0.07\pm0.11)\cdot10^{-3}$
$\epsilon_{\Lambda_c^+}$	$(1.31\pm0.06\pm0.00)\cdot10^{-3}$
$\frac{\epsilon_{\Lambda_c^+}}{\epsilon_{D^0p}}$	$(7.81\pm0.49\pm0.50)\cdot10^{-1}$

D^0p mass spectrum have been measured. The results are

$$
\begin{aligned}
\Lambda_c(2880)^+ : \quad & m_{\Lambda_c(2880)^+} = (2881.97 \pm 0.34\,(\mathrm{stat}))\,\mathrm{MeV},\\
& \Gamma_{\Lambda_c(2880)^+} = (7.5 \pm 1.3\,(\mathrm{stat}))\,\mathrm{MeV},\\
\Lambda_c(2940)^+ : \quad & m_{\Lambda_c(2940)^+} = (2937.5 \pm 1.7\,(\mathrm{stat}))\,\mathrm{MeV},\\
& \Gamma_{\Lambda_c(2940)^+} = (23.4 \pm 6.0\,(\mathrm{stat}))\,\mathrm{MeV},\\
\mathrm{enhancement} : \quad & m_{\mathrm{enh}} = (2842.04 \pm 0.87\,(\mathrm{stat}))\,\mathrm{MeV},\\
& \Gamma_{\mathrm{enh}} = (24.4 \pm 3.7\,(\mathrm{stat}))\,\mathrm{MeV}.
\end{aligned}
$$

No studies on systematic uncertainties of these values are done. As the enhancement and the $\Lambda_c(2880)^+$ resonance overlap, the widths of the peaking structures obviously depend on the parametrisation of the enhancement and are thus preliminary. Nonetheless, these (preliminary) results are in agreement with the current PDG values as discussed in Section 6.5.

Chapter 13

Conclusion

This thesis presents the first branching ratio measurement of the semileptonic decay $\Lambda_b^0 \to D^0 p\mu^- \overline{\nu}_\mu X$ in form of a relative branching fraction ratio $\mathcal{R} := \frac{\mathcal{B}(\Lambda_b^0 \to D^0 p\mu^- \overline{\nu}_\mu X)}{\mathcal{B}(\Lambda_b^0 \to \Lambda_c^+ \mu^- \overline{\nu}_\mu)}$. The analysed data was collected by the LHCb experiment during 2011 and 2012 and corresponds to an integrated luminosity of $3\,\mathrm{fb}^{-1}$. The determination of $\mathcal{R}$ requires in principle four quantities: the signal yields of the channels $\Lambda_b^0 \to D^0 p\mu^- \overline{\nu}_\mu X$ and $\Lambda_b^0 \to \Lambda_c^+ \mu^- \overline{\nu}_\mu$ as well as the corresponding reconstruction and selection efficiencies. Since only events with the daughter decays $D^0 \to K^-\pi^+$ and $\Lambda_c^+ \to pK^-\pi^+$ are reconstructed, $\mathcal{R}$ has to be corrected for their respective branching ratios. These values are taken from other experiments.

Due to the semileptonic nature of signal and normalisation channel, it is not possible to reconstruct the Λ_b^0 mass to get the signal yields. The signal yield of the decay $\Lambda_b^0 \to D^0 p\mu^- \overline{\nu}_\mu X$ is determined with a two-dimensional fit to the $D^0 p$ mass and the $\log \chi^2_{\mathrm{IP}}$ distribution. Being a measure of how well the p makes a vertex with the $D^0\mu^-$ candidate, $\log \chi^2_{\mathrm{IP}}$ enables to distinguish between signal and background from randomly combined protons. This is very helpful to disentangle the nonresonant $\Lambda_b^0 \to D^0 p\mu^- \overline{\nu}_\mu X$ decays from background in the $D^0 p$ mass spectrum. The fit yields in total $(2.293 \pm 0.088) \cdot 10^4$ signal candidates. However, the fit does not prevent that other backgrounds than randomly combined protons leak into the signal. It is shown that the main backgrounds are either fake protons or muons, i.e. decays, that mimic to be $\Lambda_b^0 \to D^0 p\mu^- \overline{\nu}_\mu X$ since one of the particles is misidentified as proton or muon. The leakage of backgrounds into the signal yield is estimated to be $(12.0 \pm 2.5)\%$.

An anomalous enhancement is observed in the invariant $D^0 p$ mass spectrum at a mass of about 2840 MeV. Different attempts to explain its origin do not provide a final solution. As it currently seems that this enhancement is anyhow part of an inclusive $\Lambda_b^0 \to D^0 p\mu^- \overline{\nu}_\mu X$ decay, its yield is counted as signal.

For the reference channel $\Lambda_b^0 \to \Lambda_c^+ \mu^- \overline{\nu}_\mu$, the main source of backgrounds are Λ_b^0 decays into excited Λ_c^{*+} states. These decays are identified by their lower corrected Λ_b^0 mass. The fit to the corrected mass is based on simulation templates and yields $(1.544 \pm 0.011) \cdot 10^6$ $\Lambda_b^0 \to \Lambda_c^+ \mu^- \overline{\nu}_\mu$ events. It is assumed that all relevant backgrounds are already subtracted before or in the fit.

For the determination of the reconstruction and selection efficiencies, the necessary simulations are reweighted, especially the simulation of the decay $\Lambda_b^0 \to D^0 p\mu^- \overline{\nu}_\mu X$.

The ratio of both efficiencies is determined to be $\epsilon_{\Lambda_c^+}/\epsilon_{D^0p} = 0.781 \pm 0.049$.

This leads to the final result of the relative branching ratio

$$\mathcal{R} = 0.0180 \pm 0.0013\,(\text{stat}) \pm 0.0014\,(\text{syst}).$$

The statistical and the systematic uncertainties are of same order. The biggest contribution to the systematic uncertainties comes from the reweighting process. It will certainly become more accurate if a proper theoretical physics description is available. There is currently no theoretical prediction to be compared with the obtained result. Since this is the first measurement of $\mathcal{B}\left(\Lambda_b^0 \to D^0 p \mu^- \overline{\nu}_\mu X\right)$ anyway, there are no other experimental results for comparison either.

What is left is the question of the origin of the enhancement at low D^0p mass. There are currently different ongoing analyses at LHCb observing a similar behaviour in the invariant D^0p mass. Hopefully, an explanation can be found with combined efforts. Since this enhancement overlaps with the $\Lambda_c(2880)^+$ resonance in the D^0p spectrum, the obtained masses and widths of the $\Lambda_c(2880)^+$ and $\Lambda_c(2940)^+$ are only preliminary. These results clearly depend on the parametrisation of the enhancement. Thus, the obtained properties of the $\Lambda_c(2880)^+$ and $\Lambda_c(2940)^+$ are not quoted here again. To get reliable results here, it has to be clear, what the enhancement's nature is and how large the impact of the $\Lambda_c(2765)^+$ and $\Sigma_c(2800)^+$ to the invariant D^0p mass at threshold is.

This thesis complements the results of BaBar on the $\Lambda_c(2880)^+$ and $\Lambda_c(2940)^+$ resonances [20]. With the first measurement of the decay $\Lambda_b^0 \to D^0 p \mu^- \overline{\nu}_\mu X$, it furthermore contributes to the currently largely unexplored b baryon sector. Both help to understand more of the dynamics of light quarks in the vicinity of the heavy b and might improve effective theories of QCD. The relative branching ratio $\mathcal{R}$ itself can be included in the background estimations of the a_{sl}^d or semileptonic $|V_{ub}|$ measurements presented in Chapter 2, to reduce systematic uncertainties. This is necessary to hopefully reveal the contributions of New Physics in future, since the current experimental precision is not sufficient for that purpose.

Appendix A

Mass resolution

Figure A.1 shows the fits to all bins of D^0p mass for the determination of the mass resolution. The whole method and prodecure is described in Section 6.2.

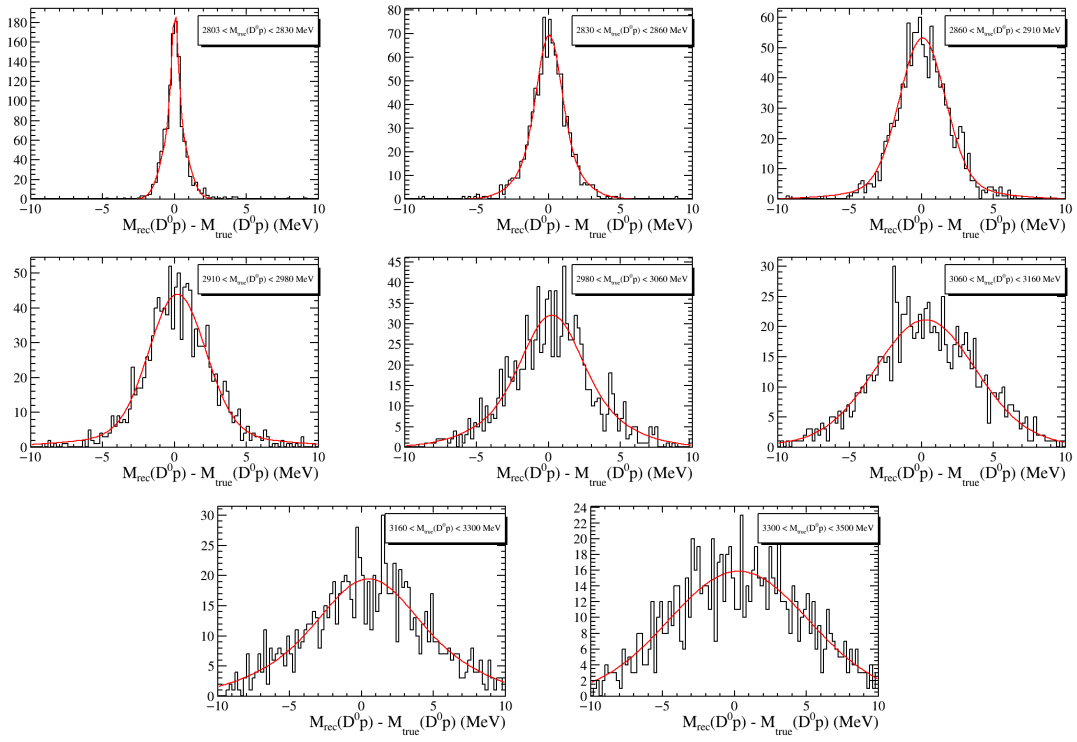

Figure A.1: Fit of a double Gaussian to the difference between generated and reconstructed D^0p mass (simulation sample) in different bins of true D^0p mass. The width of distributions corresponds to the mass resolution for the respective bin.

Appendix B

Reweighting of $\Lambda_b^0 \to D^0 p \mu^- \overline{\nu}_\mu X$ decay simulation

Figure B.1 shows several more comparisons of data and simulation before and after reweighting. More on the reweighting process can be found in Section 8.2.

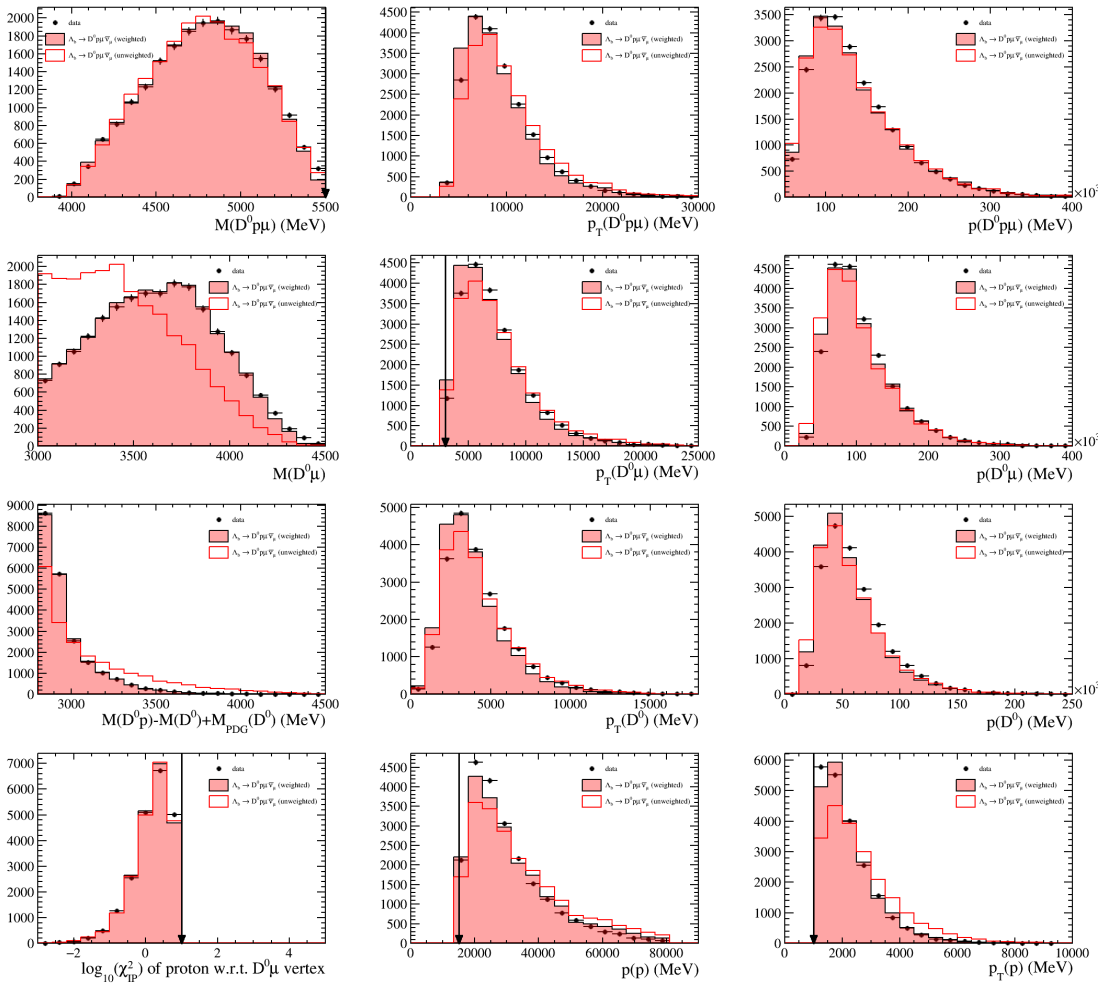

Figure B.1: Comparison of data (black points) and simulation for the $\Lambda_b^0 \to D^0 p\mu^- \overline{\nu}_\mu X$ channel before (red line) and after (red shaded area) three-dimensional reweighting as described in Section 8.2.

Appendix C

Reweighting and comparison of the $\Lambda_b^0 \to \Lambda_c^+ \mu^- \overline{\nu}_\mu$ candidates

Except for the kinematic p_{T} (Λ_b^0) reweighting, no additional reweighting is applied as for $\Lambda_b^0 \to D^0 p \mu^- \overline{\nu}_\mu$. However, the data is polluted by two decays into excited states, $\Lambda_b^0 \to \Lambda_c^*(2593)^+ \mu^- \overline{\nu}_\mu$ and $\Lambda_b^0 \to \Lambda_c^*(2625)^+ \overline{\nu}_\mu$. Thus, Figure C.1 shows a comparison of side bandsubtracted data and the sum of the three different channels. They are summed up according to the yields obtained by the fit to the corrected Λ_b^0 mass in Section 7.

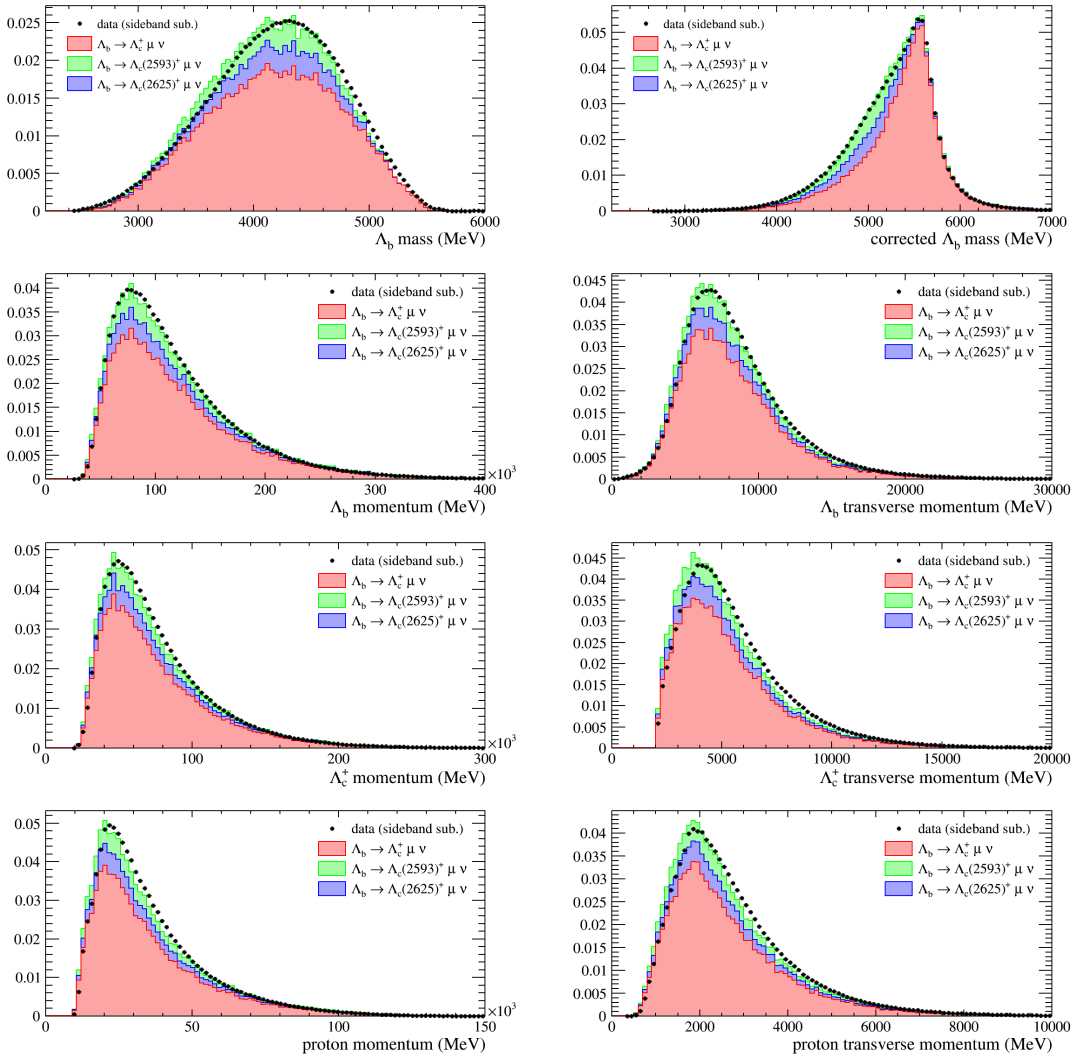

Figure C.1: Comparison of sidebandsubtracted data and the sum of the simulations describing the decays $\Lambda_c^+ \to pK^-\pi^+$, $\Lambda_b^0 \to \Lambda_c^*(2593)^+ \mu^- \overline{\nu}_\mu$ and $\Lambda_b^0 \to \Lambda_c^*(2625)^+ \mu^- \overline{\nu}_\mu$. Only the kinematic p_{T} (Λ_b^0) reweighting is applied.

Bibliography

[1] S. L. Glashow, *Partial Symmetries of Weak Interactions*, Nucl. Phys. **22** (1961) 579.

[2] A. Salam and J. C. Ward, *Weak and electromagnetic interactions*, Nuovo Cim. **11** (1959) 568.

[3] S. Weinberg, *A Model of Leptons*, Phys. Rev. Lett. **19** (1967) 1264.

[4] ATLAS, G. Aad *et al.*, *Observation of a new particle in the search for the Standard Model Higgs boson with the ATLAS detector at the LHC*, Phys. Lett. **B716** (2012) 1, arXiv:1207.7214.

[5] CMS, S. Chatrchyan *et al.*, *Observation of a new boson at a mass of 125 GeV with the CMS experiment at the LHC*, Phys. Lett. **B716** (2012) 30, arXiv:1207.7235.

[6] Planck, P. A. R. Ade *et al.*, *Planck 2013 results. I. Overview of products and scientific results*, Astron. Astrophys. **571** (2014) A1, arXiv:1303.5062.

[7] CERN, *The large hadron collider*, http://home.web.cern.ch/topics/large-hadron-collider. Accessed: 2015-08-06.

[8] A. G. Grozin, *Introduction to the heavy quark effective theory. part 1*, arXiv:hep-ph/9908366.

[9] S. Migura, D. Merten, B. Metsch, and H.-R. Petry, *Charmed baryons in a relativistic quark model*, Eur. Phys. J. **A28** (2006) 41, arXiv:hep-ph/0602153.

[10] LHCb, R. Aaij *et al.*, *Measurement of the semileptonic CP asymmetry in $B^0 - \overline{B}^0$ mixing*, Phys. Rev. Lett. **114** (2015) 041601, arXiv:1409.8586.

[11] LHCb, R. Aaij *et al.*, *Determination of the quark coupling strength $|V_{ub}|$ using baryonic decays*, arXiv:1504.0156.

[12] LHCb, R. Aaij *et al.*, *Observation of the resonant character of the $Z(4430)^-$ state*, Phys. Rev. Lett. **112** (2014), no. 22 222002, arXiv:1404.1903.

[13] LHCb, R. Aaij *et al.*, *Observation of $J/\psi p$ Resonances Consistent with Pentaquark States in $\Lambda_b^0 \to J/\psi K^- p$ Decays*, Phys. Rev. Lett. **115** (2015), no. 7 072001, arXiv:1507.0341.

[14] D. H. Perkins, *Introduction to High Energy Physics*, Cambridge University Press, 2000.

[15] C. P. Burgess and G. D. Moore, *The standard model: A primer*, Cambridge University Press, 2006.

[16] M. Meissner, *Measurements of particle production and particle correlations in proton-proton and proton-ion collisions with LHCb*, PhD thesis, Heidelberg U.

[17] http://www.isgtw.org/sites/default/files/Standard_model_infographic.png. Accessed: 2015-08-27.

[18] K. A. Olive and P. D. Group, *Review of particle physics*, Chinese Physics C **38** (2014), no. 9 090001.

[19] LHCb, R. Aaij *et al.*, *Studies of beauty baryon decays to D^0ph^- and $\Lambda_c^+h^-$ final states*, Phys. Rev. **D89** (2014), no. 3 032001, arXiv:1311.4823.

[20] BaBar, B. Aubert *et al.*, *Observation of a charmed baryon decaying to D0p at a mass near 2.94 GeV/c^2*, Phys. Rev. Lett. **98** (2007) 012001, arXiv:hep-ex/0603052.

[21] R. Gupta, *Introduction to lattice QCD: Course*, in *Probing the standard model of particle interactions. Proceedings, Summer School in Theoretical Physics, NATO Advanced Study Institute, 68th session, Les Houches, France, July 28-September 5, 1997. Pt. 1, 2*, pp. 83–219, 1997. arXiv:hep-lat/9807028.

[22] LHCb, B. Adeva *et al.*, *Roadmap for selected key measurements of LHCb*, arXiv:0912.4179.

[23] M. Kobayashi and T. Maskawa, *CP Violation in the Renormalizable Theory of Weak Interaction*, Prog. Theor. Phys. **49** (1973) 652.

[24] L. Wolfenstein, *Parametrization of the Kobayashi-Maskawa Matrix*, Phys. Rev. Lett. **51** (1983) 1945.

[25] U. Nierste, *Three Lectures on Meson Mixing and CKM phenomenology*, in *Heavy quark physics. Proceedings, Helmholtz International School, HQP08, Dubna, Russia, August 11-21, 2008*, pp. 1–38, 2009. arXiv:0904.1869.

[26] C.-H. Chen and S.-h. Nam, *Left-right mixing on leptonic and semileptonic $b \to u$ decays*, Phys. Lett. **B666** (2008) 462, arXiv:0807.0896.

[27] CKMfitter Group, J. Charles *et al.*, *CP violation and the CKM matrix: Assessing the impact of the asymmetric B factories*, Eur. Phys. J. **C41** (2005) 1, arXiv:hep-ph/0406184.

[28] A. D. Sakharov, *Violation of CP Invariance, c Asymmetry, and Baryon Asymmetry of the Universe*, Pisma Zh. Eksp. Teor. Fiz. **5** (1967) 32, [Usp. Fiz. Nauk161,61(1991)].

[29] A. Lenz and U. Nierste, *Numerical Updates of Lifetimes and Mixing Parameters of B Mesons*, in *CKM unitarity triangle. Proceedings, 6th International Workshop, CKM 2010, Warwick, UK, September 6-10, 2010*, 2011. arXiv:1102.4274.

[30] L. Lista, *Statistical Methods for Data Analysis in Particle Physics*, Lect. Notes Phys. **909** (2016) pp.1.

[31] R. J. Barlow and C. Beeston, *Fitting using finite Monte Carlo samples*, Comput. Phys. Commun. **77** (1993) 219.

[32] L. Evans and P. Bryant, *LHC Machine*, JINST **3** (2008) S08001.

[33] ATLAS, G. Aad *et al.*, *The ATLAS Experiment at the CERN Large Hadron Collider*, JINST **3** (2008) S08003.

[34] CMS, S. Chatrchyan *et al.*, *The CMS experiment at the CERN LHC*, JINST **3** (2008) S08004.

[35] ALICE, K. Aamodt *et al.*, *The ALICE experiment at the CERN LHC*, JINST **3** (2008) S08002.

[36] LHCb collaboration, A. A. Alves Jr. *et al.*, *The LHCb detector at the LHC*, JINST **3** (2008) S08005.

[37] LHCb speaker's bureau, *LHCb $\bar{b}b$ production angle plots*, https://lhcb.web.cern.ch/lhcb/speakersbureau/html/bb_ProductionAngles.html. Accessed: 2015-08-11.

[38] LHCb Collaboration, *LHCb VELO (VErtex LOcator): Technical Design Report*, Technical Design Report LHCb, CERN, Geneva, 2001.

[39] LHCb, R. Aaij *et al.*, *Precision measurement of the B_s^0-$\bar{B}_s^0$ oscillation frequency with the decay $B_s^0 \to D_s^- \pi^+$*, New J. Phys. **15** (2013) 053021, arXiv:1304.4741.

[40] R. Aaij *et al.*, *Performance of the LHCb Vertex Locator*, JINST **9** (2014) 09007, arXiv:1405.7808.

[41] LHCb Silicon Tracker Group, J. Luisier, *Performance of LHCb Silicon Tracker Detector in the LHC*, Phys. Procedia **37** (2012) 851.

[42] LHCb Outer Tracker Group, R. Arink *et al.*, *Performance of the LHCb Outer Tracker*, JINST **9** (2014), no. 01 P01002, arXiv:1311.3893.

[43] LHCb, *LHCb technical design report: Reoptimized detector design and performance*, 2003.

[44] J. D. Jackson, *Classical electrodynamics*, Wiley, 1975.

[45] LHCb RICH Group, M. Adinolfi *et al.*, *Performance of the LHCb RICH detector at the LHC*, Eur. Phys. J. **C73** (2013) 2431, arXiv:1211.6759.

[46] LHCb, E. P. Olloqui, *LHCb preshower(PS) and scintillating pad detector (SPD): Commissioning, calibration, and monitoring*, J. Phys. Conf. Ser. **160** (2009) 012046.

[47] LHCb, P. Perret, *First Years of Running for the LHCb Calorimeter System*, PoS **TIPP2014** (2014) 030, arXiv:1407.4289.

[48] I. Machikhiliyan and the LHCb calorimeter group, *The LHCb electromagnetic calorimeter*, Journal of Physics: Conference Series **160** (2009), no. 1 012047.

[49] Y. Guz and the LHCb collaboration, *The LHCb Hadron Calorimeter*, Journal of Physics: Conference Series **160** (2009), no. 1 012054.

[50] A. A. Alves *et al.*, *Performance of the LHCb muon system*, Journal of Instrumentation **8** (2013), no. 02 P02022.

[51] T. Head, *The LHCb trigger system*, Journal of Instrumentation **9** (2014), no. 09 C09015.

[52] R. Aaij *et al.*, *The LHCb Trigger and its Performance in 2011*, JINST **8** (2013) P04022, arXiv:1211.3055.

[53] Belle Collaboration, A. Zupanc *et al.*, *Measurement of the Branching Fraction* $\mathcal{B}(\Lambda_c^+ \to pK^-\pi^+)$, Phys. Rev. Lett. **113** (2014), no. 4 042002, arXiv:1312.7826.

[54] SLD, K. Abe *et al.*, *A Measurement of R(b) using a vertex mass tag*, Phys. Rev. Lett. **80** (1998) 660, arXiv:hep-ex/9708015.

[55] M. Williams *et al.*, *The HLT2 Topological Lines*, 2011.

[56] G. J. Barker, *b-quark physics with the LEP collider*, Springer Tracts Mod. Phys. **236** (2010) pp. 170.

[57] Fermilab E653, K. Kodama *et al.*, *Measurement of the relative branching fraction* $\Gamma(D^0 \to K\mu\nu)/\Gamma(D^0 \to \mu X)$, Phys. Rev. Lett. **66** (1991) 1819.

[58] L. Demortier and L. Lyons, *Everything you always wanted to know about pulls*, Tech. Rep. CDF/ANAL/PUBLIC/5776, CDF, February, 2002.

[59] J. Gaiser, *Charmonium Spectroscopy From Radiative Decays of the J/ψ and ψ'*, PhD thesis, SLAC, 1982.

[60] BaBar, P. del Amo Sanchez *et al.*, *Observation of new resonances decaying to $D\pi$ and $D^*\pi$ in inclusive e^+e^- collisions near $\sqrt{s}$ =10.58 GeV*, Phys. Rev. **D82** (2010) 111101, arXiv:1009.2076.

[61] M. Artuso, C. Hadjivasiliou, and M. Kelsey, *Measurement of the form factor shape for the semileptonic decay $\Lambda_b^0 \to \Lambda_c^+ \mu\nu$*, .

[62] Belle, K. Abe *et al.*, *Experimental constraints on the possible J^P quantum numbers of the $\Lambda_c(2880)^+$*, Phys. Rev. Lett. **98** (2007) 262001, arXiv:hep-ex/0608043.

[63] LHCb, R. Aaij *et al.*, *Study of the kinematic dependences of Λ_b^0 production in pp collisions and a measurement of the $\Lambda_b^0 \to \Lambda_c^+\pi^-$ branching fraction*, JHEP **08** (2014) 143, arXiv:1405.6842.

[64] D. Casadei, *Estimating the selection efficiency*, Journal of Instrumentation **7** (2012) 8021, arXiv:0908.0130.

[65] LHCb, *Pidcalib packages*, https://twiki.cern.ch/twiki/bin/view/LHCb/PIDCalibPackage. Accessed: 2015-08-09.

[66] F. Archilli *et al.*, *Performance of the Muon Identification at LHCb*, JINST **8** (2013) P10020, arXiv:1306.0249.

Erklärung:

Ich versichere, dass ich diese Arbeit selbstständig verfasst habe und keine anderen als die angegebenen Quellen und Hilfsmittel benutzt habe.

Heidelberg, den 09. September 2015 .....